2019

Tailoring acoustic waves with metamaterials and metasurfaces

BOSTON UNIVERSITY

COLLEGE OF ENGINEERING

Dissertation

TAILORING ACOUSTIC WAVES WITH METAMATERIALS AND METASURFACES

by

REZA GHAFFARIVARDAVAGH

B.S., Sharif University of Technology, 2011
M.S., Boston University, 2016

Submitted in partial fulfillment of the

requirements for the degree of

Doctor of Philosophy

2019

Approved by

First Reader

Xin Zhang, Ph.D.
Professor of Mechanical Engineering
Professor of Electrical and Computer Engineering
Professor of Biomedical Engineering
Professor of Materials Science and Engineering

Second Reader

Stephan W. Anderson, MD
Professor of Radiology
Boston University, School of Medicine

Third Reader

Thomas G. Bifano, Ph.D.
Professor of Mechanical Engineering
Professor of Materials Science and Engineering
Professor of Biomedical Engineering

Fourth Reader

R. Glynn Holt, Ph.D.
Associate Professor of Mechanical Engineering

Fifth Reader

Matthew D. Guild, Ph.D.
Adjunct Professor of Mechanical Engineering
The Catholic University of America
Research Scientist
U.S. Naval Research Laboratory

DEDICATION

I want to dedicate this work to my lovely wife, Sheyda, my parents, Nader and Nasrin, and my sisters Parisa and Delsa.

ACKNOWLEDGMENTS

I would like to express my sincere appreciation to my advisor Professor Xin Zhang who has always trusted me during my study at BU. From the day she recruited me as a Ph.D. student in her class until my last day at BU, she has always been the source of inspiration for me. Without her continuous support, this dissertation would not have been possible. I would like to thank my co-advisor Professor Stephan Anderson, for his invaluable passion, creative vision, and insightful discussion, which were truly inspirational to me. It has been my absolute pleasure working under his guidance. I would like to thank Professor Glynn Holt, who first, introduced me to the beautiful world of acoustics and further helped me with his continuous guidance and letting me do some experiments in his lab. I would like to sincerely thank Professor Thomas Bifano and Professor Matthew Guild for all their technical and non-technical supports and their invaluable comments. I would like to thank professor Mohsen Ahmadian for all his invaluable comments and guidance with regards to chapter 5 of this dissertation.

I would like to thank current and former members in Professor Xin Zhang's group for all the help and support. Jacob Nickolajczyk and Rui Wu have helped me in different projects. Huseyin Seren, Xiaoguang Zhao, Gunagwu Duan, Aobo Li David Sutherland, Ryan McNaughton, Chunxu Chen, Ke Wu, Samuel Kann also gave me a lot of support and helpful discussion. I would also like to thank everyone who keeps the facilities in BU and BU Photonics Center up and running. Particularly, all the personals associated with EPIC center who helped me to fabricate the metamaterials I designed.

I would like to thank my parents, Nasrin and Nader for all their love and support. They have always been my role model on not just pursuing science, but also on how to live life. I would like to thank my dear sisters and brother-in-law, Parisa, Delsa, and Hossein for all their love and support. I want to thank my father-in-law and mother-in-law Gholamreza and Farzaneh, sister-in-law, and brother-in-law, Shadi, and Shayan for all their love and support.

In the end, I would like to express my deepest appreciation to my lovely wife, Sheyda. Her love and support have always fueled me to overcome the hurdles in my life, specifically during my journey to the USA for pursuing science. Without her sacrifices, I was not able to reach this far.

TAILORING ACOUSTIC WAVES WITH

METAMATERIALS AND METASURFACES

REZA GHAFFARIVARDAVAGH

Boston University, College of Engineering, 2019

Major Professor: Xin Zhang, Ph.D., Professor of Mechanical Engineering, Professor of Electrical and Computer Engineering, Professor of Biomedical Engineering, Professor of Materials Science and Engineering

ABSTRACT

Nowadays, metamaterials have found their places in different branches of wave physics ranging from electromagnetics to acoustic waves. Acoustic metamaterials are sub-wavelength structures in which their effective acoustic properties are dominated by their structural shape rather than their constitutive materials. In recent years, acoustic metamaterials have gained increasing interest due to numerous promising applications such as sub-wavelength imaging, perfect absorption, acoustic cloaking, etc. The focus of the work herein is to leverage acoustic metamaterial/metasurface structures to manipulate the acoustic wavefront to pave the road for future applications of the metamaterials.

In the first part of the work, the metamaterial structure is introduced, which can be leveraged for better manipulation of the transmitted wave by modulating both phase and amplitude. Initially, a general bound on the transmission phase/amplitude space for the case of arbitrary metasurface has been presented and subsequently, the necessary condition for the complete modulation of the transmitted wave is investigated. Next, a horn-like space coiling metamaterial is introduced, which satisfied the aforementioned condition and enabled us to simultaneously modulate both the phase and amplitude of the transmitted

wave. Furthermore, our initial efforts toward designing a metamaterial capable of real-time phase modulation with relatively constant amplitude will be discussed.

In the second part of this work, a novel metamaterial-based methodology is presented for the design of the air permeable acoustic silencer. In this work, the concept of the bilayer-transverse metamaterial is introduced, and its functionality for silencing the acoustic wave is demonstrated. Furthermore, it is shown that the methodology presented herein essentially does not limit the ratio of the open area, and ultra-open metamaterial silencers may be designed. Eventually, based on the presented methodology, the ultra-open metamaterial featuring nearly 60% open area is designed, and silencing capacity of about 94% at the targeted frequency is experimentally realized.

In the last part of this work, the behavior of a locally resonant class of acoustic metamaterial in the non-Rayleigh regime has been explored. Elaborately, it is demonstrated that in the case of spherical inclusion in a matrix material, large variation in the effective acoustic impedance emerges near the inclusion's Eigenmode. Eventually, the potential application of this novel phenomenon in the non-destructive evaluation (NDE) and ultrasound imaging is discussed.

TABLE OF CONTENTS

DEDICATION iv

ACKNOWLEDGMENTS v

TABLE OF CONTENTS ix

LIST OF TABLES xi

LIST OF FIGURES xii

CHAPTER 1 INTRODUCTION 1

1.1 Introduction to Acoustic Metamaterial 1

1.2 Thesis Outline 2

CHAPTER 2 SIMULTANEOUS PHASE AND AMPLITUDE MODULATION 5

2.1 Phase and Amplitude Modulation in Space-Coiling Metamaterial 7

2.2. Generalized Complex Transmission Bound for the Arbitrary Metasurface 13

2.3. Horn-like Space-coiling Metamaterial 15

2.4 Full Wavefront Modulation Using Horn-like Metasurface 25

CHAPTER 3 DOUBLE DECORATED MEMBRANE METAMATERIAL: INITIAL EFFORT FOR REAL-TIME PHASE MODULATION 33

3.1 Transmission in Single and Double Decorated Membrane: 33

Numerical Study 33

3.2 Transmission in the single and double decorated membrane: 39

Experimental study 39

CHAPTER 4 ULTRA-OPEN ACOUSTIC METAMATERIAL SILENCER 46

4.1 Fano-like Interference in Transverse Bilayer Metamaterial 48

4.2 Ultra-Open Metamaterial for Selective Sound Silencing 61

CHAPTER 5 LOCALLY RESONANT ACOUSTIC METAMATERIAL: PROPOSED APPLICATIONS IN NDE AND MEDICAL ULTRASOUND 72

5.1 Resonant Induced Impedance Variation in LRAM 73

5.2 LRAM as a contrast agent 80
5.3 LRAM as an Anti-Reflection Layer 85

CHAPTER 6 CONCLUSION 93

APPENDIX 95
A. Transfer Matrix Method (TMM) to Derive the Complex Transmission 95
B. Effect of Unit cells' width on modulation efficiency 105
C. Phase Modulation versus Phase/Amplitude modulation 106
D. Unit cell's geometry and predicted complex transmission 108
E. Impedance Tube for Measuring Transmittance 109
Reflection and Transmission in symmetrical Material 115
Reflection and Transmission in asymmetrical Material 117
Experimental Validation for Symmetrical Sample using one-load Method 118
Experimental Validation for Asymmetrical Sample using two-load Method 123

BIBLIOGRAPHY 128

CURRICULUM VITAE 137

LIST OF TABLES

Table D.1. Geometrical features and associated transmission in metasurface unit cells 108

LIST OF FIGURES

Figure 2.1. Traditional space-coiling metamaterial unit cell and its equivalent model. (a) Space-coiling metamaterial structure with the overall length of (t) and overall width of (a) is depicted here. (d) and (w) are channel width and coil's wall thickness respectively; acoustic wave trajectory is shown as the dashed line in which (L) represents the wave trajectory length within each coil. (b) Equivalent model of the coil structure featuring a single straight channel filled with a medium of different refractive index ($n_r n_0$). 8

Figure 2.2. Phase and amplitude of the transmitted wave with conventional space-coiling structure. The colored region is the predicted space using the equivalent model. Scatter results shown by red dots are derived from the TMM-based approach by varying the geometry of the unit cell. 12

Figure 2.3. Horn-like space-coiling metamaterial unit cell and its equivalent model. (a) Horn-like space-coiling metamaterial structure composed of 6 coils is shown here in which d_n (n=1:6) represents the channel width at n^{th} coil, and d_7 is the channel width at the output port; channel widths follow the geometrical sequence with the common ratio in excess of one (CR >1). (b) Equivalent model of the gradient coil structure featuring a horn-shaped channel of length Leff filled with original medium with a refractive index of (n0). 16

Figure 2.4. Space-coiling unit cell with a gradual change in channel width as an exponential horn. (a) Horn-like space-coiling metamaterial with an effective length of

the acoustic pathway shown with orange dashed-line. (b) Comparison between the exact profile of the channel and the approximated horn model. 17

Figure 2.5. Transmission through horn-like space-coiling metamaterial derived from three different approaches. Exact model refers to the TMM presented in Appendix A, and equivalent model refers to the horn-like model discussed here. 20

Figure 2.6. Illustration of the result space for gradient space-coiling metamaterials with varying common ratio (CR). The colored region (pink) is the region defined by Equation (2.36), and the dot points represent the results from TMM..... 24

Figure 2.7. (a) Acoustic plane wave with an amplitude of 1kPa incident on the left-hand-side of the metasurface and the resultant focusing on the right-hand-side. (b) Acoustic beam splitter that transforms the plane incident wave with the amplitude of 1kPa to two equi-amplitude beams in $\pi/12$ and $-\pi/12$ directions. (c) Pressure profile along the cut-line with the length of 5λ extending through the focal spot shown in Figure (2.5a). (d) Pressure profile along the cut-line placed at a distance of 5λ from the metasurface (2.5b). In Figures (2.5c) and (2.5d), the red line represents the data from the lossless simulation while the blue dotted line represents the data with the presence of loss. 27

Figure 2.8. Experimental setup employed to map the resultant acoustic field in the specified region on the transmission side of the metasurface. 29

Figure 2.9. Numerical and experimental results of the reverse form of focusing in which a monopole point source is placed two wavelengths away from the metasurface, and a laterally confined plane wave is created on the transmission side. (a) Simulation results showing the cylindrical to plane wave conversion. Rectangular dotted region

depicts the location in which the experimental acoustic wave pattern was mapped. (b) Measured normalized acoustic field in the absence of the metasurface. (c) Measured normalized acoustic field in the presence of the metasurface..... 30

Figure 3.1. Complex transmission through the single decorated membrane. (a) Transmission amplitude for different values of the applied voltage. (b) Transmission phase for different values of the applied voltage. 34

Figure 3.2. Complex transmission through the double decorated membrane. (a) Transmission amplitude for the different spacing of the membranes and occurrence of in-phase and out-of-phase resonances. (b) Transmission phase for the different spacing of the membranes and occurrence of Pi phase shift for both in-phase and out-of-phase resonances. (c) Transmission amplitude for merged resonances in the optimized double decorated membrane. (d) Transmission phase for merged resonances in optimized double decorated membrane structure..... 37

Figure 3.3. Experimental apparatus. (a) Impedance tube setup. (b) single decorate membrane. (c) double membrane with no attached mass. 39

Figure 3.4. Experimentally obtained complex transmission for single decorated membrane. (a) Transmission amplitude for three different masses attached on the membrane. (b) Transmission phase for three different masses attached on the membrane..... 40

Figure 3.5. Complex transmission through the double decorated membrane. (a) Transmission amplitude for three different combinations of masses attached on the

membranes. (b) Transmission phase for three different combinations of masses attached on the membrane. 42

Figure 3.6. Experimental result for double decorated membrane when M_1 and M_2 are both equal to 2m and with the spacing of 3cm between membranes. (a) Transmission through Xenon filled double membrane. (b) Transmission through double Mylar membrane. (c) Transmission, Reflection, and Absorption in double Mylar membrane. (d) Coupled transmission in double Mylar membrane. 43

Figure 4.1. Transverse bilayer metamaterial. The metamaterial is shown here in which the two colored regions are composed of regions with distinct acoustic properties placed transversely with respect to the wave propagation direction 49

Figure 4.2. Analytical results. (a) Acoustic transmittance through the transverse bilayer metamaterial for different values of Acoustic impedance contrast when the refractive indices ratio is kept constant. Notably, for the cases with a finite ratio between the impedance of the regions (shown with the blue line, orange dashed line, and the yellow dotted line), Fano-like interference results in destructive interference. However, in the case of infinite contrast between the regions impedance, representing orifice-like behavior, the destructive interference is suppressed (purple dotted-dashed line). (b) Acoustic transmittance through the bilayer metamaterial for different ratios of the refractive indices when the acoustic impedance is kept constant. For different values of refractive index. 57

Figure 4.3. (a)Acoustic transmittance from transverse bilayer metamaterial structure with different refractive index ratios and a constant impedance ratio of 10. The silencing

functionality initially emerges when n_2t is equal to half wavelength but is also present in higher order harmonics when it approximates integer multiplication of half wavelength. (b) Acoustic transmittance through transverse bilayer metamaterial in case of oblique incidence with different incident angles. 60

Figure 4.4. (a) UOM structure is shown in which the open region at the center ($r < r_1$) corresponds to region 1 in the transverse bilayer metamaterial and the outer region, featuring six channels coiled in the form of helix ($r_1 < r < r_2$), corresponds to region 2. (b) Internal structure of the UOM is shown with an acoustic wave traveling through the channels and essentially following the helical pathway with a helix angle of φ. 62

Figure 4.5. Acoustic transmittance resulting from the impedance tube experiment is shown with the dotted-line with a triangular marker demonstrating that near 460 Hz, the transmittance is reduced to the minimum value of approximately 0.06. Sound transmission loss (STL) for the wave passing through the UOM is also shown with the dashed line corresponding the rightward y-axis. The solid line represents the predicted behavior using Green's function method by modeling the UOM structure as a transverse bilayer metamaterial..... 66

Figure 4.6. (a) The absolute pressure value normalized by the incident wave magnitude resulting from a plane wave with a frequency of 400 Hz and an incident on the UOM from the left-hand side is shown using a color map. The local velocity stream is shown with the white lines. At this frequency, the transmission coefficient is about 0.85, hence, approximately 72% of the acoustic wave energy is transmitted. (b) The pressure and velocity profile are depicted with an incident plane wave of the same

amplitude but a frequency of 460 Hz. At this frequency, due to Fano-like interference, the transmitted wave has a markedly decreased amplitude, and the wave has been silenced. In this case, the phase difference between the transmitted waves from the two regions of the metamaterial has resulted in a curvature of the wave velocity field and has diminished the far-field radiation. (c) Acoustic transmittance through UOM structures with different degrees of structure openness. Transmittance has been analytically derived using Green's function method. Notably, UOM structures considered herein feature identical refractive index ratios in their transverse bilayer metamaterial model but have different impedance ratios. 68

Figure 5.1. Locally resonant acoustic metamaterial with hard inclusion in a soft matrix. (a). single layer spherical inclusion. (b) Bilayer spherical inclusion 74

Figure 5.2. Effective acoustic properties of LRAM in the non-Rayleigh regime. (a) Normalized effective stiffness. (b)Normalized effective density. (c) Effective refractive index. (d)Normalized effective acoustic impedance. Normalized quantities have been normalized by the value of the matrix medium. f_0 denotes the first resonance mode of the inclusion (monopole), and f_1 is the second mode of the resonance of the inclusion (dipole). 76

Figure 5.3. Retrieved effective impedance and wavenumber of the unit cell of LRAM. (a) Effective wave number with the unit cell of LRAM shown here. (b) Effective impedance of the LRAM. 78

Figure 5.4. Effective impedance variation of the cement/sphere composite with different volume ratios of the spherical inclusions. 81

Figure 5.5. Illustration of the numerical model to investigate the functionality of the bilayer spherical inclusions as a contrast agent for cement bond logging. 82

Figure 5.6. Complex reflection in ultrasound-based cement bond logging. (a) & (b) cement. (c) & (d) Cement with bilayer spherical inclusion. (e) Signal variation ratio. 83

Figure 5.7. Application of the acoustic antireflection coating (ARC) on the skull 88

Figure 5.8. Application of the nAMC to realize enhanced transmission through the skull. 92

Figure A.1. Illustration of the internal structure of space–coiling unit cell. (a) Space-coiling structure associated propagation tensor for each section. (b) Single coil structure, which has been divided into three sections: section A is the input port, section B is the main channel, and section C is the output port. 96

Figure A.2. Transmission and Reflection from Space-coiling metamaterial..... 102

Figure A.3. Comparison between analytical and numerical transmission and reflection. (a) Transmission and reflection amplitude. (b) Transmission and reflection phase. The analytical-labeled legend refers to the results of the TMM methods and Numerical-labeled legends corresponds to the results obtained with simulation (COMSOL). 103

Figure B.1. Sound focusing lateral profile for unit cells of different widths. 105

Figure C.1. Acoustic beam splitting. (a) Phase modulation. (b) Phase-amplitude modulation. 107

Figure E.1. Impedance tube setup with 4-microphones configuration 112

Figure E.2. Transmission and reflection amplitude and phase for the case of open termination. Results based on our method, i.e., UWD are shown with a solid red line. Results using the modified wave decomposition method (MWD) based on Ho's work (Ho et al., 2005) are shown with a black dotted line. Moreover, the results based on the Transfer Matrix approach based on Bolton's methods (Olivieri et al., 2006) are shown with a black dashed line. (a) Transmission amplitude. (b) Transmission phase. (c) Reflection amplitude. (d) Reflection phase. 120

Figure E.3. Transmission and reflection amplitude and phase for the case of rigid termination. Results based on our method, i.e., UWD are shown with a solid red line. Results using the modified wave decomposition method (MWD) based on Ho's work (Ho et al., 2005) are shown with a black dotted line. And the results based on the Transfer Matrix approach based on Bolton's methods (Olivieri et al., 2006) are shown with a black dashed line. (a) Transmission amplitude. (b) Transmission phase. (c) Reflection amplitude. (d) Reflection phase. 121

Figure E.4. Transmission and reflection amplitude and phase for the case of semi-anechoic termination. Results based on our method, i.e., UWD are shown with a solid red line. Results using the modified wave decomposition method (MWD) based on Ho's work (Ho et al., 2005) are shown with a black dotted line. And the results based on the Transfer Matrix approach based on Bolton's methods (Olivieri et al., 2006) are shown with a black dashed line. (a) Transmission amplitude. (b) Transmission phase. (c) Reflection amplitude. (d) Reflection phase. 122

Figure E.5. Transmission and reflection for asymmetrical material. (a) Transmission amplitude. (b) Transmission phase. (c) Reflection (r_1) amplitude. (d) Reflection (r_1) phase. (e) Reflection (r_2) amplitude. (f) Reflection (r_2) phase. 125

Figure E.6. Maximum variation in the calculated amplitude and phase when a different pair of termination is employed. (a) Amplitude variation. (b) Phase variation. 127

CHAPTER 1 INTRODUCTION

1.1 Introduction to Acoustic Metamaterial

Metamaterials, which are composed of sub-wavelength unit cells, can exhibit extraordinary behaviors that are not readily found in nature. The fundamental idea behind the science of metamaterials is to conceptually replace the molecules with tailored unit cell structures in the order of much less than the wavelength. Subsequently, based on the unit cell's design, the metamaterial structure may exhibit a myriad of behavior which may be characterized by its effective properties. The concept of metamaterial was first theoretically proposed by Veselago (Veselago, 1968), who proposed that a medium with negative permittivity and permeability will possess a negative refractive index. Followed by the Veselago's proposition, Pendry et al. (Pendry et al., 1999) designed a metamaterial unit cell with simultaneously negative permeability and permittivity. Nowadays, the achievement of negative permeability and permittivity in electromagnetic metamaterials has been widely reported, with novel phenomena including negative index materials and cloaking having been realized in this area (Smith et al., 2004; Schurig et al., 2006).

Based on the analogy between the governing equations of acoustic waves and the electromagnetic Maxwell equations (Carcione et al., 1995), the effective density and compressibility of the medium are seen to be the critical features for acoustic wave propagation. With regards to acoustic metamaterials, the design of sub-wavelength unit cell structures enables control over the effective density and compressibility in order to achieve acoustic wave manipulation such as negative index acoustic metamaterials (Fol et al., 2011; Zhai et al., 2013; Xie et al., 2013; Brunet et al., 2015). Recently, acoustic

metamaterials have gained increasing interest due to numerous promising applications such as sub-wavelength imaging (Moleron et al., 2015; Su et al., 2014), perfect absorption (Fink, 2014; Mei et al., 2012), acoustic cloaking (Yang et al., 2013; Zingoneanu et al., 2014; Li et al, 2015), and acoustic diodes (Liang et al, 2009).

Among the applications of metamaterial and metasurfaces, there exists a growing interest in acoustic wavefront modulation given the numerous promising applications such as acoustic communication and biomedical imaging, among others. The thesis herein aims to explore different aspects of metamaterial based acoustic wavefront modulation to pave the way for more advanced applications of metamaterial structure for tailoring acoustic waves. For this aim, four different aspects of wavefront modulation will be addressed and investigated. Considering acoustic wavefront is essentially composed of two main components, i.e., phase and amplitude, the next two chapters (chapter 2 and chapter 3) have been devoted to addressing the current issues with regards to the phase modulation by first introducing full-wavefront modulation in chapter 2 and further investigation on the tunable phase modulation in chapter 3. Subsequently, chapter 4 and chapter 5 are dedicated to investigating metamaterial-based wavefront manipulation with the focus of amplitude modulation.

1.2 Thesis Outline

Chapter 2 of this thesis seeks to address the complexity associated with the phase-based wave modulation and ease the process by introducing the unit cell structure that can be utilized for complete wave modulation by simultaneously modulating both phase and

amplitude. In the context of complete acoustic wave modulation, in which both phase and amplitude are simultaneously modulated, the additional degree of freedom leads to a marked simplification of the metasurface design process. As opposed to complicated optimization procedures required with phase-based wavefront modulation, complete acoustic wave modulation may leverage the time-reversal technique in which the required phase and amplitude map may be readily obtained. Furthermore, by extending the properly designed unit cell structure to the 3D domain without additional complexity, acoustic metamaterial bricks or holograms may be generated to render 3D acoustic field patterns.

In **Chapter 3** of this thesis, the double decorated membrane will be studied, aiming for the realization of metamaterial structure with the capacity of tunable phase modulation. To this end, metamaterial and metasurfaces are predominantly designed as a passive structure, and tunability is a fundamental challenge not adequately addressed within this context. For this aim, double decorated membrane metamaterial structure will be investigated in which the coupled resonance of double membrane metamaterial may provide a degree of freedom to modulate the transmitted acoustic phase while maintaining the amplitude. Eventually, transmission through the double decorated membrane structure is experimentally studied, and present challenges and limitations will be discussed. Leveraging the double decorated membrane structure presented herein, one may realize tunable phase modulation by tailoring the membrane's Eigenmode.

In **Chapter 4**, it is intended to design a metamaterial structure that despite containing a large open area, features a negligible acoustic transmission in a specific range of the frequency. For this aim, Fano-like interference (Fano, 1961) is utilized to realize the

ultra-open metamaterial silencer, which can selectively silence the unwanted acoustic wave and simultaneously preserve the efficient ventilation. Furthermore, the performance of the proposed metamaterial structure functioning based on Fano-like interference is experimentally validated, and it is demonstrated that the openness of the presented methodology is essentially not bounded. The methodology presented herein is shown to have a harmonic silencing attribute which has made it readily applicable for fan or engine noise suppression.

In **Chapter 5** of this thesis, a class of locally resonant acoustic metamaterial has been studied. It is shown that in this class of metamaterial, the effective impedance of the whole structure exhibits an abrupt variation in the non-Rayleigh regime prior to the emergence of attenuation. Next, we have numerically demonstrated how this unnatural behavior may be leveraged in non-destructive evaluation by functioning as a contrast agent to enhance the reflection amplitude and in biomedical imaging by acting as an anti-reflection coating to amplify the transmission.

CHAPTER 2 SIMULTANEOUS PHASE AND AMPLITUDE MODULATION

Acoustic wavefront modulation is of great interest given the numerous promising applications such as acoustic communication and biomedical imaging, among others. Traditionally, acoustic wavefront modulation has been realized in the context of phased array transducers, which, due to their complexity, are considered expensive in terms of both design and implementation aspects. In recent years, following successful achievements in electromagnetic wave manipulation using metamaterials and metasurface science (Liu et al., 2014; Zhao et al., 2011; Ni et al., 2013; Estakhri et al., 2016) ongoing efforts have been made to utilize metasurfaces for acoustic wavefront modulation (Song et al., 2016; Zhao et al., 2013; Mei et al., 2014; Xie et al., 2014; Tang et al., 2014; Li et al., 2014; Li et al., 2015).

Metasurfaces, engineered surfaces of sub-wavelength thickness, offer a unique approach to acoustic manipulation in which the desired wave pattern may be achieved by precisely designing the constituent unit cell structures. Among the unit cell structures reported to date, space-coiling structures (Tang et al., 2014; Li et al., 2014; Li et al., 2013; Li et al., 2012; Sun et al., 2016; Yuan et al., 2015; Li et al., 2014; Li et al., 2013) are drawing growing attention due to their incredibly simple structure, ease of fabrication, and demonstration of successful wavefront manipulation capacity. In these structures, the space-coiling geometry is designed to generate the desired phase shift in the radiated acoustic signal while mitigating the impedance mismatch to optimize power transmission and amplitude uniformity (Li et al., 2013). Even though low transmission loss in such phase-based wavefront modulation yields high conversion efficiency (Wang et al., 2016),

the complexity of the design process required to obtain a desired metasurface phase map remains a fundamental limitation. Typically, iterative or stochastic algorithms are required to derive the ideal phase map, relying on an appropriate initial guess to reach the global minimum (Scheuer et al., 2016). Moreover, transitioning from two-dimensional (2D) to three-dimensional (3D) phase-based wavefront manipulation approaches radically increases the design cost and complexity.

In the context of complete acoustic wave modulation, in which both phase and amplitude are simultaneously modulated, the additional degree of freedom leads to a marked simplification of the metasurface design process. As opposed to complicated optimization procedures required with phase-based wavefront modulation, complete acoustic wave modulation may leverage the time-reversal technique (Scheuer et al., 2016) in which the required phase and amplitude map may be readily obtained. Furthermore, by extending the properly designed unit cell structure to the 3D domain without additional complexity, acoustic metamaterial bricks or holograms may be generated to render 3D acoustic field patterns.

While prior work has focused primarily on phase engineering, in this chapter, we demonstrate the possibility of simultaneous phase and amplitude modulation in a class of horn-like space-coiling metasurfaces. Utilizing a gradient in channel spacing of the unit cells, full acoustic control over wavefront modulation is realized. We firstly demonstrate that conventional space-coiling metamaterials possess a fundamental limitation in the simultaneous modulation of both phase and amplitude of transmitted wave acoustic waves. Specifically, the complex transmission through conventional space-coiling structures is

shown to be inherently bounded in certain complex regions. Subsequently, we extend the applicability of the presented bound to the general case of the metasurface and infer the necessary conditions for the realization of complete acoustic wavefront modulation. Ultimately, a modified, horn-like space-coiling metamaterial structure is presented that satisfies the necessary conditions for complete acoustic wave modulation. Finally, the functionality of the horn-like space-coiling metamaterial structure is theoretically and experimentally validated with regards to its capacity for simultaneous phase and amplitude modulation. This work seeks to shift the paradigm in acoustic metasurfaces through the realization of simultaneous control of phase and amplitude, thereby paving the way for a new generation of acoustic devices.

2.1 Phase and Amplitude Modulation in Space-Coiling Metamaterial

The concept of space-coiling metamaterials was initially proposed by Liang et al. (Liang et al., 2012). It was demonstrated that acoustic waves with frequencies above a given cutoff value would propagate along an elongated path within an assembly of zigzag channels shown in **Figure 2.1(a)**. The elongated path of the acoustic wave leads to the occurrence of a phase delay in the transmitted wave and, consequently, a higher refractive index is realized. Moreover, phenomena such as negative refractive index (Liang et al., 2013), zero indexes (Xie et al., 2013) and Dirac-like dispersion (Frenzel et al., 2013) have also been demonstrated using space-coiling structures. Space-coiling metamaterials possess marked advantages due to their simple structure and, consequently, ease of design. It has been demonstrated that when the channel width (d) is sufficiently small with respect to the

wavelength, the relative refractive index of the coiled structure (n_r: effective refractive index of coiled structure normalized by the original fluid index) can be precisely calculated using the path length of the acoustic wave shown in **Figure 2.1(a)** (Liang et al., 2012). The relative refractive index can be expressed as:

$$n_r = \frac{L_{eff}}{t} \tag{2.1}$$

Where t is the overall length of the coiled structure and L_{eff} can be estimated as:

$$L_{eff} \approx N \times L \tag{2.2}$$

Where N denotes the number of coils (for example, $N = 7$ in the structure depicted in **Figure 2.1(a)** and L is the length of each branch and is approximated as:

$$L = \sqrt{(a-d)^2 + (d+w)^2} \tag{2.3}$$

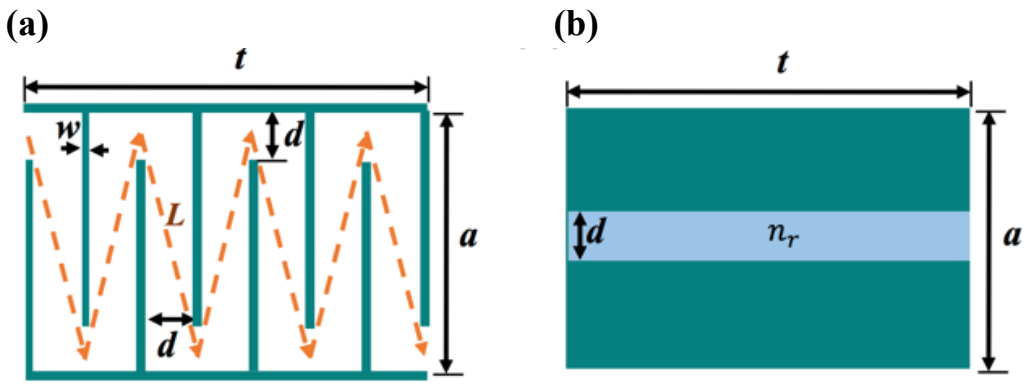

Figure 2.1: Traditional space-coiling metamaterial unit cell and its equivalent model. (a) Space-coiling metamaterial structure with the overall length of (t) and overall width of (a) is depicted here. (d) and (w) are channel width and coil's wall thickness respectively; acoustic wave trajectory is shown as the dashed line in which (L) represents the wave trajectory length within each coil. (b) Equivalent model of the coil structure featuring a single straight channel filled with a medium of different refractive index ($n_r n_0$).

Given the expression for the relative refractive index of the coil structure, it can be represented as an equivalent model of the same dimensions but comprised of a straight channel filled with a medium of the refractive index of $\boldsymbol{n_r n_0}$ shown in **Figure 2.1(b)** in which $\boldsymbol{n_0}$ represents the refractive index of the original fluid. Please note that from another perspective, the space-coiling structure can also be modeled as a single straight channel structure similar to **Figure 2.1(b)** and filled with the original fluid with a refractive index of $\boldsymbol{n_0}$ but with an overall length of $\boldsymbol{L_{eff}}$.

By employing the equivalent model of the space-coiling structure, one can derive the transmission coefficient, denoted as *T,* for a normally incident plane wave. The equivalent model of conventional space-coiling metamaterials is based on the classical three medium acoustic transmissions in which the transmission coefficient can be derived as:

$$T = \frac{4}{\left(1+Z_2/Z_3+Z_1/Z_2+Z_1/Z_3\right)\mathrm{e}^{-ik_2 l_2}+\left(1-Z_2/Z_3-Z_1/Z_2+Z_1/Z_3\right)\mathrm{e}^{ik_2 l_2}} \quad (2.4)$$

In the case of the space-coiling metamaterial shown in **Figure 2.1(a)**, $l_2 = n_r t$ $Z_1 = Z_3 = \frac{\rho_1 c_1}{a}$ and $Z_2 = \frac{\rho_2 c_2}{d}$. Substituting the above parameters into Equation (2.4) and given that all media are composed of the same material, *T* may be calculated as:

$$T = \frac{4}{\left(1+\frac{a}{d}\right)\left(1+\frac{d}{a}\right)\mathrm{e}^{-ik_0 n_r t}+\left(1-\frac{a}{d}\right)\left(1-\frac{d}{a}\right)\mathrm{e}^{ik_0 n_r t}} \quad (2.5)$$

where k_0 is the wavenumber associated with the medium inside the zigzag channel, *a*, *d* and *t* (shown in **Figure 2.1(a)**) represent the unit cell width, channel width, and unit cell

length, respectively, and n_r is the relative refractive index discussed above. Please note that throughout the analytical derivations, the $e^{-i\omega t}$ convention has been considered, and one may reach the complex conjugate forms of the equations by following the $e^{i\omega t}$ convention.

In order to derive the relationship between phase and amplitude of the transmission coefficient, the denominator of Equation (2.5) has initially been simplified to the trigonometric form, and the transmission amplitude is subsequently determined in terms of the transmission phase:

$$T = |T| e^{i\theta} = \frac{1}{\cos(k_0 n_r t) - \frac{i}{2}(a/d + d/a)\sin(k_0 n_r t)} \tag{2.6}$$

From the above equation, the amplitude and phase can be derived as:

$$|T| = \frac{1}{|\cos(k_0 n_r t)|}\sqrt{\frac{1}{1+\frac{1}{4}(a/d + d/a)^2 \tan^2(k_0 n_r t)}} \tag{2.7}$$

$$\theta = \tan^{-1}\left(\frac{1}{2}\left(\frac{a}{d}+\frac{d}{a}\right)\tan(k_0 n_r t)\right) \tag{2.8}$$

From Equation (2.7) and (2.8), one can conclude that:

$$\frac{1}{|\cos(k_0 n_r t)|} = \sqrt{1+\frac{\tan^2\theta}{\frac{1}{4}\left(\frac{a}{d}+\frac{d}{a}\right)^2}} \tag{2.9}$$

Defining $S = \frac{1}{2}\left(\frac{a}{d}+\frac{d}{a}\right)$ and employing Equation (2.7, 2.8 and 2.9), the transmission amplitude in terms of the transmission phase may be derived as follows:

$$|T| = \sqrt{\frac{1+\frac{\tan^2(\theta)}{S^2}}{1+\tan^2(\theta)}} \tag{2.10}$$

Considering that the term S in Equation (2.10) is always greater than unity ($S \geq 1$), the amplitude of the transmission coefficient for any transmitted phase (θ) is bounded by:

$$\left|\cos(\theta)\right| \leq |T| \leq 1 \tag{2.11}$$

The lower bound occurs when the channel width (d) is significantly smaller than the unit cell width (a). To further validate the presence of the aforementioned bound on sound transmission through a space-coiled structure, the transmission coefficient has been derived analytically using the transfer matrix method (TMM). The details of the derivation using the TMM are discussed in Appendix A. Using the TMM, and by varying the geometries of the traditional space-coiling structure, a large set of solutions has been investigated, and the resultant transmission phase/amplitudes are depicted in **Figure 2.2**.

By comparing the bound (pink region) predicted by Equation (2.11) resulting from the equivalent model and the set of results from the TMM-based solution, it can be observed that the set of results using the TMM fall within the predicted transmission bound, thereby ensuring the validity of the bound represented in Equation (2.11). Given the presented transmission bound shown in **Figure 2.2**, it is apparent that the conventional space-coiling structure cannot be used for simultaneous phase and amplitude modulation. The bounded nature of the transmission phase and amplitude results in large portions of the phase-amplitude diagram being inaccessible and, consequently, simultaneous modulation of phase and amplitude is essentially precluded. Of note, however, the

conventional space-coiling structure is capable of modulating the amplitude of the transmitted acoustic wave in specific instances. By tailoring the unit cell design and targeting a transmission phase of either $\pi/2$ or $-\pi/2$, the complete range of amplitude modulation is accessible (0-1). Nevertheless, the capacity for simultaneous and independent modulation of phase and amplitude is highly limited in the conventional class of space-coiling structures.

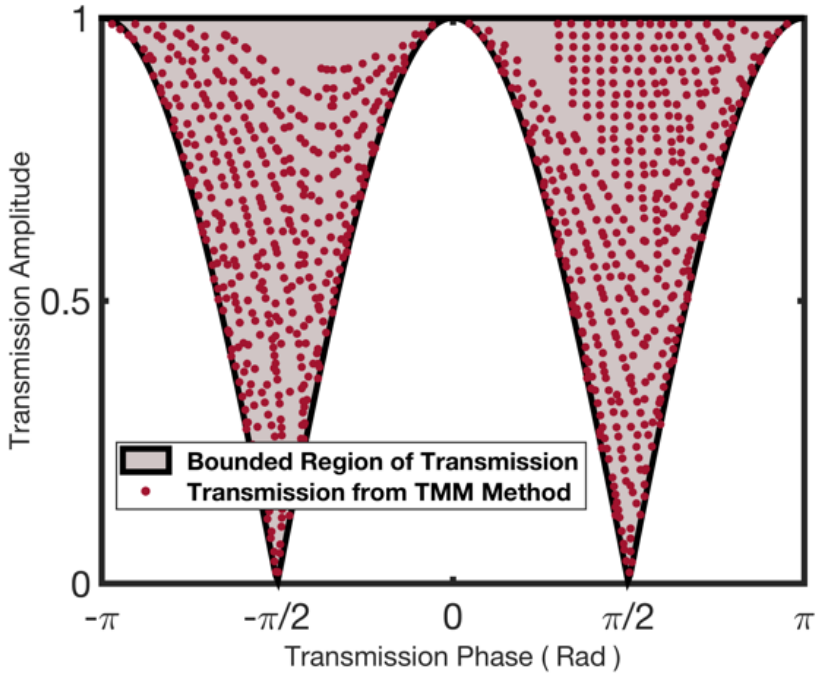

Figure 2.2. Phase and amplitude of the transmitted wave with conventional space-coiling structure. The colored region is the predicted space using the equivalent model. Scatter results shown by red dots are derived from the TMM-based approach by varying the geometry of the unit cell.

2.2. Generalized Complex Transmission Bound for the Arbitrary Metasurface

The transmission bound presented in the previous section has been derived for the space-coiling metamaterial structure. It is of utmost importance to explore how this bound is generalizable for any arbitrary metasurface and is not solely limited to space-coiling metamaterial. In this section, we investigate the origin of this transmission bound and analyze approaches to overcome this bound in order to yield full wavefront control.

Considering a general metasurface which is essentially a 2D form of metamaterial, with a thickness of L_m, the equivalent acoustic impedance of Z_m and wave number of K_m placed in infinite space with the acoustic impedance of Z, one may derive the following:

$$1-R=T\ [\ \cos(K_{\mathrm{m}}L_{\mathrm{m}})+\mathrm{i}\frac{Z}{Z_{\mathrm{m}}}\sin\left(K_{\mathrm{m}}L_{\mathrm{m}}\right)\ ] \tag{2.12}$$

$$1+R=T\ [\ \cos(K_{\mathrm{m}}L_{\mathrm{m}})+\mathrm{i}\frac{Z_{\mathrm{m}}}{Z}\sin(K_{\mathrm{m}}L_{\mathrm{m}})\ ] \tag{2.13}$$

In which R and T denote the reflection and transmission coefficients of the metasurface in a 2D space, respectively. Assuming a metasurface with purely real acoustic impedance (Z_m), the validity of the complex conjugate form of Equation (2.13) is ensured.

$$1+R^{*}=T^{*}\ [\cos(K_{\mathrm{m}}L_{\mathrm{m}})-\mathrm{i}\frac{Z_{\mathrm{m}}}{Z}\sin(K_{\mathrm{m}}L_{\mathrm{m}})] \tag{2.14}$$

In which the asterisks denote the complex conjugate operator. By multiplying the two sides of Equation (2.12) and Equation (2.14) with each other and assuming a passive, lossless metasurface ($|R|^2 + |T|^2 = 1$), the following may be derived:

$$R - R^{*} = \mathrm{i}\left|T\right|^{2} \sin\left(K_{\mathrm{m}} L_{\mathrm{m}}\right) \cos\left(K_{\mathrm{m}} L_{\mathrm{m}}\right) \left(\frac{Z_{\mathrm{m}}}{Z} - \frac{Z}{Z_{\mathrm{m}}} \right) \tag{2.15}$$

Additionally, by subtracting Equation (2.12) from Equation (2.13), it can be concluded that:

$$2R = \mathrm{i}T \left[\sin\left(K_{\mathrm{m}} L_{\mathrm{m}}\right) \left(\frac{Z_{\mathrm{m}}}{Z} - \frac{Z}{Z_{\mathrm{m}}} \right) \right] \tag{2.16}$$

By substituting Equation (2.16) into the Equation (2.15), one may readily derive the following:

$$\left|T\right| = \frac{\cos\left(\theta\right)}{\cos\left(K_{\mathrm{m}} L_{\mathrm{m}}\right)} \tag{2.17}$$

In which (θ) is the transmitted phase. Equation (2.17) demonstrates the general coupling between the transmission phase and amplitude from which the aforementioned bound shown in Equation (2.11) can be inferred. Notably, this bound exists for any arbitrary, passive, lossless metasurface with real acoustic impedance, regardless of the internal structure. Please note that for ultrathin metasurfaces ($K_{\mathrm{m}} L_{\mathrm{m}} \ll 1$), $\cos(K_{\mathrm{m}} L_{\mathrm{m}})$ goes to unity and the transmission amplitude will approach $\cos(\theta)$, similar to its electromagnetic counterpart's reported bound (Monticone et al., 2013).

The results obtained herein indicate that the key element for realizing full wavefront modulation is the presence of the acoustic reactance term in the metasurface acoustic impedance. For common acoustical fluids, by omitting the losses, the impedance will be a purely real quantity. However, with regards to the metasurfaces composed of acoustical lumped elements such as ports, cavities and resonators, the presence of the capacitive

behavior, leads to the emergence of the complex impedance. For metasurfaces with complex acoustic impedance, Equation (2.14) is no longer valid and may be altered to an alternate form from which a similar bound cannot be derived. Hence, in order to realize full acoustic control of the transmitted wave, we present a horn-like class of space-coiling structures featuring a gradient in channel spacing that possesses complex acoustic impedance and investigate its capacity for simultaneous phase and amplitude modulation.

2.3. Horn-like Space-coiling Metamaterial

To date, space-coiling metamaterial structures have been designed such that the zigzag channel width (d) remains constant throughout the length of the unit cell. In the previous section, we have demonstrated that this design methodology imposes a limited internal bound on acoustic transmission phase and amplitude, regardless of unit cell size or working frequency. Herein, a horn-like space-coiling structure is presented in which the gradual change in channel width leads to the presence of an imaginary term in the acoustic impedance of the metasurface. While the variation in channel width may be realized in many distinct forms (linear, periodic, arithmetic, geometric, etc.), this article will focus on a unique case of geometric progression of channel width, which resembles a horn-like shape. The horn-like structure presented herein shown in **Figure 2.3(a)**, instead of having a constant channel width throughout its length, features a change in width at each step governed by a constant common ratio (CR), defined as:

$$\mathrm{CR} = \frac{d_n}{d_{n-1}} \tag{2.18}$$

In which d_n and d_{n-1} are the channel width of n^{th} and $n\text{-}1^{th}$ coil respectively.

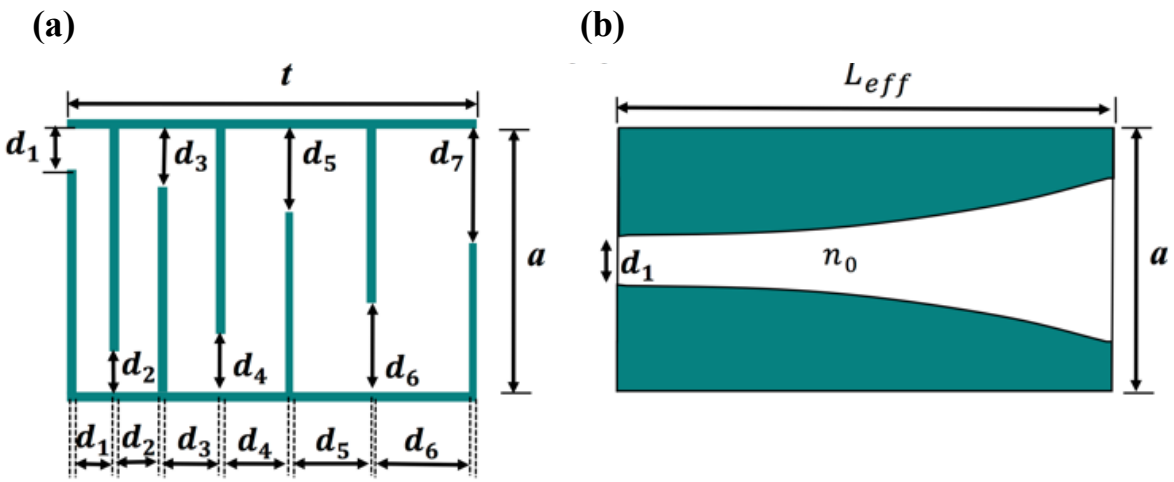

Figure 2.3. Horn-like space-coiling metamaterial unit cell and its equivalent model. (a) Horn-like space-coiling metamaterial structure composed of 6 coils is shown here in which d_n (n=1:6) represents the channel width at n^{th} coil, and d_7 is the channel width at the output port; channel widths follow the geometrical sequence with the common ratio in excess of one (CR >1). (b) Equivalent model of the gradient coil structure featuring a horn-shaped channel of length L_{eff} filled with original medium with a refractive index of (n_0).

By this definition, a structure with CR = 1 simply represents the conventional space-coiling metamaterial structure depicted in **Figure 2.1(a)**. However, for structures with CR>1, the zigzag channel can be well approximated as an exponential horn (**Figure 2.3(b)**) with a flare constant of:

$$m = \frac{N}{L_{\text{eff}}} \ln(\text{CR}) \tag{2.19}$$

Where N is the number of coils, and L_{eff} is the effective length of the zigzag structure.

The behavior of horn-like space-coiling metamaterials may be analyzed using the TMM approach presented in Appendix A, in which in Equation (A.7), each propagation tensor (T_i) will be computed based on the associated coil's geometry. However, due to the complexity of the aforementioned analytical solution, the use of an equivalent model to formulate the performance of the structure will be beneficial for markedly simplifying the

incorporation of this structure in various applications. In this section, the horn-like space-coiling structure has been approximated with the equivalent horn and, subsequently, the transmission coefficient based on the horn model has been derived.

The structure of the horn-like space-coiling metamaterial is shown in **Figure 2.4(a)**. In this structure, the effective length of the acoustic pathway can be approximated with:

$$L_{\text{eff}} = \sum_{b=1}^{b=N} L_b \tag{2.20}$$

Where:

$$L_b = \sqrt{(a - d_b)^2 + (w + d_b)^2} \tag{2.21}$$

In which N is the number of coils ($N = 5$ in the structure depicted in Figure 2.4a), and w is the wall thickness. By calculating d_b and L_b for each coil, the acoustic pathway profile through the horn-like space-coiling metamaterial has been illustrated for one arbitrary structure ($N = 10$, $w = 0.01$m, $d_1 = 5$mm, $a = 8.5$cm and CR = 1.3), shown in **Figure 2.4(b)** in red.

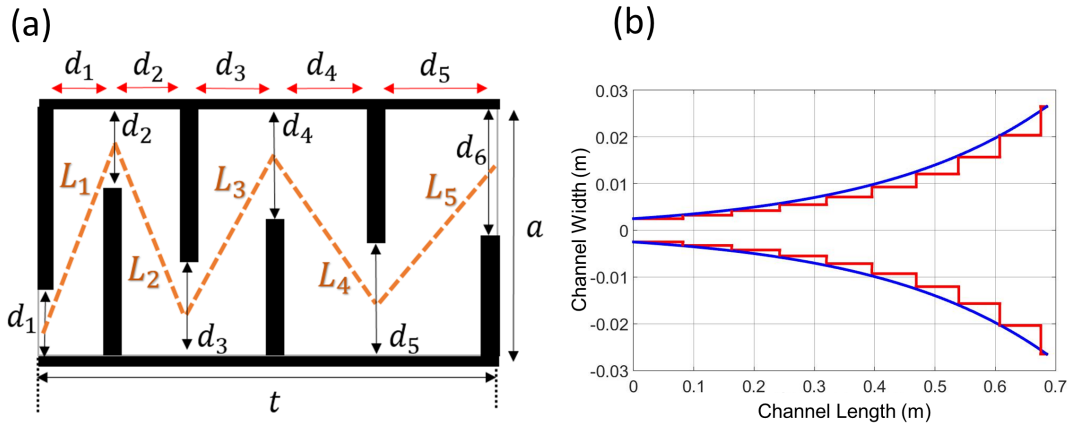

Figure 2.4. Space-coiling unit cell with a gradual change in channel width as an exponential horn. (a) Horn-like space-coiling metamaterial with an effective length of the acoustic pathway shown with orange dashed-line. (b) Comparison between the exact profile of the channel and the approximated horn model.

At each section of the pathway, the profile has a width of d_b and a length of L_b, both of which change from one coil of a given unit cell to another. From **Figure 2.4(b)**, it can be observed that the approximated horn-like profile, demonstrates a good approximation of the exact profile and may serve as the equivalent model of Horn-like space-coiling metamaterial. Next, using the equivalent model (**Figure 2.3(b)**), the acoustic transmission coefficient may be analytically derived using Webster's horn equation for velocity potential (Crandall, 1954).

$$\left(\frac{\partial^2}{\partial x^2}+m\frac{\partial}{\partial x}+k^2\right)\varnothing=0 \tag{2.22}$$

Where $\emptyset$ is the velocity potential, m is the flare constant, and k is the wave number. The solution of Equation (2.22) has the form of:

$$\varnothing=C_1\mathrm{e}^{\mu_1 x}+C_2\mathrm{e}^{\mu_2 x} \tag{2.21}$$

$$\mu_1=-\frac{m}{2}+\frac{i}{2}\sqrt{4k^2-m^2} \tag{2.22}$$

$$\mu_2=-\frac{m}{2}-\frac{i}{2}\sqrt{4k^2-m^2} \tag{2.23}$$

From the velocity potential obtained in Equation (2.21), one can calculate the pressure and velocity as:

$$V=\frac{\partial\varnothing}{\partial x}=C_1\mu_1\mathrm{e}^{\mu_1 x}+C_2\mu_2\mathrm{e}^{\mu_2 x} \tag{2.24}$$

$$P=-\rho\frac{\partial\varnothing}{\partial t}=-i\rho\omega(C_1\mathrm{e}^{\mu_1 x}+C_2\mathrm{e}^{\mu_2 x}) \tag{2.25}$$

Next, the pressure and velocity boundary conditions have been written at x=0 and x= L_{eff}.

At $x = 0$:

$$-i\rho\omega\left(C_1 + C_2\right) = P_{\mathrm{I}} + P_{\mathrm{R}} \tag{2.26}$$

$$C_1\mu_1 + C_2\mu_2 = \frac{a}{\rho c\, d_{\mathrm{in}}}\left(P_{\mathrm{I}} - P_{\mathrm{R}}\right) \tag{2.27}$$

At $x = L_{\mathrm{eff}}$:

$$-i\rho\omega\left(C_1 \mathrm{e}^{\mu_1 L_{\mathrm{eff}}} + C_2 \mathrm{e}^{\mu_2 L_{\mathrm{eff}}}\right) = P_{\mathrm{T}} \tag{2.28}$$

$$C_1\mu_1 \mathrm{e}^{\mu_1 L_{\mathrm{eff}}} + C_2\mu_2 \mathrm{e}^{\mu_2 L_{\mathrm{eff}}} = \frac{a}{\rho c\, d_{\mathrm{out}}}\left(P_{\mathrm{T}}\right) \tag{2.29}$$

From Equations (2.26) to (2.29), the complex transmission coefficient has been derived.

$$T = |T|\mathrm{e}^{i\theta} = \frac{4}{\left(-\frac{k}{\beta}\frac{a}{d_{\mathrm{out}}} + 1 + \frac{d_{\mathrm{in}}}{d_{\mathrm{out}}} - \frac{k}{\beta}\frac{d_{\mathrm{in}}}{a} + i\frac{\gamma}{\beta}\left(1 - \frac{d_{\mathrm{in}}}{d_{\mathrm{out}}}\right)\right)\mathrm{e}^{(\gamma + i\beta)L_{\mathrm{eff}}} + \left(\frac{k}{\beta}\frac{a}{d_{\mathrm{out}}} + 1 + \frac{d_{\mathrm{in}}}{d_{\mathrm{out}}} + \frac{k}{\beta}\frac{d_{\mathrm{in}}}{a} - i\frac{\gamma}{\beta}\left(1 - \frac{d_{\mathrm{in}}}{d_{\mathrm{out}}}\right)\right)\mathrm{e}^{(\gamma - i\beta)L_{\mathrm{eff}}}} \tag{2.30}$$

Where d_{in} and d_{out} are the channel width at the input and output ports, respectively, a is unit cell width (all are shown in **Figure 2. 3(a)**), k is wave number, and γ and β are defined as:

$$\gamma = \frac{m}{2} \tag{2.31}$$

$$\beta = \frac{1}{2}\sqrt{4k^2 - m^2} \tag{2.32}$$

In order to validate the applicability of the presented equivalent model for the horn-like

space-coiling structure, the results from the equivalent model have been compared with both a COMSOL numerical model and the exact analytical solution (transfer matrix method) presented in Appendix A. The structure considered herein has the following parameters: $N = 14$, $w = 1$cm, $d_1 = 3$mm, $a = 8.5$cm and CR = 1.2. The comparisons of the equivalent model with both the COMSOL model and the exact solution are shown in Figure I.6. From the results shown in **Figure 2.5**, it can be observed that the numerical results obtained from the simulated model in COMSOL Multiphysics are in precise agreement with the results of the TMM discussed in Appendix A (labeled herein as the exact model).

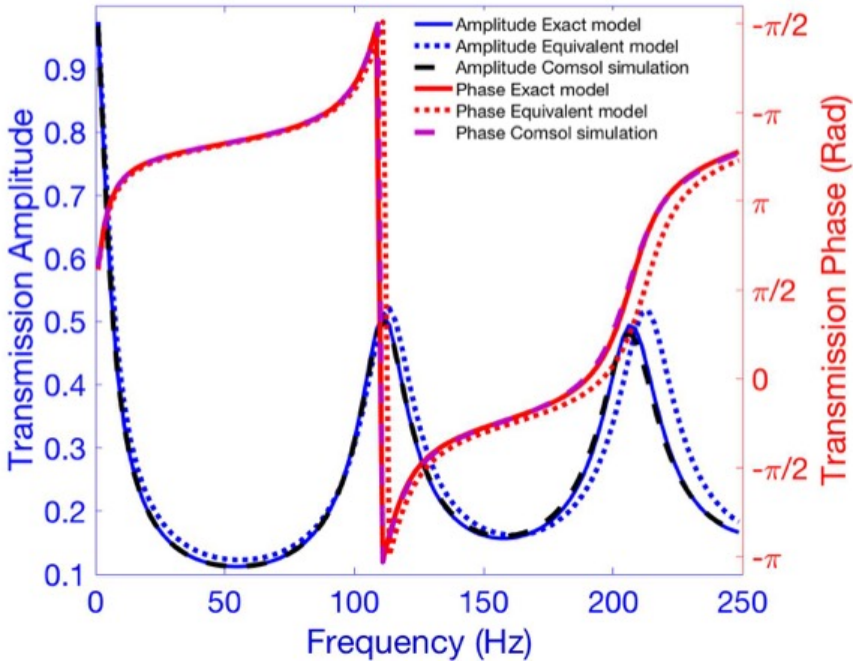

Figure 2.5. Transmission through horn-like space-coiling metamaterial derived from three different approaches. Exact model refers to the TMM presented in Appendix A, and the equivalent model refers to the horn-like model discussed here.

Moreover, the results from the equivalent horn-like model are in good agreement, with only small deviations from the exact model and the numerical results. This small discrepancy is largely due to the simple approximation of L_{eff} and can be improved with

the more exacting computation of this parameter. The presented equivalent model drastically simplifies the design of the Horn-like space coiling-metamaterial and readily provides a good initial estimate of structural performance for further experimental or numerical validation. Finally, using the equivalent horn-like model, the transmission bound similar to the one derived for conventional space-coiling metamaterials has been derived.

From Equation (2.30) and given the relation that $\gamma^2 + \beta^2 = k^2$, the transmission phase and amplitude can be derived as:

$$\theta = \tan^{-1}\left[\frac{k\left(\frac{a}{d_{\text{out}}}+\frac{d_{\text{in}}}{a}\right)\sin\left(\beta L_{\text{eff}}\right)}{\beta\left(1+\frac{d_{\text{in}}}{d_{\text{out}}}\right)\cos\left(\beta L_{\text{eff}}\right)+\gamma\left(1-\frac{d_{\text{in}}}{d_{\text{out}}}\right)\sin\left(\beta L_{\text{eff}}\right)}\right] \tag{2.31}$$

$$|T| = 2\mathrm{e}^{-\gamma L_{\text{eff}}}\sqrt{\frac{\frac{1}{(1+\frac{d_{\text{in}}}{d_{\text{out}}})^2}+\frac{\tan^2\theta}{(\frac{d_{\text{in}}}{a}+\frac{a}{d_{\text{out}}})^2}-\frac{4\gamma^2 d_{\text{in}}\tan^2\theta}{k^2 d_{\text{out}}(\frac{d_{\text{in}}}{a}+\frac{a}{d_{\text{out}}})^2(1+\frac{d_{\text{in}}}{d_{\text{out}}})^2}+\frac{2\gamma\,(1-\frac{d_{\text{in}}}{d_{\text{out}}})\tan\theta}{k(\frac{d_{\text{in}}}{a}+\frac{a}{d_{\text{out}}})^2(1+\frac{d_{\text{in}}}{d_{\text{out}}})^2}}{1+\tan^2\theta}} \tag{2.32}$$

In the case of a structure with close to unity CR and, consequently small flare constant of a frequency higher than that of the equivalent horn cut-off frequency, the ratio $\frac{\gamma}{k}$ would be small and has been omitted to simplify the equation. Thus, Equation (2.32) yields to:

$$|T| = \frac{2e^{-\gamma L_{\text{eff}}}}{\left(1+\frac{d_{\text{in}}}{d_{\text{out}}}\right)}\sqrt{\frac{1+\frac{\tan^2(\theta)}{S^2}}{1+\tan^2(\theta)}} \tag{2.33}$$

In which *S* is defined as:

$$S = \frac{\left(\frac{a}{d_{\text{out}}} + \frac{d_{\text{in}}}{a}\right)}{\left(1 + \frac{d_{\text{in}}}{d_{\text{out}}}\right)} \tag{2.34}$$

By substituting $\gamma = \frac{m}{2} = \frac{N}{2L_{\text{eff}}}\log(\text{CR})$, along with the fact that $\frac{d_{\text{in}}}{d_{\text{out}}} = \text{CR}^{-N}$, the transmission amplitude can be written as:

$$|T| = \frac{2}{\text{CR}^{N/2} + \text{CR}^{-N/2}} \sqrt{\frac{1 + \frac{\tan^2(\theta)}{S^2}}{1 + \tan^2(\theta)}} \tag{2.35}$$

It can readily be demonstrated that $S \geq 1$ & $\text{CR}^{(N/2)} + \text{CR}^{(-N/2)} \geq 2$, therefore, the transmission amplitude will be bounded:

$$\frac{2}{\text{CR}^{N/2} + \text{CR}^{-N/2}} \geq |T| \geq \frac{2}{\text{CR}^{N/2} + \text{CR}^{-N/2}} |\cos(\theta)| \tag{2.36}$$

Based on Equation (2.36), both the upper and lower bounds of the transmission amplitude are functions of the common ratio (CR) and the number of coils (N), and increasing these two parameters results in lowering both bounds. Thus, in order to validate Equation (2.36) and the bounds on the transmission coefficient for the horn-like space-coiling metamaterials, a limited range of the number of coils (N = 1-15) for four different values of the common ratio (CR = 1.1-1.4) are considered. Additionally, from the TMM-based approach, the set of results for different unit cell geometries, in accordance with the aforementioned range of N for each value of CR, have been obtained and are shown in **Figure 2.6**. For each structure with a distinct common ratio, the upper bound is constructed

with a value of N = 1, with a tiny decrease in the upper bound as a function of CR (≈ 0.98 for CR = 1 .4, for example). However, the lower bound is related to the highest N (N = 15, in this example analysis) and, consequently, the effect of variations in CR is enhanced and the lower bound may be significantly decreased (≈ 0.16 for CR = 1.4, for example). Of note, there exists a tradeoff between CR and the maximum allowable range of N given the fact that channel width at the output port (d_{out}) must remain smaller than the unit cell width (*a*). As illustrated in **Figure 2.6**, this class of horn-like space-coiling structures enables marked expansion of the coverage of the phase-amplitude diagram well beyond the inherent limits encountered in conventional space-coiling metamaterials.

The expansion of the coverage of the phase-amplitude diagram yields the realization of full wavefront manipulation through a simultaneous phase and amplitude modulation in gradient space-coiling metamaterials. Please note that expanding coverage of the phase-amplitude diagram is not the only criteria requisite to realizing full wavefront modulation using the proposed structure. Of critical importance is also the fact that, due to the classical and simple shape of the horn-like space-coiling metamaterials, the presentation of an analytical formulation is enabled, thereby easing the complexity of the design process.

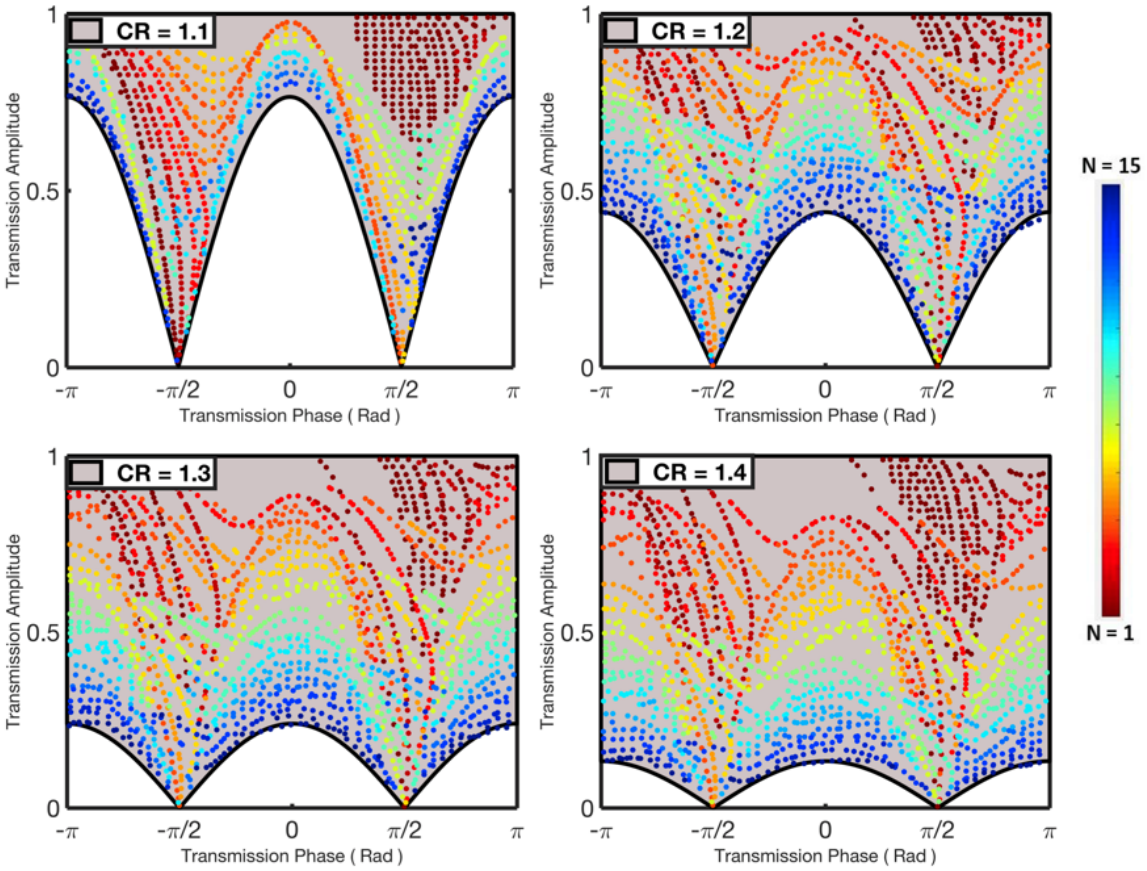

Figure 2.6. Illustration of the result space for gradient space-coiling metamaterials with varying common ratio (CR). The colored region (pink) is the region defined by Equation (2.36), and the dot points represent the results from TMM.

2.4 Full Wavefront Modulation Using Horn-like Metasurface

Subsequent to demonstrating the capability of Horn-like space-coiling metamaterials to expand the accessible transmission phase-amplitude region, metasurfaces comprised of these structures have been designed, targeting two distinct functionalities: sound focusing and acoustic beam splitting. The metasurfaces thusly designed herein feature 30 horn-like space coiling unit cells of identical width ($a = \lambda/6$) and length ($t = \lambda/2$) but distinct internal structures. While constant width and length of the unit cells is not requisite to achieving the intended functionalities, these constraints have been implemented to further demonstrate the ease of design using this class of horn-like space-coiling metamaterials. Please note that the unit cell's width plays a critical role in conversion efficiency, with smaller widths being preferable for optimal performance (Appendix B).

The internal structure of each unit cell (N, w, d_{in}, and CR) has been designed to generate the desired phase and amplitude in order to shape the transmitted acoustic wavefront. The first step undertaken herein in designing the metasurfaces was to derive the required phase and amplitude of the transmitted wave from each unit cell of a particular metasurface. To this end, the concept of time-reversal or the phase-conjugation method in the frequency domain have been utilized, given the capability for simultaneous phase and amplitude modulation. Implementing the aforementioned approaches in designing the metasurface allows for a drastic reduction in the computational expense when compared to phase-based metasurfaces in which rigorous optimization is required. The desired transmission amplitude-phase profile of the metasurface with regards to a given functionality may be obtained from both numerical and analytical approaches. Herein,

numerical techniques have been utilized for this step, since this approach may readily be generalized for any complicated profile, such as 3D acoustic holograms. Following the derivation of the requisite phase and amplitude of transmission at each unit cell, the internal geometry of the metasurface's unit cell has been designed analytically using the TMM approach and, ultimately, the entire metasurface in both lossy and lossless conditions has been simulated to visualize the targeted performance.

In the case of the focusing of the acoustic wave shown in **Figure 2.7(a)**, the metasurface has been designed to focus the sound at a focal point located two wavelengths from the metasurface. In order to determine the proper wavefront, a hypothetical monopole point source has been considered on the desired focusing spot and the resultant complex conjugate pressure has been calculated over the transmission side of the metasurface (right-hand-side). Next, given the plane wave incident on the left-hand-side of the metasurface, the desired transmission coefficient for each unit cell is computed, and the unit cell structures have been designed accordingly. With regards to the acoustic beam splitting shown in **Figure 2.7(b)**, two plane waves with angles of $\pi/12$ and $-\pi/12$ have been assumed on the transmission side of the metasurface, and the desired transmission coefficients at each unit cell have been calculated.

The sound focusing results are shown in **Figure 2.7(a)** in which the transmitted wave has been focused at the desired focal spot. As a common aim in focusing applications is the confinement of the acoustic wave power, the squared pressure (p^2) in **Figures 2.7(a)** and **2.7(c)** is depicted and corresponds to the resultant power. By employing the horn-like space coiling design, a high degree of focusing has been obtained.

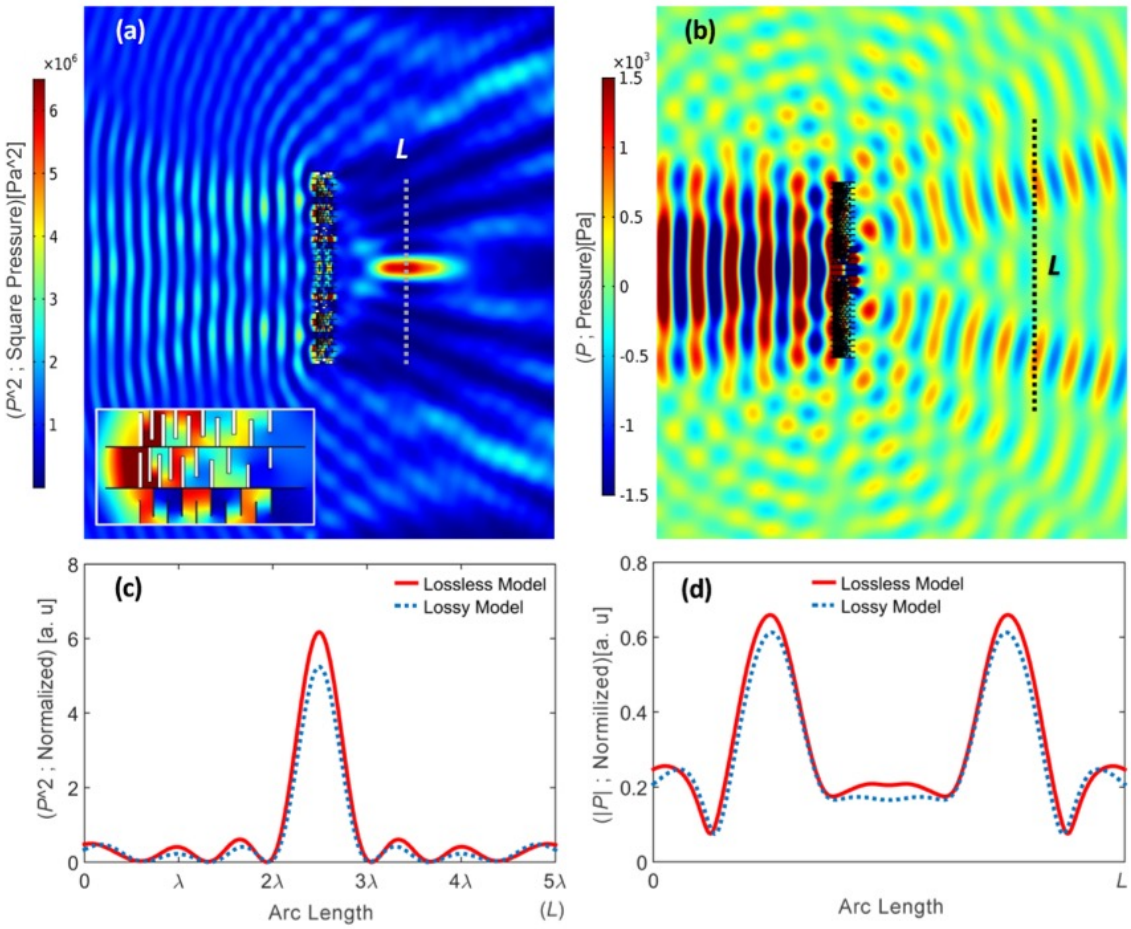

Figure 2.7. (a) Acoustic plane wave with an amplitude of 1kPa incident on the left-hand-side of the metasurface and the resultant focusing on the right-hand side. (b) Acoustic beam splitter that transforms the plane incident wave with the amplitude of 1kPa to two equi-amplitude beams in $\pi/12$ and $-\pi/12$ directions. (c) Pressure profile along the cut-line with the length of 5λ extending through the focal spot shown in Figure (2.5a). (d) Pressure profile along the cut-line placed at a distance of 5λ from the metasurface (2.5b). In Figures (2.5c) and (2.5d), the red line represents the data from the lossless simulation while the blue dotted line represents the data with the presence of loss.

In order to quantify the resultant focusing, p^2 is probed along the cut-line shown in **Figure 2.7(a)** and is depicted in **Figure 2.7(c)**. Notably, the pressure at the focal point is approximately 2.5 times the incident pressure, yielding power confinement on the order of 6. Moreover, the pressure profile depicted in **Figure 2.7(c)** successfully mimics the form of the Hankel function as the monopole source and a pressure power ratio of approximately

8 (6.3 peak at the focal region and 0.8 at the nearest peak to focal region) have been obtained.

Finally, the acoustic beam splitting results are shown in **Figure 2.7(b)** in which the normally incident plane wave on the metasurface has been divided into the two equi-amplitude beams in the desired directions. In order to quantify the results, an absolute pressure profile normalized by the incident beam's amplitude has been probed along the cutline and depicted in **Figure 2.7(d)**. It can be observed that the split beams maintain an amplitude of approximately 65% of the incident beam and an amplitude resolution of approximately 3 (0.65 in the beam regions and 0.2 in the region between the two beams) may be achieved with the designed metasurface.

In order to experimentally validate the proposed design methodology, a metasurface featuring the horn-like space coiling metamaterial design has been fabricated and tested. To this end, for the sake of simplicity, the reverse form of the sound focusing case has been experimentally validated in order to avoid the complexity associated with the practical generation of a plane wave in the near-field regime. Given the time-reversible nature of the proposed structure, if the point source is placed at a distance of two wavelengths from the metasurface, an identical metasurface to that having been designed for sound focusing may be employed to convert a cylindrical wave to a plane wave.

The acoustic metasurface was fabricated with a commercial 3D printer (Dimension SST 1200es) from Acrylonitrile-Butadiene-Styrene (ABS) plastic with a resolution of 0.2mm. The experimental setup is shown in **Figure 2.8** and is composed of two thick plywood sheets of dimensions 250cm x 250cm x 2.5cm placed in parallel with a spacing

of 2cm to create a 2D domain. Domain boundaries were confined with an absorbing foam 5cm in thickness to mitigate the back reflection with optimal performance at 1KHz. In order to realize an acoustic point source within this domain, a loudspeaker was coupled to a narrow tube outlet to generate a localized point source. In order to ultimately map the acoustic field, a measurement region defined with an appropriate offset from boundaries (~40cm) meshed with 190 equally spaced probing points with center-to-center spacing of 9cm. The experimental procedure was designed to be performed at a frequency of 1KHz, and associated dimensions and spacing have been realized accordingly. To map the field within the measurement region, two initially calibrated microphones (Audix TM1) have been used in which one microphone is fixed throughout the entire mapping procedure and the second microphone moved to sample all probing points. At each probing location, the

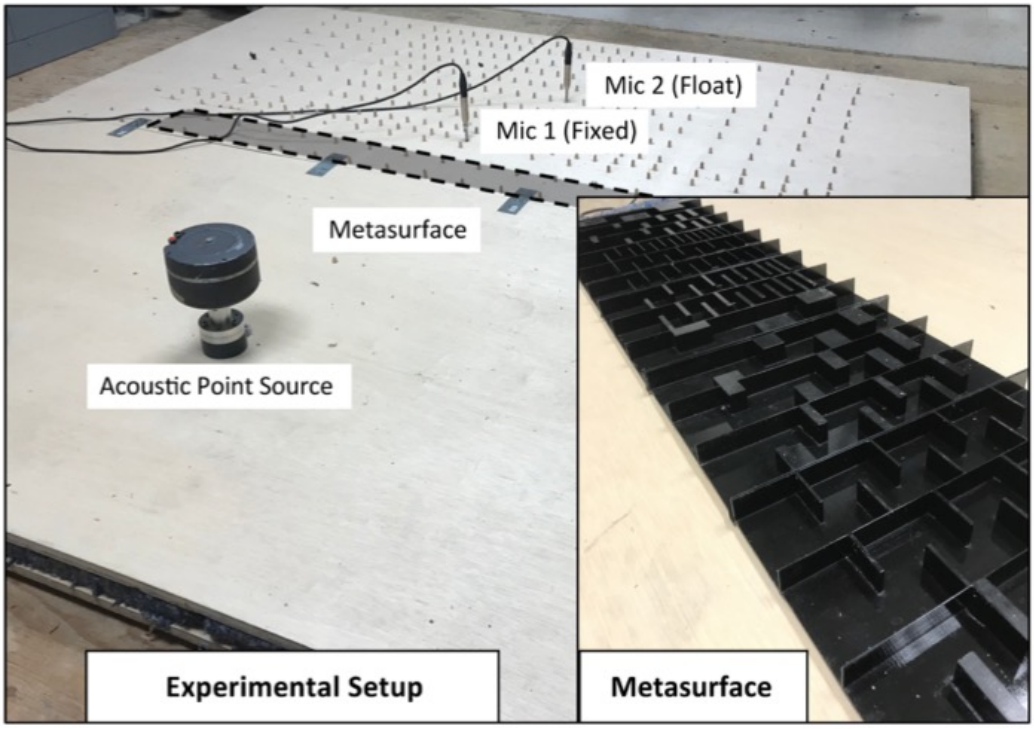

Figure 2.8. Experimental setup employed to map the resultant acoustic field in the specified region on the transmission side of the metasurface.

complex transfer function between the two microphone signals was calculated and averaged over ten readouts. Finally, spline interpolation was utilized to visualize the resultant acoustic field in the finer mesh. **Figure 2.9(a)** demonstrates the simulated resultant pressure profile in which the cylindrical wavefront originating from the monopole source has been reformed to yield a laterally confined plane waveform on the transmission side of the metasurface In order to visualize the experimental wave pattern, the resultant pressures on the transmission side of the metasurface shown in **Figure 2.9(a)**, have been measured both with and without the presence of the metasurface and results are shown in **Figures 2.9(b)** and **2.9(c)**. In **Figure 2.9(b)**, the normalized pressure in the absence of the metasurface is shown in which the acoustic wavefront represents a diverging cylindrical waveform.

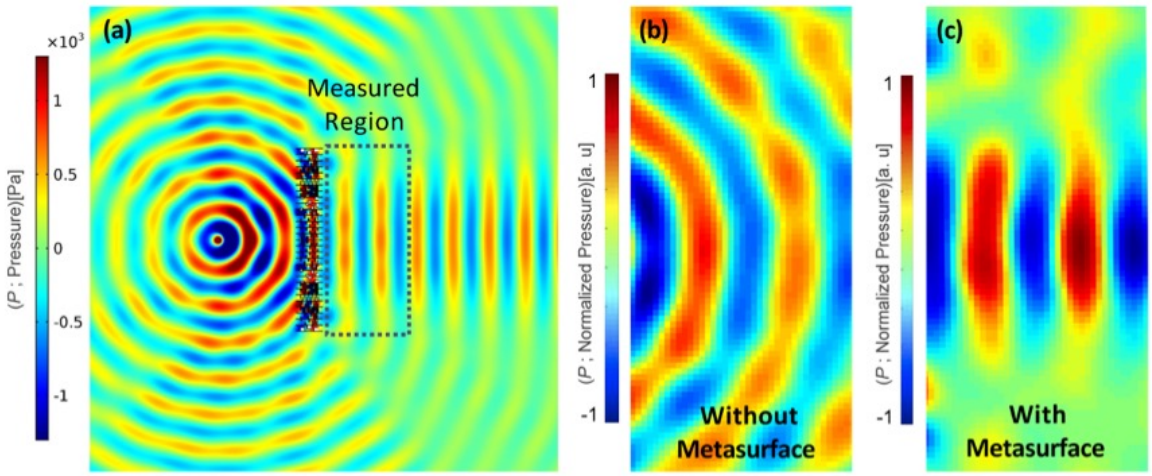

Figure 2.9. Numerical and experimental results of the reverse form of focusing in which a monopole point source is placed two wavelengths away from the metasurface, and a laterally confined plane wave is created on the transmission side. (a) Simulation results showing the cylindrical to plane wave conversion. Rectangular dotted region depicts the location in which the experimental acoustic wave pattern was mapped. (b) Measured normalized acoustic field in the absence of the metasurface. (c) Measured normalized acoustic field in the presence of the metasurface.

Please note that although the experimental domain is bounded with absorbing foam to mitigate reflection, the impedance mismatch at the domain boundary resulted in a minor and localized deviation of the pressure from the ideal form. **Figure 2.9(c)** demonstrates the resultant pressure field on the transmission side of the fabricated metasurface. The experimentally derived and normalized pressure field in the presence of the metasurface clearly demonstrates a laterally confined plane wavefront which is in good agreement with the pattern expected from the numerical solution, shown in **Figure 2.9(a)**.

Acoustic wave focusing, cylindrical-to-plane wave conversion, and beam splitting represent simple examples of acoustic wavefront manipulation analyzed herein in order to demonstrate the capability of gradient space-coiling metamaterials. Beyond acoustic wavefront manipulation, including the realization of more complicated acoustic patterns, metasurfaces may also be employed to mitigate the effects of aberrant layers by aberration correction. In all these cases, the precise design of the metasurface is simplified by the capacity for modulating both phase and amplitude. Moreover, the added degree of freedom to modulate the amplitude, in addition to phase, offers opportunities for performance that surpasses the capabilities of phase-based approaches (Appendix C).

The work presented in this chapter is founded on the basis of a well-known acoustic metamaterial structure, namely, space-coiling metamaterials and introduces a class of horn-like space-coiling metamaterials which provides sufficient degrees of freedom for full acoustic wave control. Moreover, the limitations of conventional space-coiling metamaterials for simultaneous phase and amplitude modulation were investigated, demonstrating that transmission through conventional space-coiling structures possesses a

topological-like bound, which is independent of frequency or unit cell dimension. Moreover, we have demonstrated that this bound applies to any passive, lossless metasurface with real acoustic impedance and highlighted the importance of the reactance term for full wavefront modulation. Next, a horn-like space-coiling structure capable of phase-amplitude modulation beyond conventional space-coiling structure limits is proposed and analyzed. Finally, metasurfaces featuring the proposed structures have been designed and simulated with the aims of sound focusing and acoustic beam splitting, while cylindrical to plane wave conversion has been experimentally validated (Details of the unit cells geometry have been listed in Appendix D). Horn-like space-coiling metamaterials offer a new methodology in metasurface design, in which phase and amplitude of the transmitted wave can simultaneously be modulated and tuned, yielding the capacity for complete wavefront shaping for a myriad of applications.

CHAPTER 3 DOUBLE DECORATED MEMBRANE METAMATERIAL: INITIAL EFFORT FOR REAL-TIME PHASE MODULATION

One of the fundamental challenges in the practical implementation of acoustic metamaterials science is the issue of tunability. To date, proposed acoustic metamaterial structures and devices suffer from narrow-band working frequencies and are typically passive structures. For example, with regard to phase modulation using metasurfaces, the tunability and capability of real-time phase modulation are critical in numerous applications ranging from biomedical ultrasound to acoustic communication. This chapter represents an initial step toward realizing acoustic metamaterials with the potential capacity of real-time phase modulation. Elaborately, herein, we have both numerically and experimentally investigated the possibility of phase modulation with minimal amplitude variation using a membrane-based class of acoustic metamaterials.

3.1 Transmission in Single and Double Decorated Membrane: Numerical Study

In the terminology of acoustic metamaterials, a decorated membrane refers to the combination of rigid mass with relatively small dimensions with respect to the overall size, which is attached to a membrane surface. Recently, implementations and applications of decorated membranes have gained growing interest, primarily in the context of perfect absorbers. Large transmission losses of a very low-frequency sound incident on a decorated membrane have previously been reported (Yang et al., 2015; Naify et al., 2010; Zhang et al., 2012). More recently, the application of a decorated membrane with the aim of phase modulation of the transmitted acoustic wave has been reported (Chen et al., 2014;

Langfeldt et al., 2016). In an effort to realize real-time tuning of the membrane-based metamaterial, Xiao et al, demonstrated that by placing a fishnet electrode in the vicinity of the decorated membrane and by applying a DC voltage to the electrode, the phase of the acoustic transmission wave may be modulated in real-time, yielding a tunable acoustic phase modulator (Xiao et al., 2015). The phase shift of the acoustic wave occurs due to the vibro-acoustic coupling of the membrane and incident sound field in which a phase shift of approximately 180 degrees occurs near the first Eigenfrequency of the membrane. The subsequent application of a DC voltage creates an anti-restoring force that decreases the Eigenfrequency of the membrane and consequently yields a tunable structure for phase modulation. For validation of this concept, we developed a FEM model of the decorated membrane in the waveguide coupled with the electrostatic field. The phase and amplitude spectra of the transmitted wave associated with different applied voltages are shown in **Figure 3.1**.

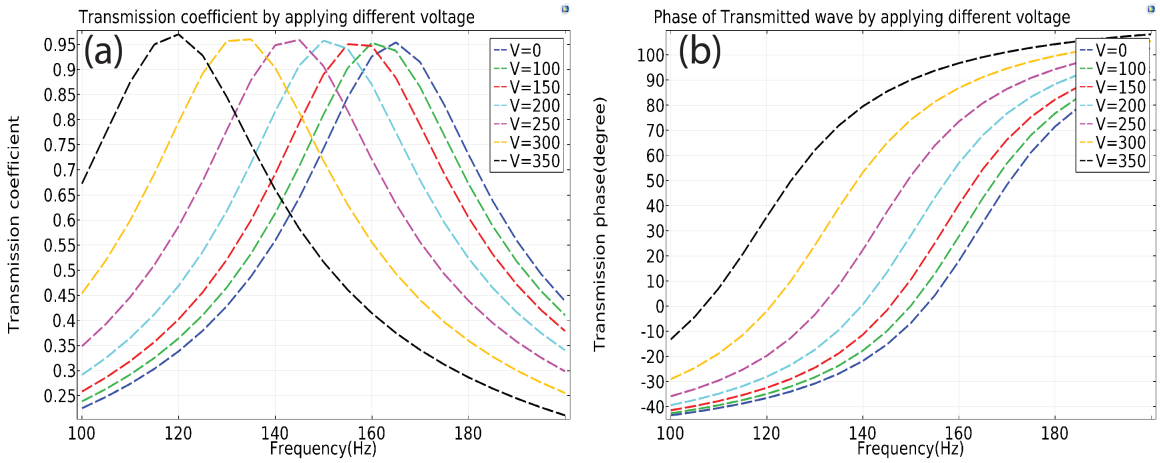

Figure 3.1. Complex transmission through the single decorated membrane. (a) Transmission amplitude for different values of the applied voltage. (b) Transmission phase for different values of the applied voltage.

As is shown in **Figure 3.1(a)**, by increasing the DC voltage, the Eigen frequency of the membrane shifts towards lower values, and the peak of the transmission coefficient shifts leftwards towards lower frequencies. Similarly, the phase of the transmitted wave shifts leftwards with an increase in the DC voltage, illustrated in **Figure 3.1(b)**. The shift of the phase of the transmitted wave enables control over the acoustic phase by varying the magnitude of the DC voltage. For example, based on the results obtained, increasing the voltage from 0 volts to approximately 350 volts yields a change in the phase of the transmitted wave from -20 to 80 degrees at a frequency of 143 Hz. Despite the fact that tunable phase modulation can be realized with this structure, the associated amplitude changes impose an inherent limitation in the intended application of the proposed structure as a metamaterial in which each unit cell mimics a discrete element of a phased array transducer. The ultimate aim of this part of this dissertation is to investigate the possibility of tuning the phase of the transmitted wave independent of the variation in amplitude by employing the decorated membrane metamaterial.

In an effort to achieve acoustic control, a structure composed of two decorated membranes in series in the waveguide has been designed. In this proposed unit cell structure, two decorated membranes are located in parallel to each other and separated by a precise, requisite distance. Each decorated membrane is modeled in the vicinity of a fishnet electrode, enabling the introduction of a desired distinct voltage for each membrane. Preliminary analyses of the capability of this structure to decouple phase and amplitude have been undertaken. The unit cell composed of two decorated membranes is found to exhibit two resonances, the first resonance occurring when the two membranes are moving

in phase during which the trapped region between the two membranes will undergo a simple displacement (**Figure 3.2(a)**). The second resonance occurs when the two membranes are out-of-phase, during which the trapped region will be under compression and expansion (**Figure 3.2(b)**). It is expected that the first resonance would be dominated by the mechanical characteristics of the membrane, such as the membrane equivalent spring constant, while the second resonance would be more affected by the geometric characteristics of the trapped region, such as the spacing length between the two decorated membranes. This concept has been numerically investigated by varying the spacing between the membranes in the unit cell and analyzing the transmission amplitude and phase, the results of which are shown in **Figure 3.2**. The phase and amplitude of the transmitted wave are depicted for three different non-dimensional parameters of L/D in which L denotes the spacing length between two membranes and D stands for the diameters of the membranes. **Figure 3.2(a)** demonstrates the fact that by changing the spacing length between the two membranes, the first resonance frequency remains constant. In fact, even in the case of large variations of 1 to 10 in L/D parameters, the first resonance frequency remains unchanged.

In contrast, however, by increasing the spacing between the two membranes, the second resonance associated with out of phase membrane vibration shifts towards lower frequencies. By tuning the membranes properties and spacing between them, the out-of-phase resonance may emerge in the vicinity of the in-phase resonance, thereby creating a broadband transmission peak instead of the single peak obtained previously. In addition, with regards to phase, 180-degree phase shift associated with the in-phase resonance is

obtained followed by secondary 180-degree phase shift corresponding to the out-of-phase resonance (**Figure 3.2(b)**). Please note that the sudden change in phase is related to the nature of the argument function defined in COMSOL as ranging from -180 to 180 degrees and in reality the phase shift is continuous.

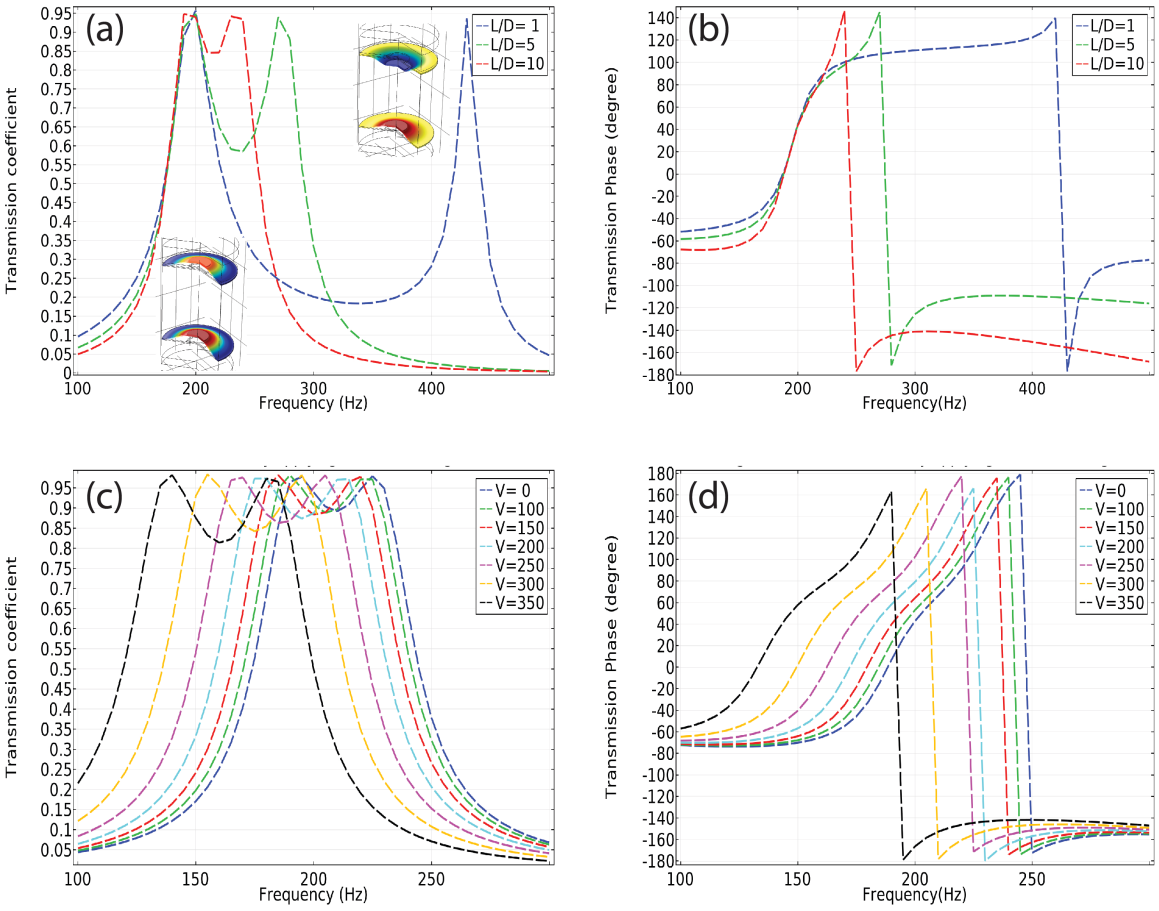

Figure 3.2. Complex transmission through the double decorated membrane. (a) Transmission amplitude for the different spacing of the membranes and occurrence of in-phase and out-of-phase resonances. (b) Transmission phase for the different spacing of the membranes and occurrence of Pi phase shift for both in-phase and out-of-phase resonances. (c) Transmission amplitude for merged resonances in the optimized double decorated membrane. (d) Transmission phase for merged resonances in optimized double decorated membrane structure.

The preliminary results obtained herein are promising due to the possibility that by tailoring the membrane's properties and spacing between them, the second resonance may be

coupled with the first resonance, thereby resulting in a broadband transmission peak. For initial validation of this concept, a unit cell composed of two decorated membranes has been modeled numerically. It should be noted that despite the fact that the applied DC voltage to each membrane may ultimately be adjusted individually, for the analysis performed herein, an identical voltage was applied at both membranes for purposes of the initial validation of this design. Two membrane models have been constructed with membrane and waveguide diameters of 20 mm and a 250 mm spacing distance between membranes. Amplitude and phase of the transmitted wave were recorded at varying frequencies as a function of applied DC voltage, illustrated in **Figure 3.2(b) &(c)**. The results demonstrate that at a constant frequency of approximately 187 Hz for values of the applied voltage ranging from 0 to 350 volts, the transmission coefficient ranges between 0.85 and 0.95, while in the case of a single decorated structure, the transmission coefficient ranges from 0.60 to 0.95. With regards to the transmission phase, our preliminary efforts have realized an amplification of the potential phase change due to the second resonance. Therefore, at a frequency of 187 Hz, a phase change from -25 degrees to 155 degrees has been obtained.

The realization of the phase shift approximating 180 degrees with only 10% change in the transmission coefficient strongly supports the potential of this approach towards the ultimate goal of a complete decoupling of phase and amplitude. Notably, in the numerical results obtained herein, due to the complex and multiphysics nature of this phenomena, to simplify the modeling step, thermal and viscous losses have been ignored.

3.2 Transmission in the single and double decorated membrane: Experimental study

Next, in order to investigate the effect of loss and validate the possibility of decoupled phase modulation using a double membrane metamaterial, the transmission has been measured experimentally for both single and double decorated membrane structure.

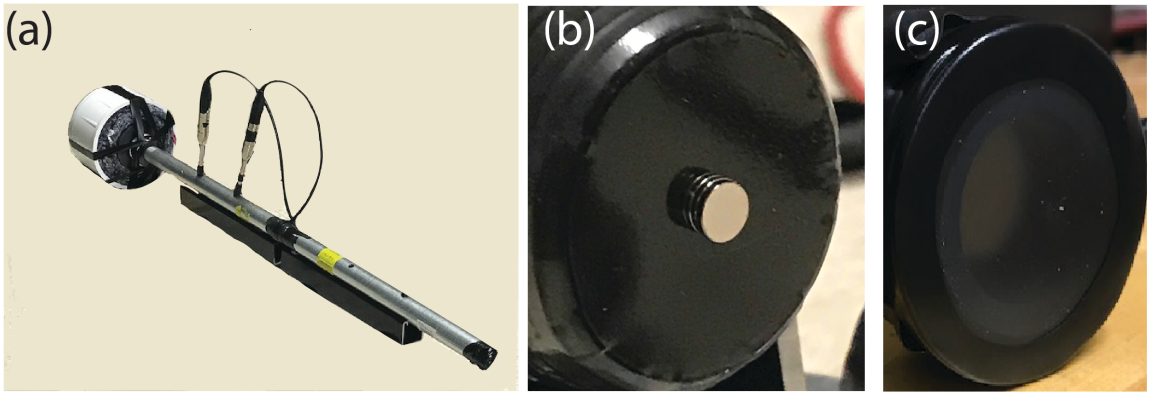

Figure 3.3. Experimental apparatus. (a) Impedance tube setup. (b) single decorate membrane. (c) double membrane with no attached mass.

The experimental apparatus is shown in **Figure 3.3**. To measure the complex transmission through the decorated membrane, an impedance tube setup featuring a steel pipe with a diameter of 2.5cm shown in **Figure 3.3(a)** is employed. The diameter of the impedance tube waveguide is selected considering the reliable range of frequency for measurement and based on the expected resonance frequency range of the membranes. The membrane is composed of a silicon rubber sheet under tension with the thickness of 0.3mm and the magnets with the diameter of 3mm and thickness of 1mm and weight of 40mg is leveraged to act as an attached mass on the membrane. Single membrane and double membrane configurations are shown in **Figure 3.3(b) & (c)**, respectively.

Initially, using the impedance tube setup, the complex transmission through the single decorated membrane has been measured. In this experiment, in order to evaluate the concept of the coupling the resonances discussed before, instead of applying voltage to tune the membrane's Eigenfrequency, the attached mass has been altered to realize resonance shift. Notably, multiple strategies may be pursued to manipulate the vibrational and resonance identity of the membrane which may analytically be modeled in one dimension as a form of the beam (Mehrvarz et al., 2018; Khodaei et al., 2018; Ardekany et al., 2018; Mehrvarz et al., 2019). Shown in **Figure 3.4**, the transmission amplitude and phase for three different configurations of the single decorated membranes with the resonances of 115Hz, 112Hz, and 107 Hz are demonstrated. From **Figure 3.4(a)**, it may be observed that the acoustic transmission trough decorated membrane is generally small except in the vicinity of the resonance, where the transmission amplitude has been increased in a narrow band of the frequency.

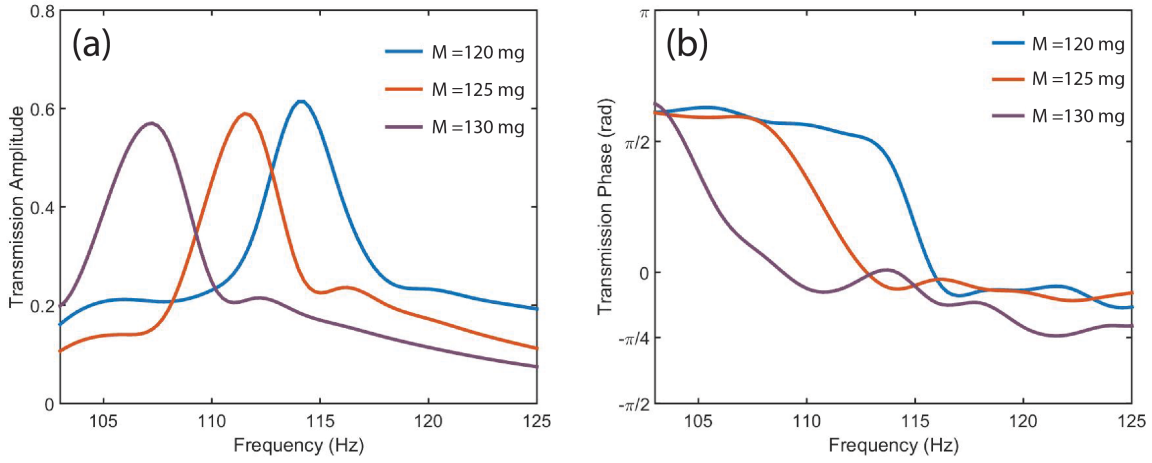

Figure 3.4. Experimentally obtained complex transmission for single decorated membrane. (a) Transmission amplitude for three different masses attached on the membrane. (b) Transmission phase for three different masses attached on the membrane.

Moreover, and expectedly, the transmission phase (**Figure 3.4(b)**) undergo a nearly Pi phase shift due to the resonance. Notably, due to the thermal and viscous boundry layer loses both the peak of transmission and range of phase shift is smaller than the theoretically expected values.

Following experimentally measuring the complex transmission through the single decorated membrane, the transmission through the proposed double decorated membrane structure is measured. In this experiment, the membrane's properties, i.e., attached masses along with the spacing between membranes have been tuned to merge the in-phase and out-of-phase resonances. The complex transmission results through a double membrane structure are shown in **Figure 3.5** for three different combinations of the masses and the spacing of 3cm. M_1 and M_2 denote the attached mass condition on the first and second membranes respectively represented based on the multiplication of m as the mass of each magnet (= 40 mg.). From **Figure 3.5(a)** and **Figure 3.5(b)**, it may be observed that in the first case when M_1= 2m and M_2=0, the in-phase and out-of-phase resonances are not merged. The transmission amplitude in this condition only possesses one peak and transmission phase has only varied by approximately Pi. In the other two cases, where M_1=2m and M_2=2m or 3m, the in-phase and out-of-phase resonances have emerged in close vicinity of each other. In these cases, the transmission amplitude possesses two peaks, and the transmission phase has varied over a range of about 2Pi.

Despite the successful demonstration of coupling between in-phase and out-of-phase resonances, strong damping has been observed in the out-of-phase resonances. The strong damping observed herein may be associated with three different sources of acoustic

energy losses. Commonly, the acoustic loss occurs near the boundaries of the media with the waveguide/membrane in the form of thermal and viscous losses (Pierce, 1989). These two sources of losses may be quantified with the viscous and thermal boundary layer thickness, which are approximated to be in the order of sub-millimeters in the experimental condition herein. Thereby, it is unlikely that the observed dampening is associated with thermos-viscous losses. The third potential source of energy loss, which is relevant in this particular experiment is the escape of the entrapped air. The out-of-phase resonances of the membranes essentially rely on the compression and expansion of the air isolated between the membranes. In this condition, the entrapped air exhibits a breathing mode generating pressure fluctuation in this region. For imperfect air-sealed condition, the pressure fluctuation in this region will be strongly mitigated due to the air transport and the breathing mode will be damped.

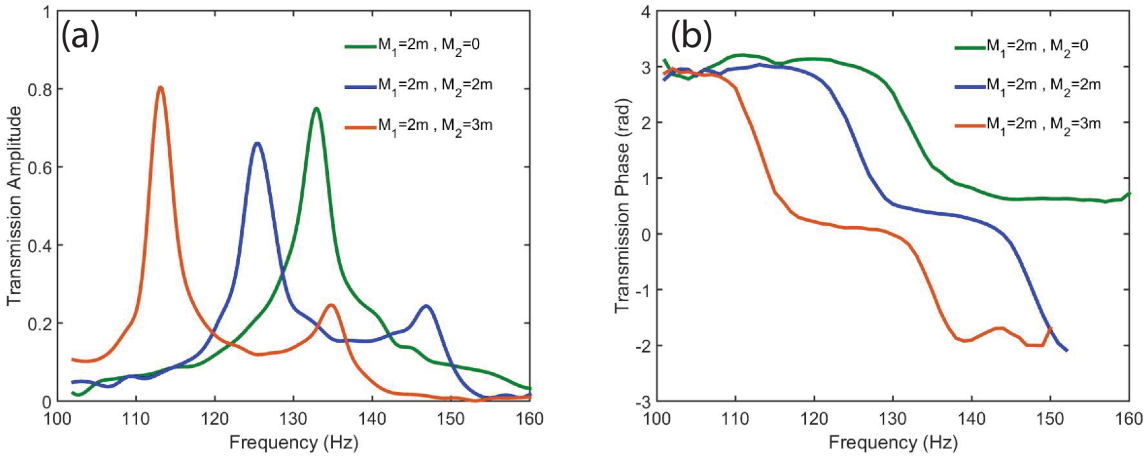

Figure 3.5. Complex transmission through the double decorated membrane. (a) Transmission amplitude for three different combinations of masses attached on the membranes. (b) Transmission phase for three different combinations of masses attached on the membrane.

To assess the contribution of different loss mechanisms discussed herein, two further experiments have been conducted. In the first experiment, the region between two membranes has been filled with Xenon for which the thermal and viscous losses are about half of those air. In the second experiment, instead of the silicon rubber sheet, Mylar rubber is leveraged, which is significantly less permeable. Notably, the potential air transport in the experimental apparatus may occur through both membrane and membrane/spacer attaching point.

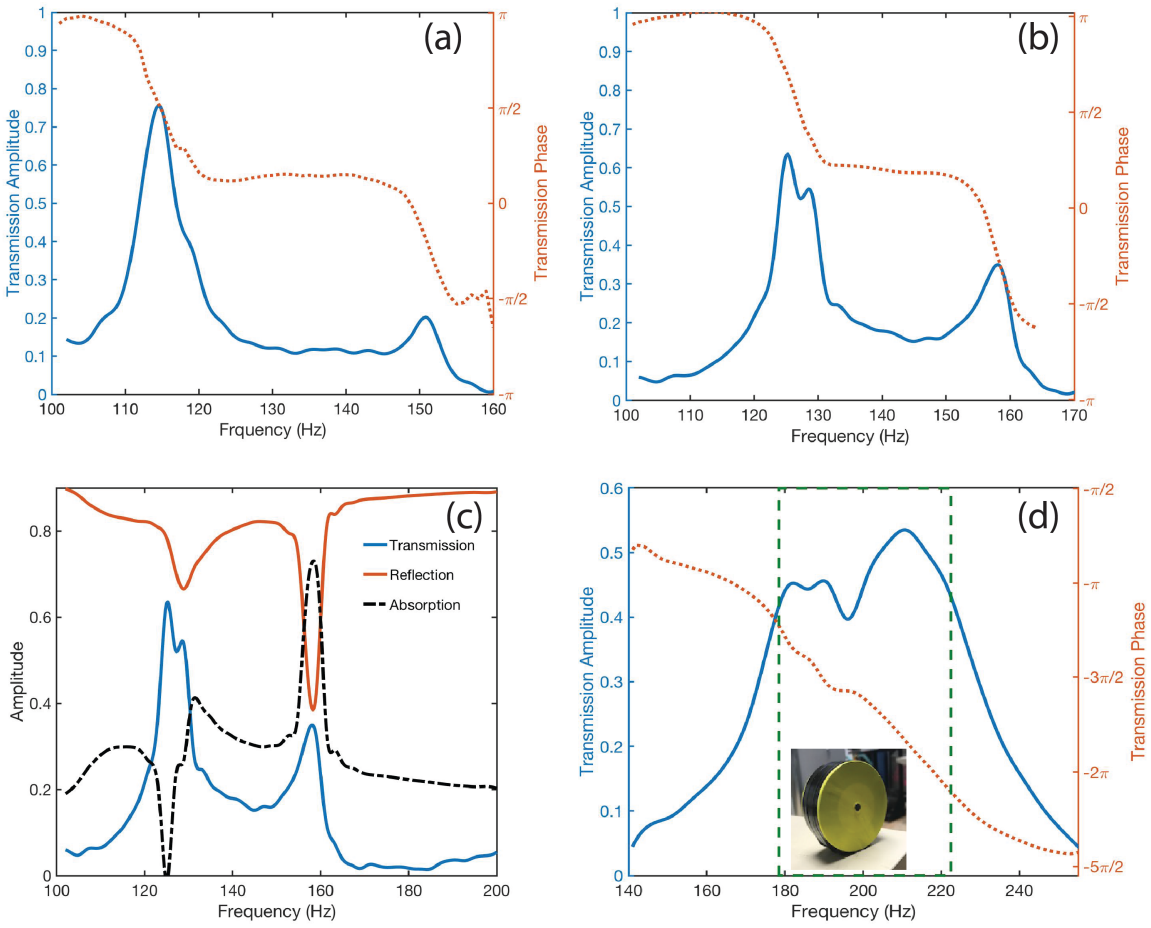

Figure 3.6. Experimental result for double decorated membrane when M_1 and M_2 are both equal to 2m and with the spacing of 3cm between membranes. (a) Transmission through Xenon filled double membrane. (b) Transmission through double Mylar membrane. (c) Transmission, Reflection, and Absorption in double Mylar membrane. (d) Coupled transmission in double Mylar membrane.

Considering that the practical realization of an air-tight setup is not trivial, the experiment leveraging a Mylar membrane has been conducted herein solely to identify and validate the source of losses in the observed results. The results are shown in **Figure 3.6**. Transmission through Xenon filled double membrane is shown in **Figure 3.6 (a)**. Expectedly, given the fact that thermal and viscous boundary layer thicknesses are minimal (dominated by thermal loss; Xenon: about 0.1 mm and Air: about 0.2mm) compare to the length scale in the experiment (2.5cm), the resulted transmission is found to be very similar to the air-filled case. On the other hand, from the results obtained in case of double Mylar membrane shown in **Figure 3.6(b)**, a marked enhancement in the transmission amplitude of out-phase-resonance may be observed. The transmission amplitude at out-phase-resonance has been approximately doubled in case of Mylar membrane with respect to the silicon rubber membrane.

From the results obtained herein, one may infer that the dampening mechanism observed for the out-of-phase resonance is strongly dominated by the presence of air transport. In **Figure 3.6 (c)**, the absorption coefficient of the double Mylar membrane is shown from which sudden enhancement of the absorption due to the discussed loss mechanism is observed near the out-of-phase resonance. Moreover, with an effort to better seal the Mylar membrane/spacer and adjusting the membrane's properties, two resonances have been successfully overlapped, and the resulting complex transmission is shown in **Figure 3.6 (d)**. It may be observed that, unlike single decorated membrane metamaterial, a broad pass-band (179-222 Hz) is obtained in which the amplitude variation remains small (0.4-0.54) despite the large phase change in this region.

From the presented numerical and experimental study, it may be concluded that by leveraging the double decorated membrane structure and by tuning the membrane's properties and spacing between them, in-phase and out-of-phase resonances may be coupled to provide a sufficient degree of freedom to modulate transmission phase with minimal amplitude variation. Moreover, it is validated experimentally that the achievement of such broadband region with a high level of transmission, relies strongly on the realization of an air-sealed double membrane structure. With the air-sealed double decorated membrane, one may couple the two resonances and subsequently realize a tunable metamaterial in which by adjusting the membrane's resonance frequency, transmission phase may be modulated in a broad range with the minimal amplitude variation.

CHAPTER 4 ULTRA-OPEN ACOUSTIC METAMATERIAL SILENCER

Airborne sound attenuation has conventionally been realized through the application of acoustic barriers, by either reflecting or absorbing incident acoustic energy. While wideband attenuation may be obtained, attenuation in the low-frequency regime (<500Hz) using such approaches is challenging and necessitates increased acoustic barrier layer thickness. Furthermore and importantly, such methods of sound attenuation eliminate the passage of air, precluding their functionality for applications in which ventilation is required. The need for sound attenuation, while preserving ventilation such as required in the application to mitigating fan noise, has inspired a range of efforts, often within the context of duct acoustics (Selamet et al., 1999; Huang et al., 2006; Wang et al., 2008; Lee et al., 2012; Sellen et al., 2006). Among prior efforts, Herschel-Quincke (HQ) waveguides (Stewart, 1928) are notable as narrowband sound attenuation may be achieved with minimal reduction in the duct air-flow area. Despite the performance of these classical methods for simultaneous sound attenuation and ventilation, their inherent in-duct nature, along with their large physical footprint, have limited their versatility and degree of implementation.

More recently, with ongoing advances in metamaterial science, new possibilities for manipulating acoustic energy have emerged. Metamaterials are composed of sub-wavelength structures in which their effective acoustic properties are dominated by their structural shape rather than their constitutive materials. Utilizing sub-wavelength metamaterial structures, phenomena such as wavefront modulation (Xie et al., 2014; Ghaffarivardavagh et al., 2018; Li et al., 2014), sub-diffraction imaging (Zhu et al., 2010;

Lu et al., 2012), and acoustic cloaking (Chen et al., 2007; Cummer et al., 2008), among others, have been demonstrated. To date, several acoustic metamaterial-based structures have been proposed to address the challenge of sound attenuation while simultaneously preserving air passage (Jung et al., 2018; Shen et al., 2018; Wu et al., 2018; Kim et al., 2014; Ma et al., 2013; Chen et al., 2015; García-Chocano et al., 2012). Despite the fact that the reported structures possess a sufficient degree of transmission loss in their designed frequency ranges, the amount of open area of the structures has been sacrificed in order to obtain the desired acoustic performance. Therefore, the ventilation areas of the reported structures are limited to small fractions of the overall area, which, while suitable for air permeability, are problematic in applications of forced ventilation, such as in the case of cooling fans. Recently, Li et al. (Li et al., 2018), proposed a metamaterial structure composed of side resonator with the micro-perforated plates that can absorb the acoustic wave at certain frequencies, while maintaining efficient ventilation. A primary focus of ongoing efforts in this area has been the broadening of the attenuation frequency band, which is substantial in applications of ambient noise reduction, but not requisite in the case of industrial noise such as machinery or fans, which is harmonic in nature. For instance, in the case of fan noise, the radiated sound is mainly composed of the tonal sound corresponding to the blade-passing frequency (BPF) and its higher harmonic modes (Lauchle et al., 1997; Niu et al., 2012). Similarly, in case of machinery noise, such as engine noise, the radiated sound is mainly composed of higher order harmonics based on the cylinder firing rate (CFR) or the engine firing rate (EFR) (Alfredson et al., 1970).

In this Chapter, we present a design methodology based on Fano-like interference

for selective attenuation of the transmitted acoustic wave by means of reflection. The method reported herein enables the design of ultra-open metamaterials (UOM) composed of sub-wavelength unit cell structures featuring a predominately open area that provide appropriate functionality when both sound attenuation and highly efficient ventilation are required. Moreover, the presented structures are capable of attenuating the acoustic wave at the targeted frequency as well as its higher harmonics and are therefore readily applicable to attenuate machinery or fan noise. Through the realization of high-performance sound attenuation, while retaining airflow, the design methodology enabling UOMs may serve as the foundation of a new generation of acoustic silencing technologies.

4.1 Fano-like Interference in Transverse Bilayer Metamaterial

Fano was the first to have derived a theory underpinning the asymmetric scattering peaks of electrons during his studies of autoionizing resonance (Fano, 1961). The origin of the asymmetric scattering profile was explained as a result of the interference between the discrete resonant and continuum states. Recently, given the analogies between the physics of phonon and electron scattering (Fellay et al., 1997), the asymmetric scattering of the elastic wave in sonic and Phononic crystals based on Fano-like interference has been demonstrated (Goffaux et al., 2002; Sainidou et al., 2006). This asymmetric transmission profile is due to the fact that the portion of the elastic wave traveling through the resonating element interferes with the portion of the elastic wave traveling through the non-resonating pathway. The asymmetric transmission profile possesses a dip region due to destructive interference resulting in attenuation of the transmitted wave. This property of attenuation

of the acoustic wave due to Fano-like interference has the potential for applications in acoustic filtering and silencing devices and represents the foundations of the ultra-open metamaterial (UOM) reported herein.

Initially, it is analytically demonstrated that such an asymmetric transmission profile based on a Fano-like interference is present in the case of a transverse bilayer metamaterial shown in **Figure 4.1**. Subsequently, the applicability of the presented metamaterial structure, providing both analytical and experimental validation of a novel acoustic silencing technology is demonstrated.

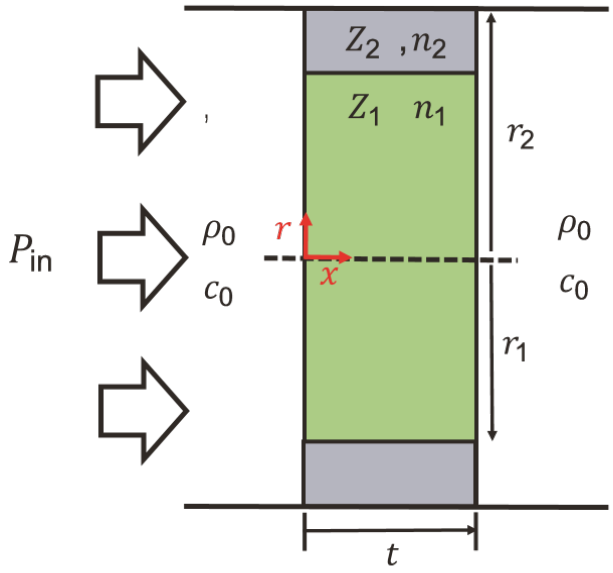

Figure 4.1. Transverse bilayer metamaterial in which the two colored regions possess distinct acoustic properties and are placed transversely with respect to the wave propagation direction

Firstly, we consider the case of an acoustic plane wave incident on a transverse bilayer metamaterial with distinct acoustic properties, as shown in **Figure 4.1**. It is assumed herein that the metamaterial has an axisymmetric configuration with respect to the x-axis with a thickness of t in which region 1 ($r < r_1$) is composed of a material with an acoustic

impedance of Z_1 and refractive index of n_1 and region 2 ($r_1 < r < r_2$) is composed of a material with an acoustic impedance of Z_2 and refractive index of n_2. Note that the axisymmetric configuration is selected solely for the purpose of simplification and other configurations may be considered without a loss of generality. Notably, it is assumed herein that two regions are separated with the acoustically rigid spacer at ($r = r_1$) of negligible thickness that eliminates the cross-coupling between them. Furthermore, the entire structure is assumed to be confined within a rigid, circular waveguide filled with a medium with the sound speed of c_0 and density of ρ_0 for the purposes of deriving the acoustic transmittance.

In the proposed metamaterial, given its inherent transverse nature, both pressure and velocity field at the boundaries of the metamaterial will be a function of *r*. Hence, as the first step to derive the transmittance, the following definitions of acoustic pressure and velocity field at the interfaces (*x = 0* and *x = t)* are employed to relieve the transverse variation of the pressure and velocity fields (r-dependancy).

$$\overline{P_1}(x=0) = \frac{2\pi}{\pi r_1^2}\int_0^{r_1} p(r,x)\big|_{x=0}\, rdr \tag{4.1}$$

$$\overline{P_2}(x=0) = \frac{2\pi}{\pi (r_2^2 - r_1^2)}\int_{r_1}^{r_2} p(r,x)\big|_{x=0}\, rdr \tag{4.2}$$

$$\overline{P_1}(x=t) = \frac{2\pi}{\pi r_1^2}\int_0^{r_1} p(r,x)\big|_{x=t}\, rdr \tag{4.3}$$

$$\overline{P_2}(x=t) = \frac{2\pi}{\pi (r_2^2 - r_1^2)}\int_{r_1}^{r_2} p(r,x)\big|_{x=t}\, rdr \tag{4.4}$$

$$\overline{U_1}(x=0) = 2\pi \int_0^{r_1} u(r,x)\big|_{x=0}\, rdr \tag{4.5}$$

$$\overline{U_2}(x=0) = 2\pi \int_{r_1}^{r_2} u(r,x)\big|_{x=0}\, rdr \tag{4.6}$$

$$\overline{U_1}(x=t) = 2\pi \int_0^{r_1} u(r,x)\big|_{x=t}\, rdr \tag{4.7}$$

$$\overline{U_2}(x=t) = 2\pi \int_{r_1}^{r_2} u(r,x)\big|_{x=t}\, rdr \tag{4.8}$$

In which *p* and *u* are acoustic pressure and the velocity field, respectively. $\overline{P}_{1\&2}$ and $\overline{U}_{1\&2}$ are averaged pressure and volume velocity at the region 1 and region 2 interfaces with the medium inside the waveguide.

Next, considering that the regions are separated with a hard boundary, the propagation of the acoustic wave within each region may be considered independently. Consequently, the transfer matrices relating the output pressure and velocity to the input conditions for regions 1 and 2 may be written in a decoupled fashion. Considering the case of plane wave propagation, the transfer matrices of these regions may be derived as follows: Acoustic pressure and velocity in these regions following the $-i\omega t$ convention may be written as:

$$\overline{P_m}(x) = A_1 e^{ik_0 n_m x} + A_2 e^{-ik_0 n_m x} \tag{4.9}$$

$$\overline{U_m}(x) = \frac{A_1 e^{ik_0 n_m x}}{Z_m} - \frac{A_2 e^{-ik_0 n_m x}}{Z_m} \tag{4.10}$$

In which k_0 is the wave number associated with the medium within the duct, defined as $k_0 = \omega / c_0$, n_m and Z_m are the effective refractive index and the effective acoustic

impedance of the region *m*, respectively, and t is the thickness of the metamaterial shown in **Figure 4.1**. A_1 and A_2 are constant coefficients associated with the outgoing and incoming wave, respectively. Employing Equations (4.9) and (4.10), the averaged pressure and volume velocity at $x = 0$ and $x = t$ may be derived as:

$$\overline{P_m}(x=0) = A_1 + A_2 \tag{4.11}$$

$$\overline{U_m}(x=0) = \frac{A_1}{Z_m} - \frac{A_2}{Z_m} \tag{4.12}$$

$$\overline{P_m}(x=t) = A_1 e^{ik_0 n_m t} + A_2 e^{-ik_0 n_m t} \tag{4.13}$$

$$\overline{U_m}(x=t) = \frac{A_1 e^{ik_0 n_m t}}{Z_m} - \frac{A_2 e^{-ik_0 n_m t}}{Z_m} \tag{4.14}$$

By first deriving A_1 and A_2 in terms of the $\overline{P_m}(x=0)$ and $\overline{U_m}(x=0)$ using the Equations (4.11) and (4.12) and then substituting them into the Equations (4.13) and (4.14), one may find the transfer matrices for regions 1 and 2 ($m = 1, 2$) as:

$$\begin{bmatrix} \overline{P_1}(x=0) \\ \overline{U_1}(x=0) \end{bmatrix} = \begin{bmatrix} \cos(k_0 n_1 t) & -iZ_1 \sin(k_0 n_1 t) \\ -\frac{i}{Z_1}\sin(k_0 n_1 t) & \cos(k_0 n_1 t) \end{bmatrix} \begin{bmatrix} \overline{P_1}(x=t) \\ \overline{U_1}(x=t) \end{bmatrix} \tag{4.15}$$

$$\begin{bmatrix} \overline{P_2}(x=0) \\ \overline{U_2}(x=0) \end{bmatrix} = \begin{bmatrix} \cos(k_0 n_2 t) & -iZ_2 \sin(k_0 n_2 t) \\ -\frac{i}{Z_1}\sin(k_0 n_2 t) & \cos(k_0 n_2 t) \end{bmatrix} \begin{bmatrix} \overline{P_2}(x=t) \\ \overline{U_2}(x=t) \end{bmatrix} \tag{4.16}$$

To this end, the relation between the input pressure and velocity to the output condition within each region of the metamaterial has been derived in terms of the transfer matrices.

The next step in deriving the transmittance (defined as the ratio of transmitted power to the incidence power) is to investigate the interaction between the acoustic wave inside the duct and the transverse bilayer metamaterial's interfaces at $x = 0$ and $x = t$. In order to investigate this interaction, a Green's function method is utilized herein, which describes the response of the system to a point source. Utilizing Green's function and given the fact that any source distribution may be written as an integral of the point sources, one may readily derive the resultant acoustic field.

Green's function $G(r, x; r_0, x_0)$ within a semi-infinite circular duct terminating at $x = 0$ may be derived as the solution of the Helmholtz equation (Feng et al., 2013):

$$\nabla^2 G(r, x; r_0, x_0) + k_0^2 G(r, x; r_0, x_0) = -\frac{\delta(r - r_0)\delta(x - x_0)}{2\pi r} \tag{4.17}$$

Where δ represents the Dirac delta function. From the solution of the Equation (4.17), Green's function with respect to the incident and transmitted side of the metamaterial can be obtained as (Li et al., 2014):

$$x \le 0 : G_1(r, x; r_0, x_0) = \sum_{n=0}^{n=\infty} \frac{\varphi_n(r_0)\varphi_n(r)}{-2i\pi r_2^2 \sqrt{k_0^2 - k_n^2}} \left(e^{i\sqrt{k_0^2 - k_n^2}|x - x_0|} + e^{i\sqrt{k_0^2 - k_n^2}|x + x_0|}\right) \tag{4.18}$$

$$x \ge t : G_2(r, x; r_0, x_0) = \sum_{n=0}^{n=\infty} \frac{\varphi_n(r_0)\varphi_n(r)}{-2i\pi r_2^2 \sqrt{k_0^2 - k_n^2}} \left(e^{i\sqrt{k_0^2 - k_n^2}|x - x_0|} + e^{i\sqrt{k_0^2 - k_n^2}|x + x_0 - 2t|}\right) \tag{4.19}$$

When r_2 and t are duct radius and metamaterial's thickness, respectively, as shown in **Figure 4.1**, and the eigenmode is defined as $\varphi_n(r) = J_0(k_n r) / J_0(k_n r_2)$ with the wavenumber k_n as the solution of $J'(k_n r_2) = 0$ where J represents the Bessel function.

Utilizing Kirchhoff–Helmholtz integral, the pressure field on the left side of the metamaterial ($x \le 0$) may be written as (Feng et al., 2013) :

$$p(r,x) = e^{ik_0 x} + e^{-ik_0 x}$$
$$+2\pi\int_0^{r_1} G_1(r,x;r_0,x_0)\left.\frac{\partial p(r_0,x_0)}{\partial x_0}\right|_{x_0=0} r_0 dr_0 + 2\pi\int_{r_1}^{r_2} G_1(r,x;r_0,x_0)\left.\frac{\partial p(r_0,x_0)}{\partial x_0}\right|_{x_0=0} r_0 dr_0 \quad (4.20)$$

By applying the conservation of the momentum, one may write:

$$i\omega\rho_0 u(r,0) = -\left.\frac{\partial p(r_0,x_0)}{\partial x_0}\right|_{x_0=0} \quad (4.21)$$

By firstly rewriting the pressure gradient term in Equation (4.20) using Equation (4.21), and subsequently employing Equations (4.5) and (4.6), one may derive:

$$p(r,0) = 2$$
$$+2\pi i\omega\rho_0 \frac{\overline{U_1}(x=0)}{\pi r_1^2}\int_0^{r_1} G_1(r,0;r_0,0) r_0 dr_0 + 2\pi i\omega\rho_0 \frac{\overline{U_2}(x=0)}{\pi(r_2^2 - r_1^2)}\int_{r_1}^{r_2} G_1(r,0;r_0,0) r_0 dr_0 \quad (4.22)$$

By substituting the $p(r,0)$ found from Equation (4.22) into Equations (4.1) and (4.2), one may readily derive that:

$$\overline{P_1}(x=0) = 2$$
$$+\frac{4i\rho_0\omega\overline{U_1}(x=0)}{r_1^4}\int_0^{r_1}\int_0^{r_1} G_1(r,0;r_0,0) r_0 dr_0 r dr + \frac{4i\rho_0\omega\overline{U_2}(x=0)}{r_1^2(r_2^2 - r_1^2)}\int_0^{r_1}\int_{r_1}^{r_2} G_1(r,0;r_0,0) r_0 dr_0 r dr \quad (4.23)$$

$$\overline{P_2}(x=0) = 2$$
$$+\frac{4i\rho_0\omega\overline{U_1}(x=0)}{r_1^2(r_2^2 - r_1^2)}\int_{r_1}^{r_2}\int_0^{r_1} G_1(r,0;r_0,0) r_0 dr_0 r dr + \frac{4i\rho_0\omega\overline{U_2}(x=0)}{(r_2^2 - r_1^2)^2}\int_{r_1}^{r_2}\int_{r_1}^{r_2} G_1(r,0;r_0,0) r_0 dr_0 r dr \quad (4.24)$$

Similarly, when $x \geq t$, following the same procedure and employing the Green's function $G_2(r, x; r_0, x_0)$, the pressure may be derived as:

$$\overline{P_1}(x=t) = -\frac{4i\rho_0\omega\overline{U_1}(x=t)}{r_1^4}\int_0^{r_1}\int_0^{r_1} G_2(r,t;r_0,t)r_0 dr_0 r dr - \frac{4i\rho_0\omega\overline{U_2}(x=t)}{r_1^2(r_2^2-r_1^2)}\int_0^{r_1}\int_{r_1}^{r_2} G_2(r,t;r_0,t)r_0 dr_0 r dr \quad (4.25)$$

$$\overline{P_2}(x=t) = -\frac{4i\rho_0\omega\overline{U_1}(x=t)}{r_1^2(r_2^2-r_1^2)}\int_{r_1}^{r_2}\int_0^{r_1} G_2(r,t;r_0,t)r_0 dr_0 r dr - \frac{4i\rho_0\omega\overline{U_2}(x=t)}{(r_2^2-r_1^2)^2}\int_{r_1}^{r_2}\int_{r_1}^{r_2} G_2(r,t;r_0,t)r_0 dr_0 r dr \quad (4.26)$$

The resultant Equations (4.23, 4.24, 4.25, and 4.26), in addition to the tensor Equations (4.15) and (4.16), provide a solvable system of 8 equations from which averaged pressure and velocity terms defined in equations (4.1) to (4.8), as 8 variables, may readily be calculated. Please note that in the calculation of the numerical integrals present in Equations (4.23) to (4.26), a sufficient number of the summation (*n* in equations (4.18) and (4.19)) needs to be considered in order to yield accurate results. Herein, a sufficient number of summations has been considered to ensure that the relative difference between the resultant partial summation and the exact summation value does not exceed 1%.

Followed by the derivation of the averaged pressure and velocity discussed herein, the overall pressure and velocity field on the two sides of the transverse bilayer metamaterial may be written as:

$$P(x=0) = \frac{1}{\pi r_2^2}[\pi r_1^2 \overline{P_1}(x=0) + \pi(r_2^2 - r_1^2)\overline{P_2}(x=0)] \quad (4.27)$$

$$P(x=t)=\frac{1}{\pi r_2^2}[\pi r_1^2\overline{P_1}(x=t)+\pi(r_2^2-r_1^2)\overline{P_2}(x=t)] \tag{4.28}$$

$$u(x=0)=\frac{1}{\pi r_2^2}[\overline{U_1}(x=0)+\overline{U_2}(x=0)] \tag{4.29}$$

$$u(x=t)=\frac{1}{\pi r_2^2}[\overline{U_1}(x=t)+\overline{U_2}(x=t)] \tag{4.30}$$

Eventually, utilizing Equations (4.27) to (4.30), the transfer matrix corresponding to the transverse bilayer metamaterial may be constructed as follows:

$$\begin{bmatrix} P(x=0) \\ u(x=0) \end{bmatrix}=\begin{bmatrix} M_{11} & M_{12} \\ M_{21} & M_{22} \end{bmatrix}\begin{bmatrix} P(x=t) \\ u(x=t) \end{bmatrix} \tag{4.31}$$

From which the transmittance may be readily calculated as:

$$T=\left|\frac{2}{M_{11}+M_{12}/\rho_0 c_0+M_{21}\rho_0 c_0+M_{22}}\right|^2 \tag{4.32}$$

Using this approach, the transmittance from the bilayer metamaterial for different values of refractive index and acoustic impedance is derived and shown in **Figure 4.2(a)** and **Figure 4.2(b)**. In **Figure 4. 2(a)**, it is considered that $n_2/n_1=10$ and the transmittance is depicted as a function of the non-dimensional quantity n_2t/λ (λ denotes the wavelength) for four different values of the impedance ratio. In **Figure 4. 2(b)**, the impedance ratio has been kept constant $(Z_2/Z_1=10)$, and the transmittance is depicted for three different values of the refractive index ratio. Notably, the background medium within the waveguide is considered to be air, and it is assumed that the medium in region 1 is identical to the background medium. Hence, the acoustic impedance of region 1 may

be derived as $Z_1 = \rho_0 c_0 / \pi r_1^2$, and the refractive index (n_1) is equal to unity. From the resulted transmittance curve, it may be observed that for different values of Z_2 and n_2, given the differing acoustic properties of regions 1 and 2, an asymmetric transmission profile is obtained in which destructive interference may result in zero transmittance due to Fano-like interference. The destructive interference emerges where $n_2 t = \lambda / 2$, which is the resonating state of region 2. Given the contrast in refractive indices of the two regions, region 1 remains in a continuum state and, consequently, a Fano-like interference occurs. During this state, the portion of the acoustic wave traveling through region 2 interacts with resonance-induced localized modes in this region, resulting in an out-of-phase condition after traveling through region 2.

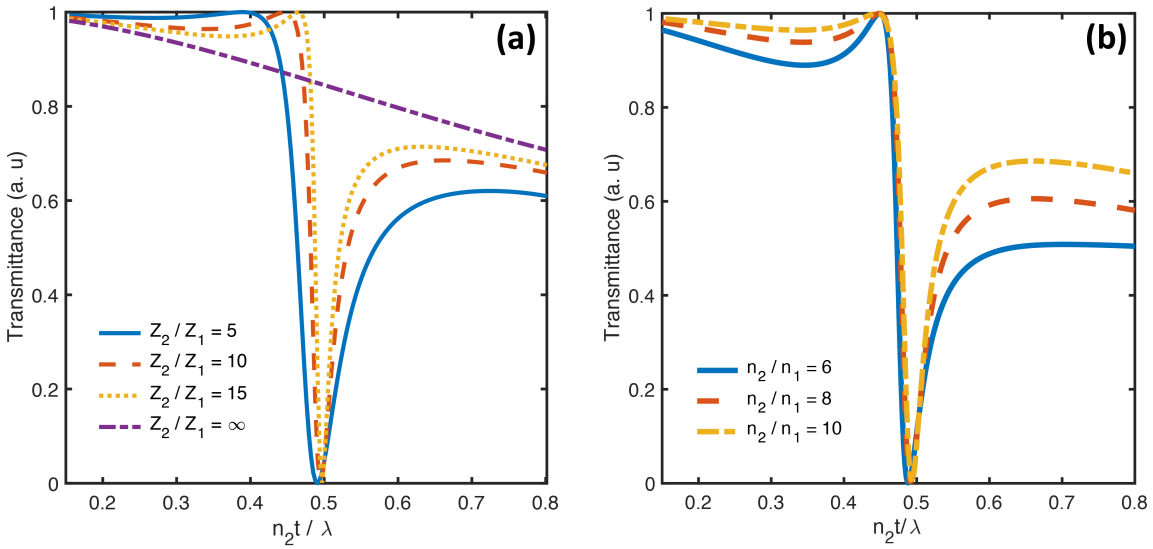

Figure 4.2. Analytical results. (a) Acoustic transmittance through the transverse bilayer metamaterial for different values of acoustic impedance contrast when the refractive indices ratio is kept constant. Notably, for the cases with a finite ratio between the impedance of the regions (shown with the blue line, orange dashed line, and the yellow dotted line), Fano-like interference results in destructive interference. However, in the case of infinite contrast between the regions impedance, representing orifice-like behavior, the destructive interference is suppressed (purple dotted-dashed line). (b) Acoustic transmittance through the bilayer metamaterial for different ratios of the refractive indices when the acoustic impedance is kept constant.

The portion of the incident acoustic wave traveling through region 1 will pass the metamaterial with negligible phase shift and, consequently, a resultant destructive interference occurs on the transmission side of the metamaterial. By comparing the transmittance for different values of the impedance ratio, it may be inferred that by increasing the contrast between the acoustic impedances of the two regions, the quality factor (Q-factor) of the attenuation performance is increased. This attribute provides a degree of freedom through which, by adjusting the impedance contrast, the proper filtration bandwidth may be realized. Notably, when the acoustic impedance ratio yields a very large number $(Z_2 / Z_1 = \infty)$, the filtration performance is suppressed, given its marked narrowband character, and an orifice-like behavior is realized. However, an orifice structure with a similar open area geometry results in a relatively poor sound filtration performance, leading to only minor degrees of attenuation of the transmitted acoustic wave. **Figure 4. 2(b)**, demonstrates the effect of refractive index contrast between the two media on transmittance and illustrates that high degrees of filtration is obtained when $n_2 t = \lambda / 2$. Thusly, by adjusting the refractive indices in the proposed structure, high-performance sound attenuation may be realized at any desired frequency.

Of note, the destructive interference initially occurs at $n_2 t = \lambda / 2$, which is the first resonance mode of region 2, but will also occur at higher resonance modes when $n_2 t = N\lambda / 2$ for integers of N shown in **Figure 4. 3(a)**. To this end, the silencing behavior of the transverse bilayer metamaterial has been investigated for the case of a normally incident acoustic plane wave. However, given the subwavelength nature of the proposed metamaterial structure, it is expected that silencing will also be present in the case of

oblique incidence. To validate this expectation, the full-wave simulation was utilized, and the transmittance through the transverse bilayer metamaterial in the case of oblique incidence with different incident angles was derived and shown in **Figure 4. 3(b)**. It can be observed that the silencing functionality of the proposed metamaterial structure is present even for very large angles of incidence.

The methodology presented herein and based on a Fano-like interference in a bilayer metamaterial structure offers a design platform to selectively silence the unwanted sound. Using this design, by tuning the acoustic impedance and refractive index contrast between the two regions of the metamaterial, the desired acoustic filtration performance may be achieved. In the following sections, this concept is utilized to design a metamaterial structure that features a large open area for air transport, while also selectively silencing the unwanted sound.

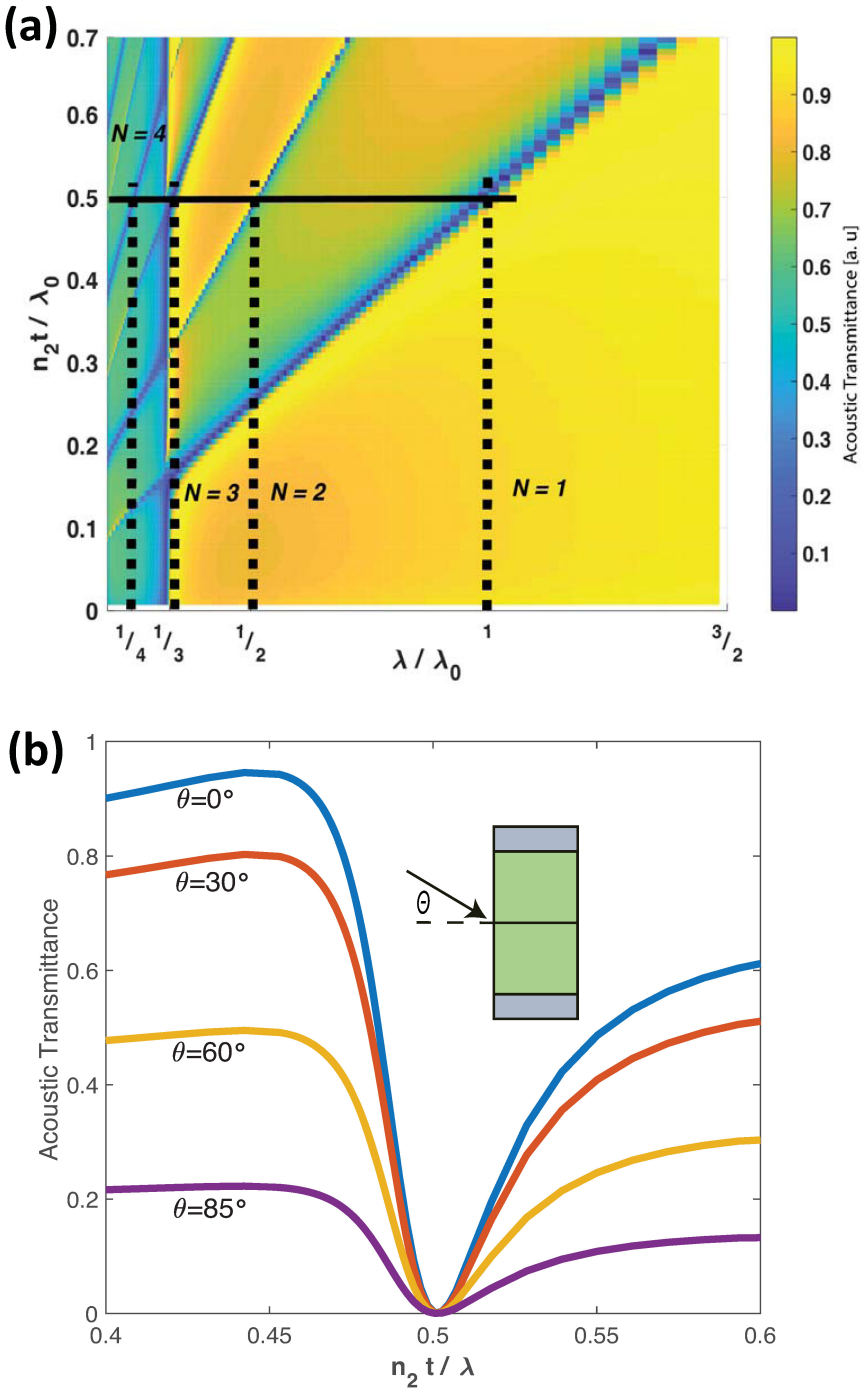

Figure 4.3. (a)Acoustic transmittance from transverse bilayer metamaterial structure with different refractive index ratios and a constant impedance ratio of 10. The silencing functionality initially emerges when $n_2 t$ is equal to half wavelength but is also present in higher order harmonics when it approximates integer multiplication of half wavelength. (b) Acoustic transmittance through transverse bilayer metamaterial in case of oblique incidence with different incident angles.

4.2 Ultra-Open Metamaterial for Selective Sound Silencing

In this section, an ultra-open metamaterial (UOM) structure based on the concept of the bilayer metamaterial is designed and its performance in sound silencing experimentally validated. The UOM structure is shown in **Figure 4. 4(a)**, the effective acoustic model of which may be simplified to the form of the transverse bilayer metamaterial structure. The center portion of the designed structure ($r < r_1$) is completely open area which yields a high degree of air transport. This region corresponds to region 1 in the bilayer metamaterial structure, and its characteristic acoustic impedance may be derived as $\rho_0 c_0 / \pi r_1^2$, where ρ_0 and c_0 are the density and sound speed of the background medium, respectively. Notably, the acoustic refractive index of this region is equal to unity. As discussed above, in order to obtain the desired silencing functionality, a contrast in the acoustic properties of the two regions is essential. The difference in acoustic properties of the two regions may provide the resonating state condition in region 2 while region 1 remains in the continuum state. Therefore, in order to realize the contrast in the acoustic properties of the two regions, the concept of a helical metamaterial structure is utilized. Helical metamaterials are founded on the basis of space-coiling metamaterials in which the acoustic wave pathway represents the form of a helix. In these structures, by tailoring the geometrical parameters, the desired effective refractive index and effective acoustic impedance may be obtained, and their application in wavefront manipulation has been demonstrated (Zhu et al., 2016; Esfahlani et al., 2017).

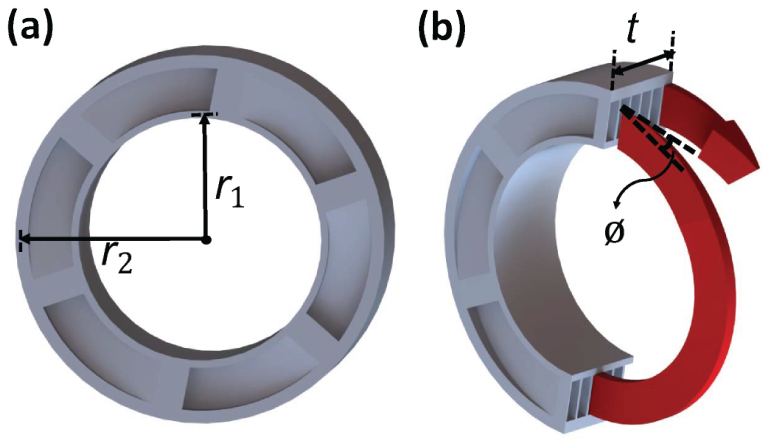

Figure 4.4. (a) UOM structure is shown in which the open region at the center ($r < r_1$) corresponds to region 1 in the transverse bilayer metamaterial and the outer region, featuring six channels coiled in the form of helix ($r_1 < r < r_2$), corresponds to region 2. (b) Internal structure of the UOM is shown with an acoustic wave traveling through the channels and essentially following the helical pathway with a helix angle of ϕ.

In the helical metamaterial regime ($r_1 < r < r_2$), which corresponds to region 2 in the transverse bilayer metamaterial, six air channels are coiled in the form of a helix in which the extended path length of the acoustic wave provides a large effective refractive index in this region. Moreover, the small cross-sectional area of the helix channels in comparison to the waveguide yields a large acoustic impedance in this region. The internal features of the UOM are shown in **Figure 4. 4(b)** in which the red arrow illustrates the pathway through the helical channels.

The acoustic impedance of the helical region may be approximated as $\rho_0 c_0 / t(r_2 - r_1)$ in which t, r_1 and r_2 are structure thickness, inner radius, and outer radius, respectively, and which are shown in **Figure 4.4(a)**. The contrast or ratio between the acoustic impedances of the two regions may be expressed as:

$$Z_2 / Z_1 = \pi r_1^2 / t(r_2 - r_1) \tag{4.33}$$

Considering the effective path length of the acoustic wave traveling through the helical channels, the effective refractive index of the helical region may be approximated as:

$$n_2 = 1/\sin(\phi) \tag{4.34}$$

Where ϕ denotes the helix angle shown in **Figure 4.4(b)**. From Equation (4.33) and Equation (4.34), it can be inferred that by adjusting the helix angle (ϕ), the desired refractive index, and the values of the t, r_1 and r_2 parameters, the desired impedance ratio may be realized. Noteworthy, the presented design offers several highly valuable degrees of freedom to optimize device performance and tailor applicability. The refractive index, as it is expressed in Equation (4.34), depends solely on the helix angle, which may be independently tailored without any effect on other design parameters. In addition, the acoustic impedance ratio derived in Equation (4.33) is a function of three geometrical parameters for which there exist infinite sets of values leading to any desired relative impedance value. Therefore, based on design preference, such as a preference for thinning the structure (small value of *t*) or increasing the open area of the structure (increasing r_1 / r_2), an optimal metamaterial unit cell structure may be readily designed.

Finally, in order to experimentally validate the performance of the UOM structure, a UOM has been designed with the aim of silencing sound with a frequency near 460 Hz and, therefore, was fabricated with dimensions of $t = 5.2cm$, $r_1 = 5.1cm$, $r_2 = 7cm$ and $\phi = 8.2\deg$. The UOM was fabricated using a commercial 3D printer (Dimension SST 1200es) from ABS plastic with a resolution of 0.2 mm. Next, the fabricated UOM was post-processed using a two-part epoxy resin (BJB Enterprise TC-1614 A/B) that sealed the

internal, porous nature of the 3D printed UOM, thereby providing improved mechanical properties. Please note that the overall size of the fabricated UOM herein is deep subwavelength in nature and, for instance, the UOM's thickness approximates 0.07λ while λ at 460 Hz approximates 74.5 cm. Employing Equation (4.33) and (4.34), the UOM may be simply modeled as a transverse bilayer metamaterial with an acoustic impedance ratio of $Z_2 / Z_1 = 7.5$ and refractive index ratio of $n_2 / n_1 = 7$, approximated based on the fabricated UOM dimensions.

Please note that the assumption with regards to the presence of an acoustically rigid spacer utilized in the analysis of the case of transverse bilayer metamaterial is also relevant for the proposed UOM silencer. The two regions of the fabricated UOM structure are separated with an acrylonitrile butadiene styrene (ABS) plastic layer of 6mm that results in approximately 29 dB transmission loss at 450 Hz for the wave traveling from the open region of the UOM to the helical metamaterial region and vice versa. Based on this large transmission loss expected from this layer, the interface between the two regions may be reasonably approximated as a rigid spacer layer such as was assumed in the transverse bilayer metamaterial structure. Consequently, the equivalent model of the presented UOM structure may be simplified to the form of the transverse bilayer metamaterial discussed in the previous section.

The fabricated UOM structure was experimentally tested using an air-filled impedance tube, with the transmittance derived in the frequency range of 300-600Hz. The impedance tube setup was designed and fabricated in accordance with the ASTM E 2611-09 standard. The setup featured a speaker enclosed in a soundproof box that predominately

guided the acoustic wave towards the impedance tube and eliminated the effect of back reflections from the experimental environment. The impedance tube was composed of two schedule-40 PVC tubes with nominal diameters of 15.24 cm and a length of 1.5m that were placed on either side of the UOM structure. In order to obtain the transmittance through the UOM, the transfer matrix of the UOM was retrieved for two different types of terminations, and by sweeping the loudspeaker's input frequency, the transmittance was obtained across the frequency range of 300Hz-600Hz. Noteworthy, experimental transmittance herein has been obtained by employing the two-load method in which open-end and semi-anechoic terminations were utilized. The detail of derivation using the impedance tube is discussed in Appendix E.

The experimental result is shown in **Figure 4.5** in which the transmittance (leftward y-axis) is shown with a dotted line with a triangular marker and its representation in sound transmission loss (STL) defined as $-10\log(\tau)$ (where τ is transmittance) is shown with the dashed line. Additionally, based on the transverse bilayer metamaterial model and using the effective acoustic properties estimated for the fabricated UOM, transmittance has been derived analytically and is also shown in **Figure 4.5** (solid line). As demonstrated in **Figure 4.5**, the experimentally measured transmittance through the UOM structure exhibits an asymmetric profile possessing a dip region where destructive interference due to Fano-like interference has silenced the transmitted wave. Notably, the experimental results obtained herein are in agreement with the predicted analytical solution and, consequently, the applicability of the analytical model for the design of this class of metamaterial structures is validated.

Based on the obtained experimental results, the transmitted acoustic energy is decreased to approximately 6% at the peak frequency, indicating that approximately 94% of the acoustic wave energy is blocked using the proposed structure. Moreover, there exists a high degree of agreement between the peak filtration frequency band when comparing the analytical and experimental results and the fact that that the experimentally obtained peak frequency is in close proximity to the regime where $n_2 t = \lambda / 2$ is confirmed. Due to limitations in the fabrication precision of the metamaterial structure, the targeted frequency in the UOM design step has been selected to approximate 460Hz, though device performance may readily be realized at lower frequencies by decreasing the helix angle.

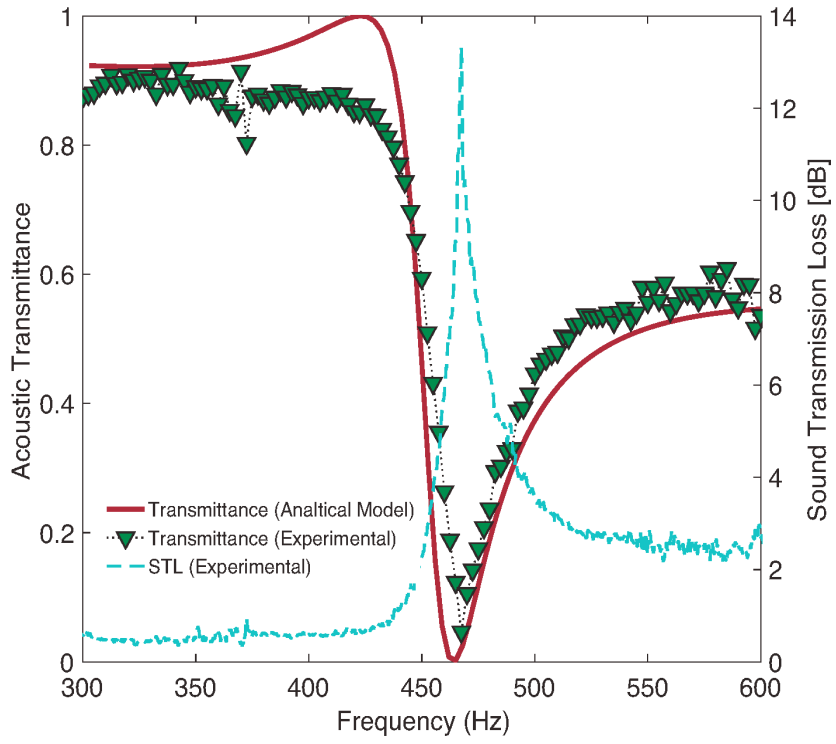

Figure 4.5. Acoustic transmittance resulting from the impedance tube experiment is shown with the dotted-line with a triangular marker demonstrating that near 460 Hz, the transmittance is reduced to the minimum value of approximately 0.06. Sound transmission loss (STL) for the wave passing through the UOM is also shown with the dashed line corresponding the rightward y-axis. The solid line represents the predicted behavior using Green's function method by modeling the UOM structure as a transverse bilayer metamaterial.

In order to visualize the silencing performance of the UOM structure and gain a deeper insight into its performance, the sound transmission through the UOM is modeled numerically using COMSOL finite element software. Given the complexity associated with the helical shape of the UOM's channel, the acoustic transmission has been modeled in three dimensional (3D) space but a cut-plane is used to demonstrate the resultant acoustic pressure and acoustic velocity fields in two dimensions (2D), shown in **Figure 4.6(a)** and **Figure 4.6(b)**. The background color represents the absolute value of the pressure field normalized by the amplitude of the incident wave, and the white lines reflect the stream and orientation of the local acoustic velocity field. Demonstrated in **Figure 4.6(a)** is a plane wave with a frequency of 400 Hz incident on the metamaterial from the left side, as shown with black arrows. In accordance with the analytically and experimentally expected behavior of the UOM structure, in the frequency regime of 400 Hz, high-pressure transmission results.

At this state, given the fact that the helical portion of the UOM structure possesses a markedly larger acoustic impedance in comparison with the open portion in the center, the incident wave will predominately travel through the central, open portion of the UOM. This behavior may be visually confirmed with the local velocity field stream shown in **Figure 4.6(a)**, where both preceding and beyond the UOM structure, the velocity field exhibits minimal disturbance save for the change in cross-sectional area. In **Figure 4.6(b)**, a similar case of a plane wave incident from the left side is demonstrated, but with a frequency of 460 Hz. Based on the theoretical and experimental results obtained above, it is expected that at this frequency, the wave transmitted through the helical portion of the

UOM will become out of phase with the transmitted wave traveling through the central, open portion of the metamaterial. The results obtained herein confirm this expectation, demonstrating that the destructive interference on the transmission side (right side) of the UOM has resulted in effectively eliminating wave transmission.

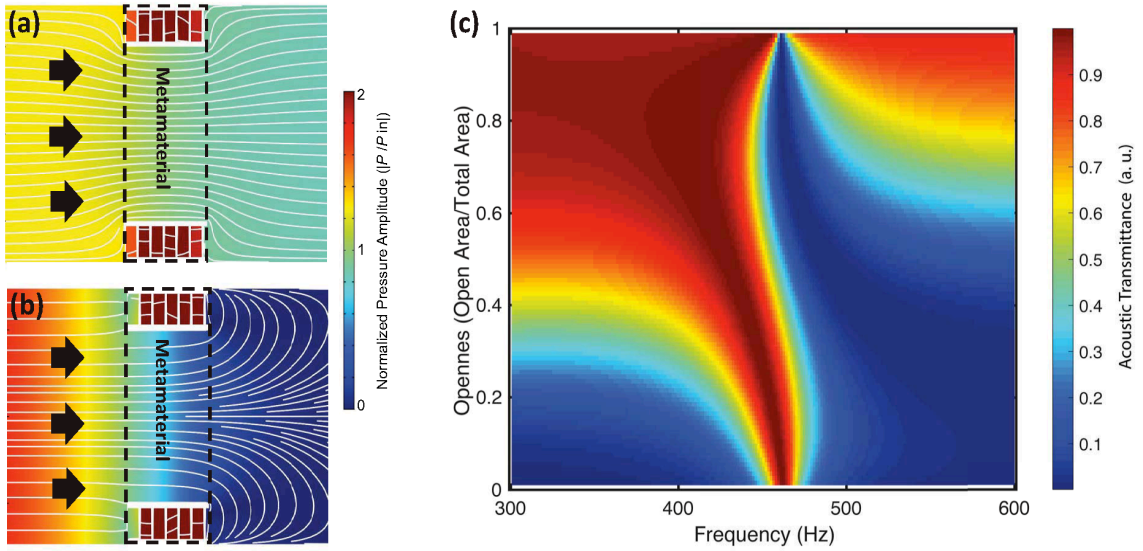

Figure 4.6. (a) The absolute pressure value normalized by the incident wave magnitude resulting from a plane wave with a frequency of 400 Hz and an incident on the UOM from the left-hand side is shown using a color map. The local velocity stream is shown with the white lines. At this frequency, the transmission coefficient is about 0.85, hence, approximately 72% of the acoustic wave energy is transmitted. (b) The pressure and velocity profile are depicted with an incident plane wave of the same amplitude but a frequency of 460 Hz. At this frequency, due to Fano-like interference, the transmitted wave has a markedly decreased amplitude, and the wave has been silenced. In this case, the phase difference between the transmitted waves from the two regions of the metamaterial has resulted in a curvature of the wave velocity field and has diminished the far-field radiation. (c) Acoustic transmittance through UOM structures with different degrees of structure openness. Transmittance has been analytically derived using Green's function method. Notably, UOM structures considered herein feature identical refractive index ratios in their transverse bilayer metamaterial model but have different impedance ratios.

Notably, the out of phase transmission through the two regions of the UOM may be further validated using the velocity profile shown in **Figure 4.6(b)** with white lines. It may be readily observed that the local acoustic velocities of the transmitted wave from the two regions of the UOM are in out-phase-condition, resulting in marked curvature of the

velocity stream and diminished far-field radiation. It should be mentioned that with the presence of the destructive interference due to Fano-like interference, the metamaterial structure mimics the case of pressure-release termination in which near-zero effective acoustic impedance results in a predominant reflection of the incident wave with Pi phase shift.

The UOM structure experimentally validated herein features a nearly 60% open area, which yields the capacity for both efficient ventilation in combination with high-performance selective sound silencing. Importantly, the presented methodology based on the transverse bilayer metamaterial concept and employed to design the UOM structure does not impose any inherent limitation on the area fraction of the central, open region. As shown in **Figure 4.2 (a)**, with an increase in the ratio between the acoustic impedance of two regions, silencing functionality will be achieved, although in a narrower band of frequency. Considering the fact that openness percentage, may be very well correlated with the acoustic impedance ratio, it is expected that even with very high openness percentage, silencing can be realized within the scope of the presented methodology. This assumption has been validated by analytically retrieving the acoustic transmittance through the UOM structure with different openness values, shown in **Figure 4.6(c)**. It may be observed that even for UOM structures with a very high percentage of open area (approaching a nearly complete open area where openness approximates 1), the silencing functionality remains present with a resulting decrease in the silenced frequency bandwidth.

Notably, in the present work, the structural elements of the proposed UOM have been considered acoustically rigid in both analytical and numerical approaches. The

rigidity assumption employed herein is supported by the fact that the ABS layers of the fabricated UOM structures result in a transmission loss in the targeted frequency range of a magnitude such that these layers may be safely considered as rigid. However, when targeting the silencing the very low frequency or when the UOM is employed as a building block of a larger element, such as a silencer wall, the incident acoustic wave may couple with the structural Eignemodes and different trend of behavior may be obtained. Therefore, in this cases, the acoustic-structure interaction needs to be considered and may not simply be omitted.

In this Chapter of the thesis, a metamaterial-based design methodology for air-permeable sound silencing is introduced. Firstly, inspired by the Fano-like interference phenomena, a transverse bilayer metamaterial concept is proposed from which destructive interference may be employed for acoustic silencing. Next, a UOM structure was designed accordingly and experimentally validated. The designed metamaterial possesses two distinguishable regions, the central, open portion, and the peripheral, helical portion, with a contrast in their acoustic properties. The central, open portion of the metamaterial provides a large degree of open area for air transport. Importantly, the design of the proposed metamaterial is inherently flexible, as discussed above. Therefore, based on the required degree of ventilation for a particular application, the open, central of the UOM metamaterial may readily be expanded to meet any ventilation requirement while maintaining acoustic wave silencing functionality.

The metamaterial-based methodology for the design of an air-permeable acoustic silencer presented herein provides an effective and versatile tool for the design of next-

generation acoustic silencing devices. Utilizing this method, sub-wavelength and lightweight structures featuring high degrees of open area may be designed to silence specific frequency bands of unwanted sound, along with their higher modes.

CHAPTER 5 LOCALLY RESONANT ACOUSTIC METAMATERIAL: PROPOSED APPLICATIONS IN NDE AND MEDICAL ULTRASOUND

For a wave of any kind traveling from one medium to another, the differences in the properties of the media determine whether the wave is reflected or transmitted. In the case of acoustic waves, the wave behavior at the interface between two media is dominated by the characteristic acoustic impedance. The characteristic acoustic impedance (Z) as an inherent property of the material, is defined as $Z = \rho c$ for an acoustical fluid and is solely a function of sound speed and density. When there exists a significant acoustic impedance mismatch between two media, the acoustic wave will be dominantly reflected at the interface, and when there exists an unremarkable mismatch, the dominant transmission will occur. Therefore, for instance, when designing a barrier to block the airborne sound, it is critical to design the barrier out of material with sufficiently distinct acoustic impedance with respect to air's impedance to effectively mitigate the transmission.

Moreover, ultrasound Non-Destructive evaluation (NDE) to locate the discontinuity within the material is only effective when the impedance of the inclusion is sufficiently distinct from the host material. Otherwise, for a discontinuity with unremarkable impedance mismatch, NDE performance is precluded given the reflection as a core element of NDE will be negligible. This fundamental aspect of wave behavior has set forth numerous limitation. For instance, in the case of medical ultrasound, currently, ultrasound-based imaging and treatment through the skull are significantly limited due to the large reflection of the ultrasound wave from the skull layer. Similarly, in the case of NDE, there exists a significant challenge for cement health monitoring in a borehole

environment due to the unremarkable impedance mismatch between borehole fluid and cement. This issue has essentially precluded the functionality of the detection methods such as pulse-echo in a downhole environment, especially in the case of low-density cement.

The Chapter herein seeks to propose a potential metamaterial-based solution to address the issue discussed here. Particularly, in this Chapter, it is proposed to leverage a locally resonant class of acoustic metamaterials (LRAM) in order to address those issue. In the class of LRAM, despite the conventional acoustic material in which impedance is relatively constant and determined by constitutive material properties, significant variation in the effective impedance emerges by approaching to the resonance state. The variation in the acoustic impedance may be very well correlated with the Fano-like interference phenomena in which the interaction between continuum and resonating states may lead to the large shift in the effective impedance of the medium (Ghaffarivardavagh et al., 2019). In this chapter, initially, the origin of the resonance induced impedance variation in the class of LRAM is analytically demonstrated. Subsequently, the potential implementation of the LRAM in two different applications is proposed.

5.1 Resonant Induced Impedance Variation in LRAM

Locally resonant acoustic metamaterial refers to the class of acoustic material in which the resonating element is integrated within a non-resonating host medium. The concept of locally resonant acoustic metamaterials (LRAM) has been the subject of growing scientific and technological interest in recent years due to their potential applications as low-frequency noise insulators (Mei et al., 2013), refractive lenses (He et al., 2008), and acoustic interferometers (Cervera et al., 2002). These composite materials exhibit spectral

gaps in a frequency range two orders of magnitude lower than those resulting from the Bragg scattering mechanism. The most common form of an LRAM is a composite material featuring resonating inclusions, such as spheres or bubbles, embedded within a continuum matrix material. The spherical inclusions in this type of metamaterial may have the simple form of single layer/material (**Figure 5.1(a)**) or possess more complicated shape such as the bilayer sphere or multilayer spheres (**Figure 5.1(b)**).

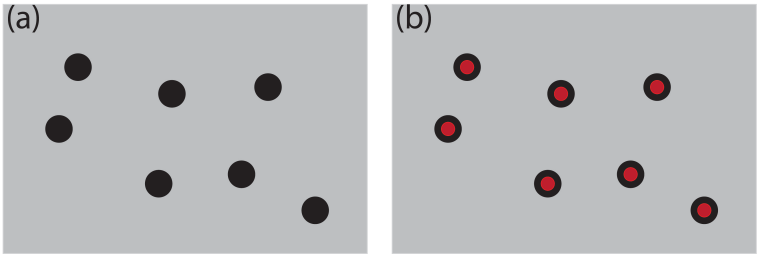

Figure 5.1. Locally resonant acoustic metamaterial with hard inclusion in a soft matrix. (a). single layer spherical inclusion. (b) Bilayer spherical inclusion

The effective acoustic properties of locally resonant acoustic metamaterial, in the low-frequency or so-called Rayleigh regime, may be very well approximated by volume averaging the acoustic properties of the soft and hard elements comprising the composite. However, for the frequencies near the resonance frequencies of the inclusions, the effective acoustic properties of the entire composite exhibits strong nonlinear behavior. Similar behavior may be found in the bubbly liquid in outside of the Wood's limit. The effective properties of the LRAM in the non-Rayleigh regime, such as the proximity of the inclusion's resonance, may be analytically studied in the framework of multiple scattering theory. Notably, for the simple shape of the scatters such as sphere or cylinder, the closed form equations may be obtained. Moreover, by neglecting the shear wave propagation in

the continuum matrix material, the equations may be significantly simplified by omitting the shear wave coupling at the interface of matrix/inclusion.

As a preliminary example, in order to investigate the acoustic behavior of LRAM in the non-Rayleigh regime, a simple case of metamaterial configuration is considered and studied. The metamaterial assumed herein, features single layer spherical inclusion with the radius of 1mm and density of 1500kg/m^3, with the longitudinal and shear sound speed of 3000m/s and 1000m/s respectively. The matrix material is considered herein with the density of 2400 kg/m^3 and with the sound speed of 4500m/s. It can be noted that, the matrix material is assumed to be an acoustical fluid which does not support the propagation of the shear wave. Finally, the volume ratio of the spherical inclusion in the continuum matrix is considered 8% and based on the work by Aristegui (Aristegui et al., 2006), the effective acoustic properties of the considered metamaterial, as an example of LRAM have been derived and shown in **Figure 5.2.**

From the results shown in **Figure 5.2**, it may be inferred that the overall acoustic properties of LRAM have mostly yielded to the weighted average (mixture law) of the inclusion and matrix acoustic properties (shown with dashed lines) except in the vicinity of two frequencies labeled by f_0 and f_1. The parameters shown in **Figure 5.2** are normalized with the associated values of the matrix material, and consequently, given the low volume ratio of the inclusions, it approximates the unity. From Figure **5.2(a)**, it may be observed that the effective stiffness of the considered LRAM is very close to the stiffness of the matrix material except near f_0.

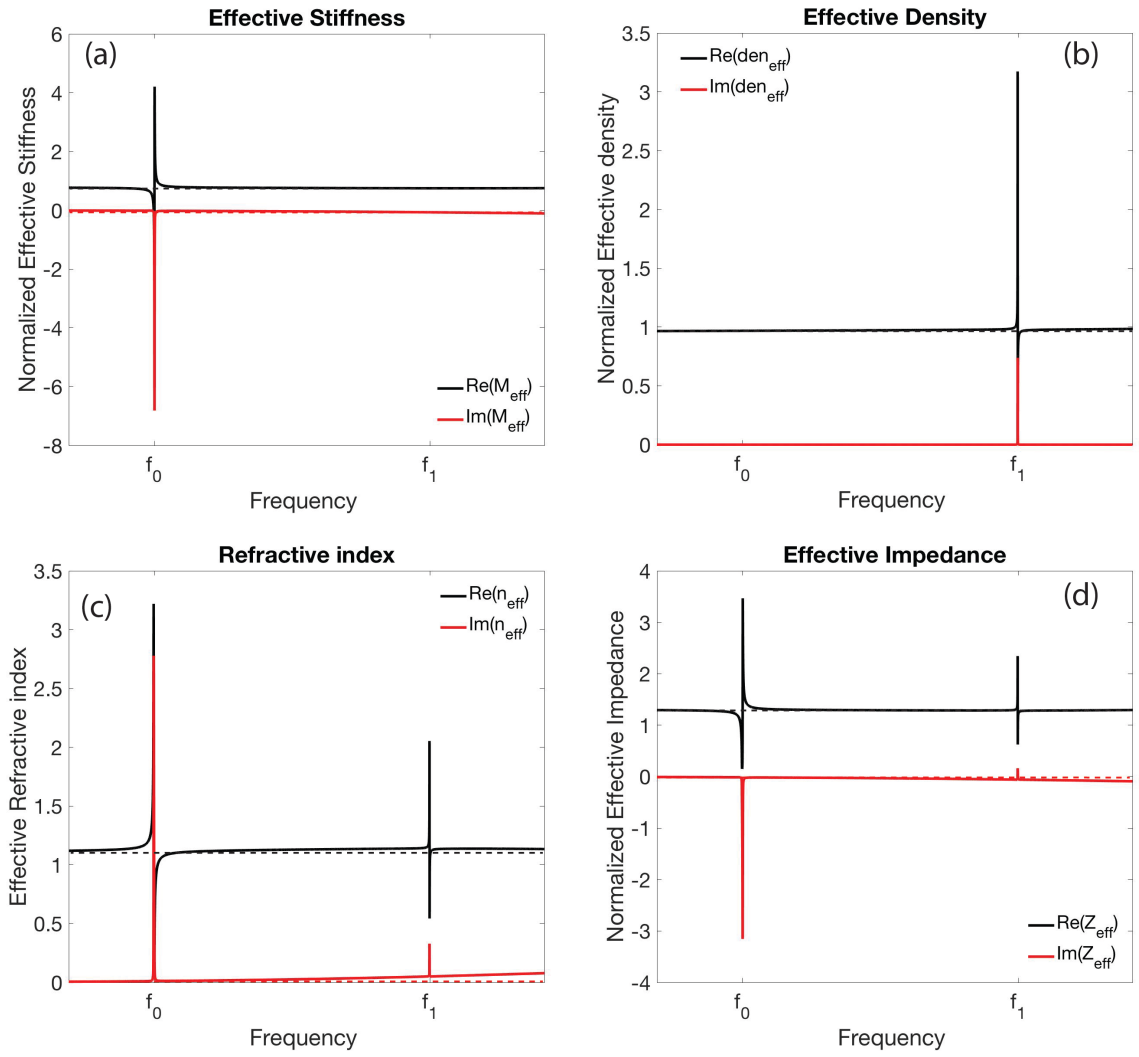

Figure 5.2. Effective acoustic properties of LRAM in the non-Rayleigh regime. (a) Normalized effective stiffness. (b)Normalized effective density. (c) Effective refractive index. (d)Normalized effective acoustic impedance. Normalized quantities have been normalized by the value of the matrix medium. f_0 denotes the first resonance mode of the inclusion (monopole), and f_1 is the second mode of the resonance of the inclusion (dipole).

In the vicinity of the f_0 which corresponds to the monopole resonance of the spherical inclusions (Breathing mode), the real part of stiffness first reduced to the value of zero and subsequently increased to about four times (4x) of the matrix material's stiffness. Moreover, near the f_0 resonance, large imaginary component has emerged in the effective

stiffness of LRAM. Similarly, in case of the effective density shown in **Figure 5.2 (b)**, its magnitude approximates the value of the matrix material except in the vicinity of the f_1 which is associated with the dipole resonance of the spherical inclusions.

The sudden change in the effective density and effective stiffness of the LRAM will yield to the variation in the effective acoustic impedance and wavenumber, as shown in **Figure 5.2 (c)** and **(d)**. The effective impedance of LRAM will approximate the effective impedance of the matrix material except in the vicinity of both monopole and dipole resonances in which its real part is found to vary between near zero magnitudes to about three times of the value of the matrix material in the LRAM configuration considered herein. Additionally, the imaginary part of the effective impedance (reactance) contains a spike in these regions, which corresponds to the phase shift in this material. This sudden variation of the impedance in the class of LRAM represents the foundation of the idea proposed in this chapter, and the potential application of such abnormal behavior will be discussed herein.

Prior to the discussion regards to utilization of this sudden impedance variation, it is critically important to consider the dispersive behavior of the LRAM in the vicinity of the resonances. From **Figure 5.2(d)** it may be observed that the effective wavenumber of LRAM, possesses a large imaginary component in the vicinity of the resonances that may lead to a significant attenuation in the propagating wave. In order to precisely investigate the disperse behavior of any particular LRAM, one needs to study its behavior comprehensively without imposing any simplifying assumptions. Thereby, the single unit cell of LRAM using COMSOL Multiphysics software is modeled, and its effective acoustic

impedance and wavenumber are retrieved and shown in **Figure 5.3** without omitting the shear wave coupling between the inclusion and matrix interfaces.

For our primary application, we considered LRAM featuring bilayer spherical particles with a hard-core (Steel: Young's Modulus= 117 GPa, Shear Modulus= 45 GPa and density of 9000kg/m^3) with the outer radius of 0.5mm and soft-shell (Silicon Rubber: Young's Modulus=20 MPa, Shear Modulus = 7 GPa and density of 1300kg/m^3) with the outer radius of 1mm. Moreover, it is considered herein that the bilayer spherical inclusions are embedded in the matrix material (Cement: Young's Modulus=30 MPa, Shear Modulus = 13 GPa and density of 2400kg/m^3) with the volume ratio of 4%. It should be noted that, bilayer configuration of the spherical inclusion is considered herein given the fact that in the case of single layer spheres, considering the limitation in the available material's properties, the radius of the spherical particle remains as the single design factor to tune the resonance of the sphere within the desired frequency range.

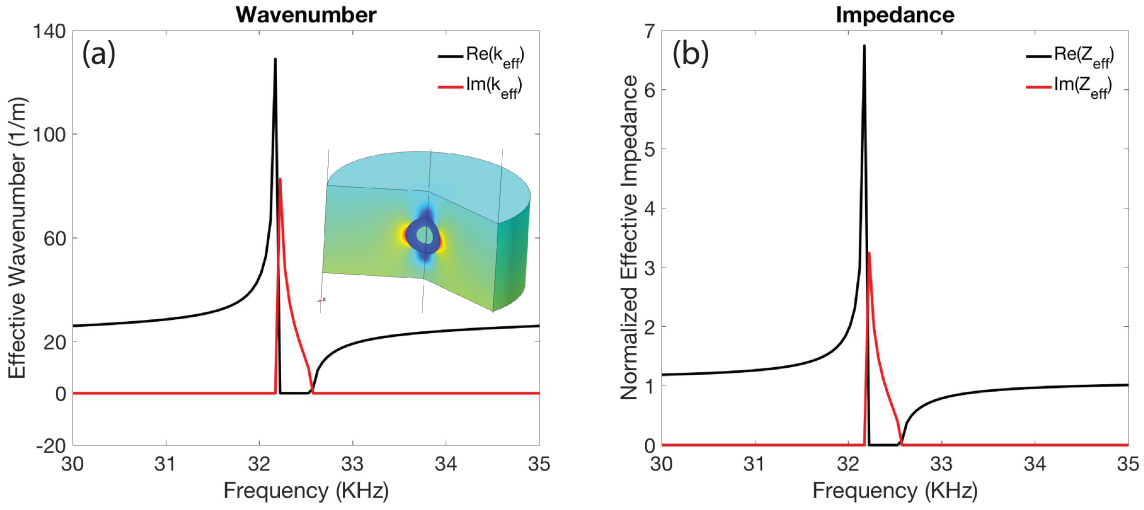

Figure 5.3. Retrieved effective impedance and wavenumber of the unit cell of LRAM. (a) Effective wave number with the unit cell of LRAM shown here. (b) Effective impedance of the LRAM.

Furthermore, increasing the size of the sphere may indeed alter the static mechanical properties of the matrix material such as mechanical stiffness. In contrast, bi-layer configuration (hard-core, Soft-shell) confers added degrees of freedom, enabling us to tune its resonance frequencies independent of the sphere's radius, and subsequently realize the least change in the static properties of the matrix material.

The effective impedance and wavenumber of the LRAM are shown in **Figure 5.3**. From the effective wavenumber shown in **Figure 5.3(a)**, it may be observed that from 32 KHz to the peak of wavenumber (approximately at 32.1 KHz), the imaginary part of the wavenumber remains negligible. Furthermore, in the narrow range of the frequency (32.1 KHz to 32.6 KHz), the LRAM shows a dispersive behavior with the purely imaginary wavenumber. Eventually, after this band (+32.6 KHz), the imaginary part of the wavenumber is diminished, and the attenuation will be negligible. Therefore, one may infer that outside of the dispersive band (32.1KHz-32.6 KHz), the variation in the effective impedance in the range of (32KHz to 33 KHz) that spans from the value of near-zero to about 6 times of the matrix material's impedance, may be leveraged and utilized with minimal attenuation in the propagating wave.

Up to now, it is demonstrated that in the class of LRAM, such as the composite of spherical inclusions dispersed in the matrix material, there exists a large variation in the effective acoustic impedance, near the resonance of the inclusions. It is further discussed that this large impedance variation, emerges in the vicinity of both monopole and dipole resonances of the inclusion. Eventually, it is clarified that despite the dispersive behavior of the LRAM in the proximity of the resonances, effective impedance variation emerges

prior to the initiation of dispersive behavior in the medium. Next, two distinct cases will be discussed herein where this abnormal behavior in the class of LRAM may be leveraged.

5.2 LRAM as a contrast agent

Wellbore damage commonly results from poorly placed cement, and consequently, it is of utmost importance to monitor and image the cement condition in the downhole environment. The properly cemented well with defect-less cement ensures the hydraulic isolation between the reservoirs layers and shallow aquifers, which can guarantee production efficiency as well as safety. For cementing quality control, it is necessary to image the structures outside the casing, especially the interfaces between cement and fluid channel as well as between cement and formation.

The ultrasonic-based imaging approaches are mainly based on the acoustic impedance contrast between borehole fluid and the material behind the casing. The acoustic impedance contrast in the interface between two media will generate the reflected pulse, which can be detected by the transducer for the imaging purpose. Thereby, when there is not a significant contrast between two mediums, the received signal for imaging will be very weak and consequently imaging in a downhole environment very challenging. To date, an acoustic-based approach for wellbore cement's defect detection has suffered from unremarkable acoustic impedance contrast between cement and borehole fluid (Wang et al., 2016). This insignificant acoustic impedance contrast between cement and borehole fluid is more problematic in the case of low-density cement, which has drastically limited the defect detection capacity. Given the fact the acoustic impedance essentially

corresponds to the mechanical properties of the material, cement in here, altering the impedance of cement while maintaining its mechanical properties is challenging. Herein, it is intended to demonstrate how the concept of impedance variation in the class of LRAM may be leveraged to address this issue.

Let us consider the case when bilayer spherical inclusions are mixed with the cement in its production stage with 4% volume ratio. This case is identical to the case considered and analyzed before, and its effective impedance is shown in **Figure 5.3 (b)**. From **Figure 5.3 (b)** it may be readily observed that by addition of the bilayer spheres with only 4% volume ratio, the effective impedance of the whole mixture may reach to about 6x of its static value in near the resonance. Consequently, by sweeping the signal in an only a narrow range of the frequency (32-33 KHz), the variation in the effective impedance may provide the sufficient degree of impedance mismatch required for NDE process.

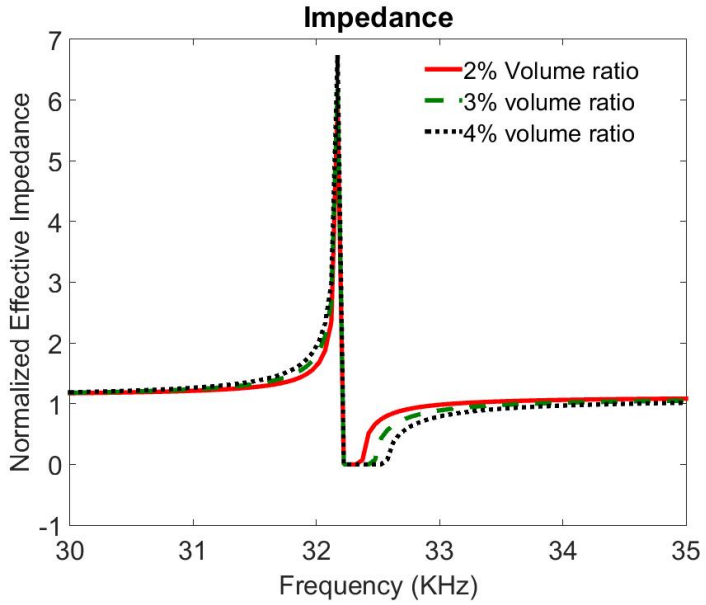

Figure 5.4. Effective impedance variation (real-part) of the cement/sphere composite with different volume ratios of the spherical inclusions.

Notably, the resonance frequency of the single spherical particles is the dominant factor in overall impedance variation, and the change in the spatial volume ratio has a minimal effect on the overall behavior. Shown in **Figure 5.4**, with alteration in the volume ratio of the spheres from 4% to 2%, the general trend of the impedance variation remains relatively unchanged save for a minor drop in the peak value. In order to validate the proposed concept, herein, a simplified case of ultrasound-based cement bond logging (shown in **Figure 5.5**) is modeled in which reflected ultrasound wave might be utilized to evaluate the bond between cement and the casing. The harmonic acoustic wave is generated from the left-hand side of the casing and reflection coefficient has been probed for different cases both with and without the presence of defect layer between cement and casing and the effect of the spherical inclusion has been studied.

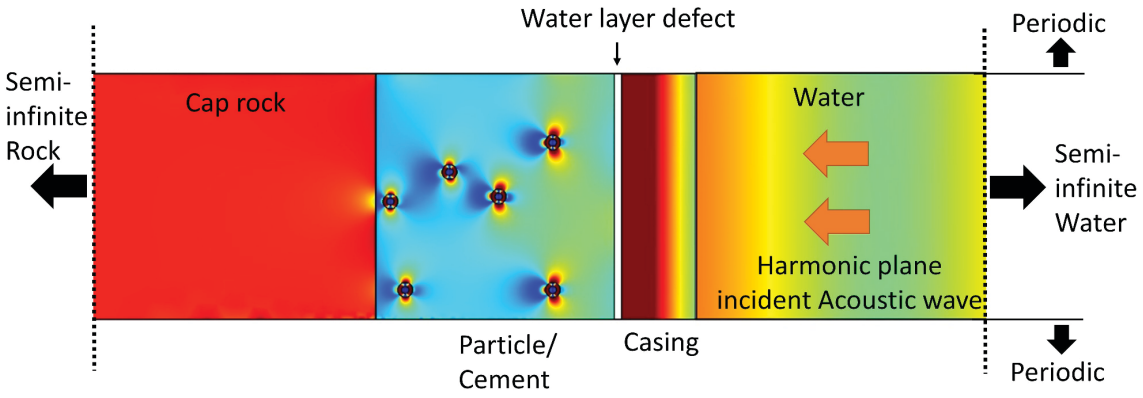

Figure 5.5. Illustration of the numerical model to investigate the functionality of the bilayer spherical inclusions as a contrast agent for cement bond logging.

The resulted complex reflection is shown in **Figure 5.6**. In case of pure cement shown in **Figure 5.6 (a) & (b)**, for the three cases of no defect, defect with the 500um thickness and 1mm defect, there exists a small variation in reflection amplitude and negligible change in

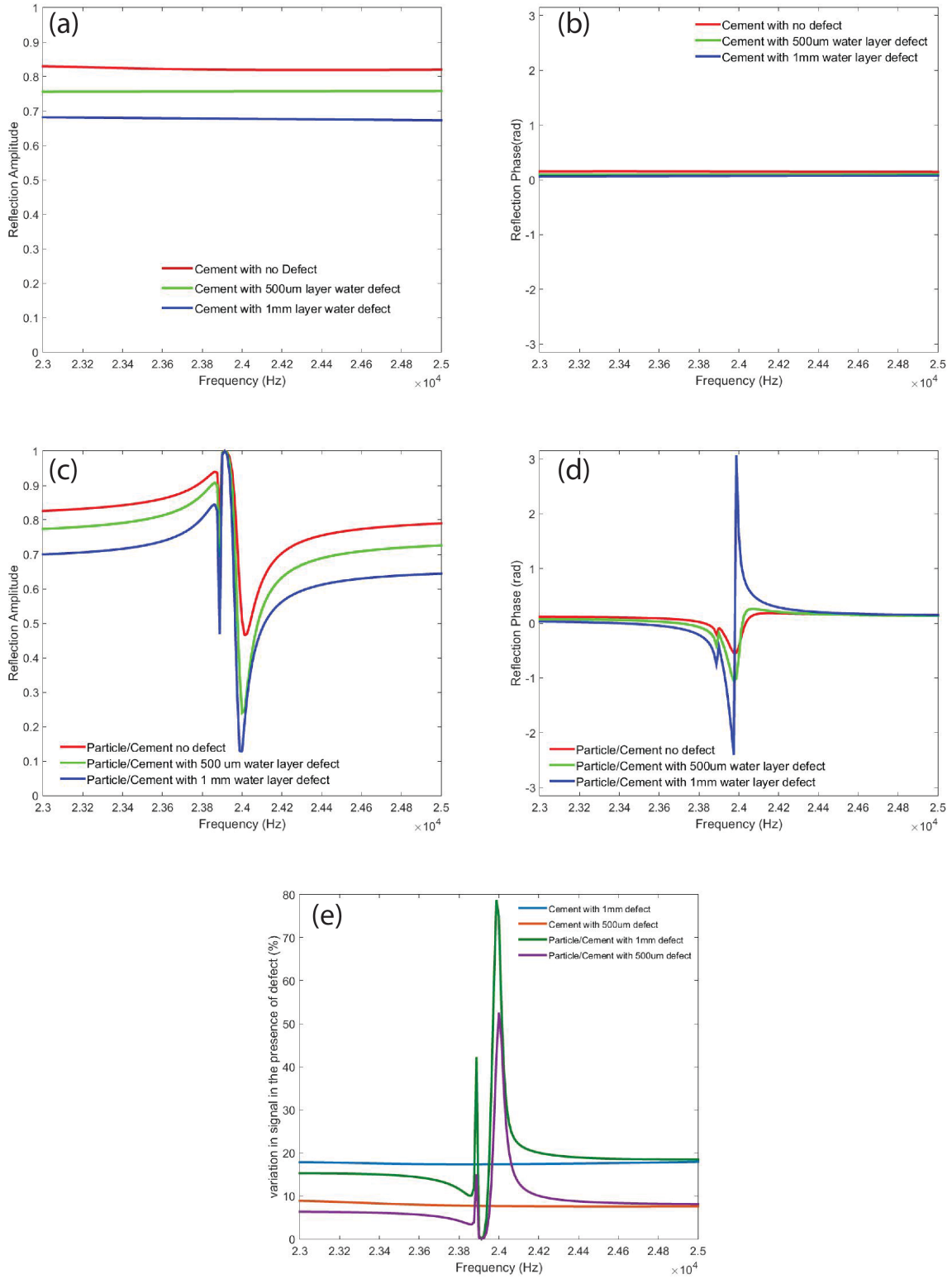

Figure 5.6. Complex reflection in ultrasound-based cement bond logging. (a) & (b) cement. (c) & (d) Cement with bilayer spherical inclusion. (e) Signal variation ratio.

the reflection phase. Moreover, the reflection amplitude is relatively high, which corresponds to the reflection of the wave from the water/casing interface. By the addition of the spherical particles in the cement and as an LRAM, shown in **Figure 5.6 (c) & (d)**, for the three cases of the defect condition, there exist a substantial alteration in the trend of both reflection amplitude and reflection phase. The percentage variation of the reflection amplitude with the presence of the defect with respect to the no defect condition is summarized in **Figure 5.6 (e).**

From **Figure 5.6 (e)**, it may be inferred that in the case of 500um thickness defect, the reflection amplitude changes less than 10 % in case of pure cement and about 50% in case of cement/particles respect to the reflection amplitude of the no-defect case. Similarly, for 1mm defect layer, the reflection amplitude change is about 20% in pure cement and may reach about 80% in cement/particle composite.

The results obtained herein demonstrates that the addition of the spherical inclusion in the cement, even in a low volume ratio, may significantly enhance the detection capacity by functioning as a contrast agent. In this approach by designing the tuned spherical resonator and integrating it with the cement, and sweeping the ultrasound signal, a sufficient degree of impedance mismatch may be obtained for successful NDE. Implementation of this concept may open up new possibilities in NDE in the downhole environment.

In **Figure 5.6 (c)**, one may correctly point out that there exists an unexpected region where the reflection is near zero despite the presence of the casing and cement layer. This interesting phenomenon and its origin is the subject of the next section of this chapter and

will be discussed here in more detail.

5.3 LRAM as an Anti-Reflection Layer

Ultrasound represents a powerful tool in the armamentarium of modern healthcare that is widely applied across a spectrum of disease. Ultrasound is safe, lacking the ionizing radiation of CT or the need for the high-field magnetic environment of MRI, relatively inexpensive, an utmost consideration in healthcare, and both portable and highly flexible, allowing for its use in a variety of settings, both within and beyond the hospital. In addition to imaging, ultrasound is a burgeoning therapeutic modality as high-intensity focused ultrasound represents a rapidly evolving ablative therapy enabling the non-invasive treatment of a wide variety of conditions ranging from oncological to neurological and beyond. Furthermore, with the capacity to reversibly excite and inhibit neural activity, low-intensity focused ultrasound, in its application to noninvasive neuromodulation, is garnering tremendous interest given is potential in neuroscience research and clinical neurological therapeutics.

However, one of the fundamental and outstanding shortcomings of ultrasound is the limitation imposed by transmission through underlying layers of bone, which results in undesirable changes in the acoustic signal amplitude or phase. Specifically, underlying bone results in reflection, refraction, and attenuation of the ultrasound beam, thereby resulting in a marked loss of signal amplitude. Furthermore, the presence of underlying layers of bone results in phase aberrations in the propagation of the ultrasound beam due to variations in speed as a function of the path through the bone. Ultimately, the presence

of underlying layers of bone precludes, for example, ultrasound imaging of the brain due to the bony calvarium, increases the challenges of transthoracic imaging of the heart due to the overlying bony sternum and ribs, and imposes limitations on transcranial focused ultrasound. Of the aforementioned effects due to the underlying bone, reflection represents a predominant component limiting transmission through a bone (Fry et al., 1978; Pinton et al., 2012; Gerstenmayer et al., 2018).

Throughout the last century, there has been an ongoing effort to reduce reflection through the application of anti-reflective coatings (ARCs) on reflective surfaces. The development of ARCs began with Rayleigh in 1879 (Rayleigh L., 1897) when he proposed that the reflectivity from the outer surface of an object could be reduced on the condition that the transition of the refractive indices between the object and its surrounding medium is small. Following this proposal by Rayleigh, various methods and strategies have been developed in order to lessen optical reflection, including single-, double- or multi-layer ARCs or structuring/patterning of the surface, among others (Rahman et al., 2015; Xi et al., 2007). Among the most well-known optical AR coatings are the quarter-wavelength coating in which zero-reflection and full transmission occur when the refractive index of the AR is equal to the geometrical mean of the substrate and 'environmental' medium refractive indices.

In the case of acoustic waves, the wave behavior at the interface between two media is dominated by the characteristic acoustic impedance, which is related to a medium's density and speed of sound. Analogous to the media's refractive indices in the case of optical waves, the impedance mismatch between two domains determines the degrees of

acoustic reflection or transmission at their interface. The use of single or multilayer structures as ARCs has also been investigated in the case of acoustic waves (Martin BG., 1992; Cheng et al., 1991; Kushibiki et al., 1981), however, due to the larger wavelengths of acoustic wave and the need for ARCs with comparable thickness, these conventional approaches tend to be impractical and, therefore, the history of acoustic ARCs is not as rich as their optical counterparts.

Recently, acoustic metamaterial structures have been proposed to function as antireflection coatings. Bok et al. proposed a deep subwavelength metamaterial composed of a decorated membrane coupled to a cavity from which acoustic wave transmission from water-to-air can be increased by up to 2 orders of magnitude by mitigating reflection (Bok et al., 2018). Furthermore, and more relevant to the aims herein, Shen et al. recently proposed their concept of an acoustic metamaterial-based complementary layer designed to cancel the effect of an underlying aberrant layer (Shen et al., 2014).

Despite the potential significance of the ultrasound-based applications of acoustic antireflection coating technology, there exists a fundamental shortcoming of the concepts presented to date that precludes their practical functionality to these applications. That shortcoming is the fact that the ARCs proposed to date, whether more conventional in nature or metamaterial-based, are designed to mitigate reflection from an object of uniform thickness and specific material properties. Consequently, any variation in the thickness or material inhomogeneity within the layer from which reflection is to be mitigated significantly affects the ARC's performance. This drawback is significantly problematic in the proposed application of ultrasound in the setting of underlying layers of bone given the

lack of uniformity in both thickness and material properties of bone (calvarium, for example, in the case of transcranial ultrasound).

In order to illustrate the necessary conditions for realizing a functional ARC, one may consider the simple case of a single-layer coating applied to an underlying aberrating layer (**Figure 5.7**). An ideal ARC design will result in the significantly enhanced transmission of an acoustic wave through the skull, which would not be the case in the absence of the ARC, given the large impedance mismatch between water (or soft tissue) and skull. By initially deriving the transfer matrix for both the ARC and the underlying skull and assuming the propagation of the plane wave, one may derive the necessary condition for zero reflection and enhanced transmission as follows:

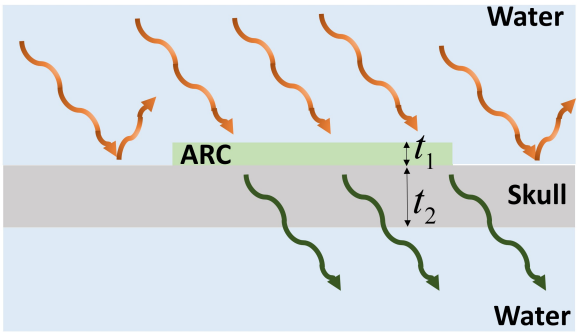

Figure 5.7. Application of the acoustic antireflection coating (ARC) on the skull

$$\psi = 2\cos(k_1 t_1)\cos(k_2 t_2) - \left(\frac{Z_2}{Z_1} + \frac{Z_1}{Z_2}\right)\sin(k_1 t_1)\sin(k_2 t_2) + j\left[\left(\frac{Z_w}{Z_1} + \frac{Z_1}{Z_w}\right)\sin(k_1 t_1)\cos(k_2 t_2) + \left(\frac{Z_2}{Z_w} + \frac{Z_w}{Z_2}\right)\cos(k_1 t_1)\sin(k_2 t_2)\right] \tag{5.1}$$

When the transmission amplitude may be derived as:

$$|T| = \frac{2}{|\psi|} \tag{5.2}$$

Where t_1 and t_2 are the thickness of the ARC and skull layer shown in **Figure 5.7**. k_1 is the wavenumber in ARC and k_2 is the wavenumber associated with the skull layer. Z_1, Z_2 and Z_w denotes the characteristic acoustic impedance of ARC, skull, and water, respectively.

From the Equation above, one may readily infer that for given values of layer thickness and certain material properties, by optimizing the nonlinear Equation, the proper values of Z_1 and t_1 may be found in which amplitude of ψ approximates 2, consequently, zero reflection and significantly enhanced transmission may be achieved. However, as discussed above, in order to ensure the practical implementation of an acoustic ARC design methodology, it is of utmost importance to maintain ARC performance under variations in the aberrating layer's (bone in this example) thickness and material properties. Herein, in order to address this fundamental challenge, we propose to develop a nonlinear acoustic metamaterial coating (nAMC).

The underlying concept enabling the nAMC design entails the consideration of the reverse of the design path. That is, as opposed to directly deriving the appropriate value of the ARC's impedance (Z_1) from the Equation above, a coating layer featuring a large range in effective acoustic impedance (Z_1) with variations in frequency will be developed. Considering the layer of nAMC composed of the matrix material with embedded spherical resonators, it has been shown before that for such LRAM, there exists a large impedance variation in the vicinity of the spherical inclusion resonances. Furthermore, as it is shown

in **Figure 5.2(a)**, the effective stiffness remains unchanged in the vicinity of the dipole resonance (f_1). Consequently, one may derive that:

$$k_1 = Z_1 \frac{\omega}{M} \tag{5.3}$$

Where M is the stiffness of the matrix material. The presence of such a linear relationship between effective impedance and effective wavenumber may be further seen in **Figure 5.3**. Employing equation (5.3), equation (5.1) may be written in the form of:

$$\begin{aligned} \psi = 2\cos(Z_1 \frac{\omega}{M} t_1)\cos(k_2 t_2) - (\frac{Z_2}{Z_1} + \frac{Z_1}{Z_2})\sin(Z_1 \frac{\omega}{M} t_1)\sin(k_2 t_2) + \\ j\left[(\frac{Z_w}{Z_1} + \frac{Z_1}{Z_w})\sin(Z_1 \frac{\omega}{M} t_1)\cos(k_2 t_2) + (\frac{Z_2}{Z_w} + \frac{Z_w}{Z_2})\cos(Z_1 \frac{\omega}{M} t_1)\sin(k_2 t_2) \right] \end{aligned} \tag{5.4}$$

As mentioned before, the condition for the full transmission may be achieved when the function ψ reaches its global minimum, and its amplitude at the global minimum approximates 2. For a given layer of skull with arbitrary thickness and impedance, from equation (5.4) one may conclude that for the designed layer of nAMC with the thickness of t_1 and stiffness of *M,* by sweeping the signal in the narrow range of the frequency (assuming constant ω), the only remained variable is Z_1 , and it is very likely that the equation (5.5) will be satisfied once the value of Z_1 varies from the zero to the substantial value.

$$\frac{\partial \psi}{\partial Z_1} = 0 \tag{5.5}$$

The large variation in Z_1 may likely satisfy the equation (5.5) in multiple values, and consequently, the local minimum and maximum of the transmission will emerge in the narrow band of the frequency regardless of the impedance and thickness of the aberrant layer. Such behavior may be very well observed in **Figure 5.6 (c)** in which both full reflection and negligible reflection have emerged in the narrow range of the frequency. This methodology for the design of the nAMC leveraging the concept of LRAM will enable one to realize enhanced transmission from the reflective layer without constraining the impedance and thickness of the reflective layer to some exact values. In fact, with properly designed nAMC one may obtain the large transmission through the layer of bone even in case of variation in thickness and effective impedance of bony layer.

Notably, considering that within the context of the presented methodology for the design of nAMC, the local minimum and maximum of the ψ will emerge in the narrow range of the frequency, the values of the nAMC thickness (t_1) and stiffness (M) need to be optimized based on the expected value and variation in the aberrant layer's thickness and impedances. Otherwise, on the local minimums of ψ, its amplitude will not approximate the value of 2, and consequently, only the incremental improvement in the transmission may be achieved rather than the full transmission. Shown in **Figure 5.8**, the layer of non-optimized nAMC has been employed to increase the transmission through the skull. It may be observed by leveraging the nAMC, the transmission through the layer of the skull has increased from less than 0.1 to about 0.27.

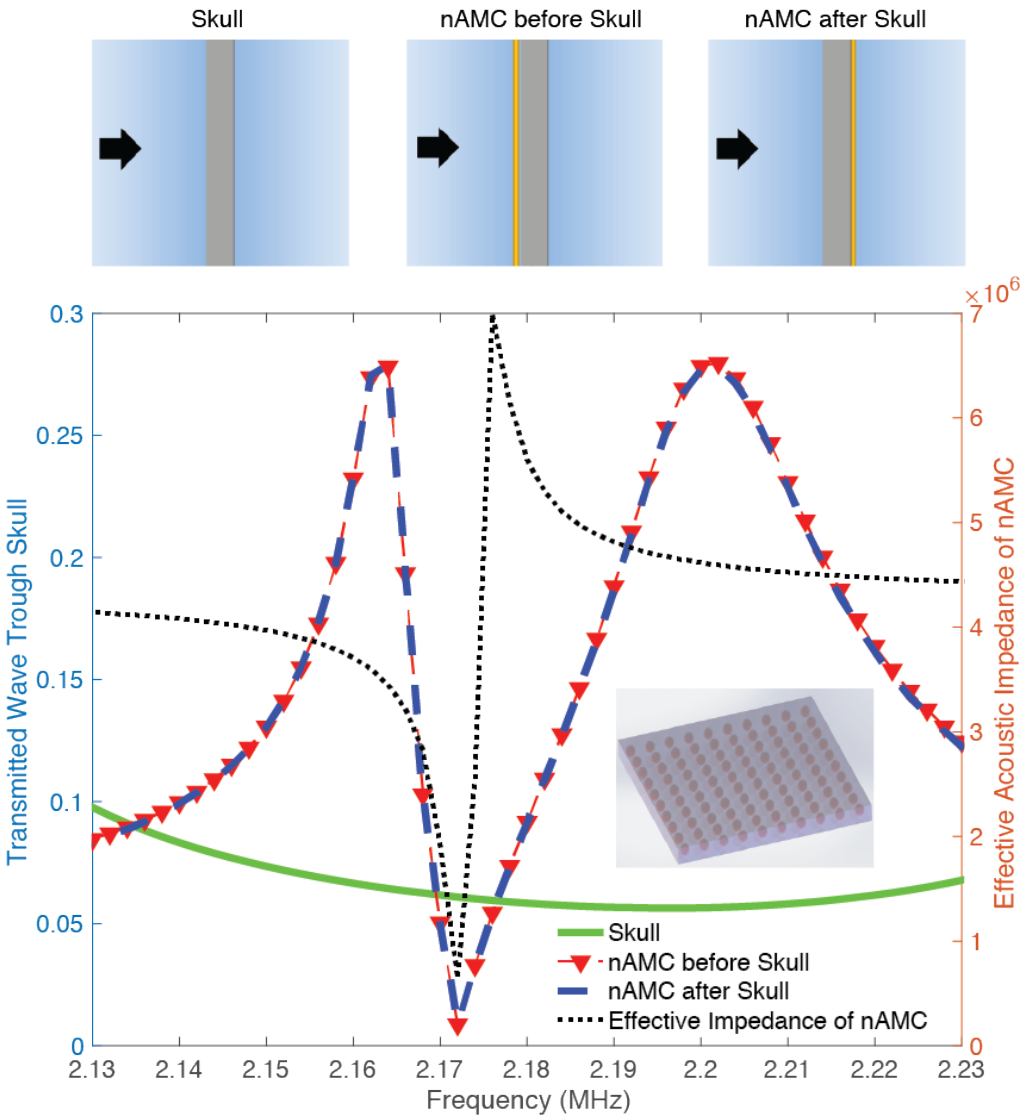

Figure 5.8. Application of the nAMC to realize enhanced transmission through the skull.

The three-time increase (3x) in the transmitted signal to the brain and consequently, 3x increase in the reflected signal from the brain, results in about 9x enhancement in the signal utilized for brain imaging. Notably, with the optimization of the nAMC properties, one may achieve markedly better results that may potentially enable the practical realization of the ultrasound brain imaging.

CHAPTER 6 CONCLUSION

Metamaterial and metasurfaces represent potential tools for modulation of the acoustic wave. Leveraging these novel structures and methodology, one may address the longstanding acoustical challenges present today. In this dissertation, several aspects of metamaterial-based acoustic wave manipulation have been studied.

In the dissertation herein, initially, the horn-like space coiling metamaterial has been introduced that enabled us to simultaneously modulate transmission phase and amplitude. The addition of amplitude modulation to phase modulation may lead to marked simplification of the wavefront modulation leveraging phase-conjugate method. Moreover, the added degree of freedom will enhance the capacity to precisely shape the wavefront (Ghaffarivardavagh et al., 2018).

Furthermore, the concept of the double decorated membrane is introduced, which represent a promising pathway for real-time modulation of the transmission phase with minimal amplitude variation. In this thesis, in addition to the numerical validation of the theory, the double decorated membrane structure has been initially tested experimentally, and the challenges with regard to its practical realization are discussed (Ghaffarivardavagh et al., 2017). Notably, in Appendix E, the novel experimental method, namely Ultimate Wave Decomposition (UWD) is presented for measuring the precise transmission and reflection through material/metamaterial (Ghaffarivardavagh et al., 2019). In these two chapters of this dissertation, drawbacks associated with current metasurface-based wavefront modulation are addressed by firstly, the addition of amplitude modulation to the

phase modulation and secondly, proposing the pathway toward real-time phase modulation.

In chapter 4 and 5 of this dissertation, the metamaterial-based approaches have been pursued to alter the transmission/reflection amplitude profile. Elaborately, the concept of ultra-open metamaterial silencer has been introduced in which leveraging Fano-like interference, the silencing functionality has been realized while marinating efficient ventilation. The concept proposed herein may be readily applied to several distinct applications ranging from noise reduction in Fan and HVAC to cavity noise suppression in the automobile industry (Ghaffarivardavagh et al., 2019). Eventually, in chapter 5 of this dissertation, the abnormal behavior in a locally resonant class of acoustic metamaterial has been elaborated, and its potentiation application in two distinct cases have been proposed.

This dissertation is devoted to better leverage and utilize the metasurface and metamaterials science to bridge the gap for real-world implementation of these novel structures.

APPENDIX

A. Transfer Matrix Method (TMM) to Derive the Complex Transmission

In this section, the transmission through the space-coiling structure has been derived analytically, considering the complex internal geometry (**Figure A. 1(a)**). To this end, the transfer matrix method has been utilized to extract the governing relationship and correlate input pressure and velocity to the output condition. Considering a single coil of a unit cell (**Figure A. 1(b)**) of the space-coiling metamaterial, one may derive the propagation tensor that relates the output condition to the input condition, which can be written in the form of:

$$\begin{bmatrix} P_2 \\ U_2 \end{bmatrix} = [M_1] \begin{bmatrix} P_1 \\ U_1 \end{bmatrix} \tag{A.1}$$

Eventually, total transmission through the space-coiling structure (Figure I.1a) may be derived as below:

$$\begin{bmatrix} P_{\text{out}} \\ U_{\text{out}} \end{bmatrix} = [M_N] \ldots . [M_2][M_1] \begin{bmatrix} P_{\text{in}} \\ U_{\text{in}} \end{bmatrix} \tag{A.2}$$

Please note that for conventional space-coiling metamaterials in which the channel width is uniform throughout the unit cell, all propagation tensors (Ms) would be identical, and this would represent a unique case. However, in the case of the gradient space-coiling metamaterials introduced in Chapter 2, the use of the transfer matrix method remains applicable, though due to the change in geometry from the coil to coil, the propagation tensor would not necessarily remain identical.

In order to determine the propagation tensor in a single coil, the region has been divided into the three sections shown in **Figure A. 1(b)**.

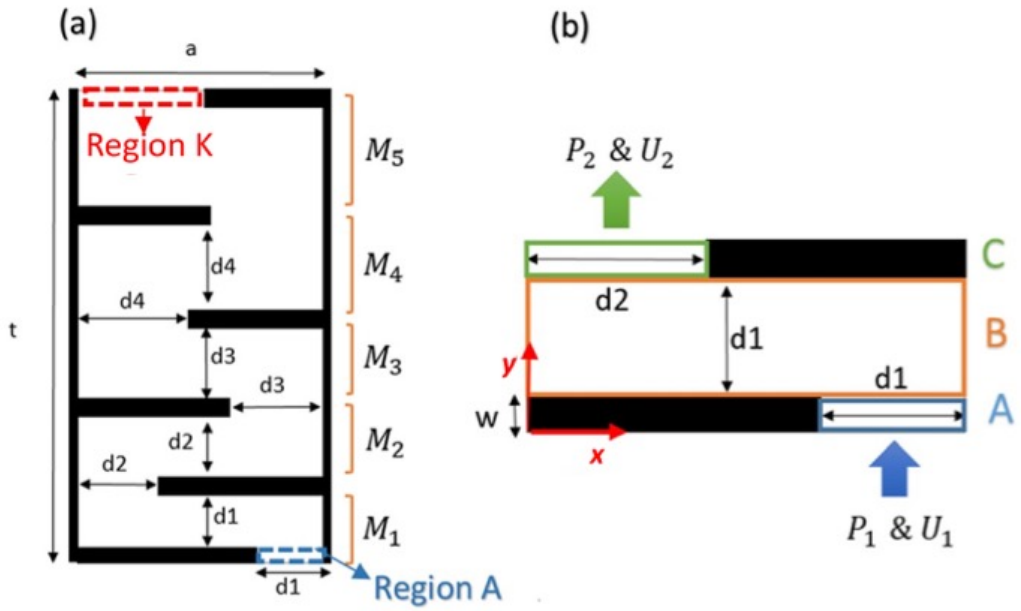

Figure A.1. Illustration of the internal structure of space–coiling unit cell. (a) Space-coiling structure associated propagation tensor for each section. (b) Single coil structure, which has been divided into three sections: section A is the input port, section B is the main channel, and section C is the output port.

Pressure and velocity in each region can be written using modal superposition in the rectangular waveguide, however, since regions A and C have relatively small dimensions when compared to the wavelength, only the principal mode is considered herein for these two regions. Pressure and velocity in these regions are as follow:

$$\mathrm{A}:\begin{cases} P(y) = A_1 \mathrm{e}^{iky} + A_2 \mathrm{e}^{-ik(y-w)} \\ U(y) = \dfrac{1}{\rho c}\left[A_1 \mathrm{e}^{iky} - A_2 \mathrm{e}^{-ik(y-w)} \right] \end{cases} \qquad \text{(A. 3a, A. 3b)}$$

$$\mathrm{C}:\begin{cases} P(y) = C_1 \mathrm{e}^{ik(y-w-d1)} + C_2 \mathrm{e}^{-ik(y-2w-d1)} \\ U(y) = \dfrac{1}{\rho c}\left[C_1 \mathrm{e}^{ik(y-w-d1)} - C_2 \mathrm{e}^{-ik(y-2w-d1)} \right] \end{cases} \qquad \text{(A. 4a, A. 4b)}$$

$$\mathrm{B}:\begin{cases} P(x,y)=\sum_{n=0}^{\infty}\cos(a_n x)\left[B_{1n}\mathrm{e}^{ik_n(y-w)}+B_{2n}\mathrm{e}^{-ik_n(y-w-d1)}\right] \\ U(x,y)=\sum_{n=0}^{\infty}\frac{k_n}{\rho ck}\cos(a_n x)\left[B_{1n}\mathrm{e}^{ik_n(y-w)}-B_{2n}\mathrm{e}^{-ik_n(y-w-d1)}\right] \end{cases} \quad \text{(A. 5a, A. 5b)}$$

In which wave number is defined as $k=\frac{\omega}{c}$ and the n^{th} eigenmode and wavenumber in region B can be derived as $a_n=\frac{n\pi}{a}$, $k_n=\sqrt{k^2-a_n^2}$. The geometrical parameters *a*, *w* and *d1* are shown in **Figure A. 1(b)**. Given the above equations, one may conclude that the problem of deriving Equation (A.1) for a single coil can be reduced to deriving the relationship between the coefficient of A and C in which A_1 and C_1 are forward traveling wave coefficients and A_2 and C_2 are backward traveling wave coefficients as follows:

$$\begin{bmatrix} C_1 \\ C_2 \end{bmatrix}=[T_1]\begin{bmatrix} A_1 \\ A_2 \end{bmatrix} \quad \text{(A.6)}$$

Consequently, the relation between input and output condition for the whole structure may be derived as below.

$$\begin{bmatrix} K_1 \\ K_2 \end{bmatrix}=[T_N]\ldots.[T_2][T_1]\begin{bmatrix} A_1 \\ A_2 \end{bmatrix} \quad \text{(A.7)}$$

In which the forward traveling wave coefficient K_1 and the backward traveling wave coefficient K_2 corresponding to the output port of the final coil shown in **Figure A. 1(a)**. Next, pressure and velocity boundary conditions at $y = w$ and $y = d1+w$ have been applied.

At: $y = w$, $a - d1 \le x \le a$

$$A_1 e^{ikw} + A_2 = \sum_{n=0}^{\infty} \cos(a_n x)\left[B_{1n} + B_{2n} e^{ik_n d1}\right] \tag{A.8}$$

$$\left[A_1 e^{ikw} - A_2\right] = \sum_{n=0}^{\infty} \frac{ak_n}{d_1 k} \cos(a_n x)\left[B_{1n} - B_{2n} e^{ik_n d1}\right] \tag{A.9}$$

At: $y = w + d1$, $0 \le x \le d2$

$$C_1 + C_2 e^{ikw} = \sum_{n=0}^{\infty} \cos(a_n x)\left[B_{1n} e^{ik_n d1} + B_{2n}\right] \tag{A.10}$$

$$\left[C_1 - C_2 e^{ikw}\right] = \sum_{n=0}^{\infty} \frac{ak_n}{d_2 k} \cos(a_n x)\left[B_{1n} e^{ik_n d1} - B_{2n}\right] \tag{A.11}$$

In order to ensure that Equations (A.8) to (A.11) are a solvable set of equations to relate the coefficients in Region A (A_1 and A_2) and Region C (C_1 and C_2), one needs to relieve the x-dependency, along with deriving the n^{th} mode's coefficient in Region B. Thus, the problem has been simplified by first multiplying the velocity boundary conditions (Equation (A.9) and Equations (A.11)) by the factor of $\cos(a_m x)$ and taking the normalized line integral with respect to x from both sides of Equations (A.8) to (A.11). Given the orthogonally of the trigonometric functions, the summation terms in the right-hand-side of Equation (A.9) and Equation (A.11) will vanish, save for the case when m = n. Eventually, the simplified form of the boundary conditions yields the following:

At: $y = w$

$$A_1 e^{ikw} + A_2 = \sum_{n=0}^{\infty} \frac{1}{d1} \int_{a-d1}^{a} \cos(a_n x)\, dx \left[B_{1n} + B_{2n} e^{ik_n d1}\right] \tag{A.12}$$

$$\left[A_1 e^{ikw} - A_2\right]\frac{1}{d1}\int_{a-d1}^{a}\cos\left(a_n x\right)dx = \frac{ak_n}{\acute{U}_n d_1 k}\left[B_{1n} - B_{2n}e^{ik_n d1}\right] \tag{A.13}$$

At: $y = w + d1$

$$C_1 + C_2 e^{ikw} = \sum_{n=0}^{\infty}\frac{1}{d2}\int_{0}^{d2}\cos\left(a_n x\right)dx\left[B_{1n}e^{ik_n d1} + B_{2n}\right] \tag{A.14}$$

$$\left[C_1 - C_2 e^{ikw}\right]\frac{1}{d2}\int_{0}^{d2}\cos\left(a_n x\right)dx = \frac{ak_n}{\acute{U}_n d_2 k}\left[B_{1n}e^{ik_n d1} - B_{2n}\right] \tag{A.15}$$

In which Neumann Factor, ϵ_n ,is defined as $\epsilon_n = 2$ for $n \neq 0$ and has the value of $\epsilon_n = 1$ if $n = 0$.

Using Equation (A.13) and Equation (A.15), B_{1n} & B_{2n} can be derived in terms of *A*'s and *C*'s coefficients and, consequently, by substituting in Equation (A.12) and Equation (A.14), the relationship between *A*'s and *C*'s coefficients are thusly determined:

$$\begin{bmatrix}C_1\\C_2\end{bmatrix} = \left[T_1\right]\begin{bmatrix}A_1\\A_2\end{bmatrix} \rightarrow \begin{bmatrix}C_1\\C_2\end{bmatrix} = \begin{bmatrix}T_{11} & T_{12}\\T_{21} & T_{22}\end{bmatrix}\begin{bmatrix}A_1\\A_2\end{bmatrix} \tag{A.16}$$

$$T_{11} = \frac{e^{ikw}\left(\gamma_3\gamma_1 + \gamma_2\right)}{\left(1+\gamma_1\right)} \tag{A.17}$$

$$T_{12} = \frac{\left(\gamma_4\gamma_1 - \gamma_2\right)}{\left(1+\gamma_1\right)} \tag{A.18}$$

$$T_{21} = \frac{\left(\gamma_2 - \gamma_3\right)}{\left(1+\gamma_1\right)} \tag{A.19}$$

$$T_{22} = \frac{-\left(\gamma_4 + \gamma_2\right)}{e^{ikw}\left(1+\gamma_1\right)} \tag{A.20}$$

In which $\gamma_1, \gamma_2, \gamma_3$and γ_4 are derived as follows:

$$\gamma_1 = \frac{1+\left[\sum_{n=0}^{\infty}\frac{\varphi_n^2}{d_2}\left(\frac{2\acute{U}_n k\varphi_n^2\ (e^{2ik_n d_1}+1)}{ak_n\left(e^{2ik_n d_1}-1\right)}\right)\right]}{1-\left[\sum_{n=0}^{\infty}\frac{\varphi_n^2}{d_2}\left(\frac{2\acute{U}_n k\varphi_n^2\ (e^{2ik_n d_1}+1)}{ak_n\left(e^{2ik_n d_1}-1\right)}\right)\right]} \tag{A.21}$$

$$\gamma_2 = \frac{\left[\sum_{n=0}^{\infty}\frac{\varphi_n^2}{d_2}\left(\frac{4\acute{U}_n k\varphi_n^1\ (e^{ik_n d_1})}{ak_n\left(e^{2ik_n d_1}-1\right)}\right)\right]}{\left[\sum_{n=0}^{\infty}\frac{\varphi_n^2}{d_2}\left(\frac{2\acute{U}_n k\varphi_n^2\ (e^{2ik_n d_1}+1)}{ak_n\left(e^{2ik_n d_1}-1\right)}\right)\right]-1} \tag{A.22}$$

$$\gamma_3 = \frac{1+\left[\sum_{n=0}^{\infty}\frac{\varphi_n^1}{d_1}\left(\frac{2\acute{U}_n k\varphi_n^1\ (e^{2ik_n d_1}+1)}{ak_n\left(e^{2ik_n d_1}-1\right)}\right)\right]}{\left[\sum_{n=0}^{\infty}\frac{\varphi_n^1}{d_1}\left(\frac{4\acute{U}_n k\varphi_n^2\ (e^{ik_n d_1})}{ak_n\left(e^{2ik_n d_1}-1\right)}\right)\right]} \tag{A.23}$$

$$\gamma_4 = \frac{1-\left[\sum_{n=0}^{\infty}\frac{\varphi_n^1}{d_1}\left(\frac{2\acute{U}_n k\varphi_n^1\ (e^{2ik_n d_1}+1)}{ak_n\left(e^{2ik_n d_1}-1\right)}\right)\right]}{\left[\sum_{n=0}^{\infty}\frac{\varphi_n^1}{d_1}\left(\frac{4\acute{U}_n k\varphi_n^2\ (e^{ik_n d_1})}{ak_n\left(e^{2ik_n d_1}-1\right)}\right)\right]} \tag{A.24}$$

In Equations A.21 to A.2 4, φ_n^1 and φ_n^2 are defined as follows:

$$\varphi_n^1 = \int_{a-d1}^{a} \cos(a_n x)\,dx \tag{A.25}$$

$$\varphi_n^2 = \int_{0}^{d2} \cos(a_n x)\,dx \tag{A.26}$$

Employing Equations (A.16) to (A.26), the propagation tensor for a single coil of a unit cell (Equation A.6) can be calculated. By taking into account the effects of all coils in the space-coiling metamaterial, the propagation tensor correlating the last output port (output of the entire unit cell) to the coefficients of the first input port (input of the entire unit cell) can be derived using Equation (A.7). Finally, employing the resultant propagation tensor of the space-coiling structure, the transmission coefficient may be calculated as follow.

Pressure and velocity boundary condition at $y = 0$ (**Figure A.2**):

$$P_{\mathrm{I}} + P_{\mathrm{R}} = A_1 + A_2 \mathrm{e}^{ikw} \tag{A.27}$$

$$P_{\mathrm{I}} - P_{\mathrm{R}} = \frac{d_{\mathrm{in}}}{a}(A_1 - A_2 \mathrm{e}^{ikw}) \tag{A.28}$$

Pressure and velocity boundary condition at $y = t$:

$$P_{\mathrm{T}} = K_1 \mathrm{e}^{ikw} + K_2 \tag{A.29}$$

$$P_{\mathrm{T}} = \frac{d_{\mathrm{out}}}{a}(K_1 \mathrm{e}^{ikw} - K_2) \tag{A.30}$$

Additionally, using the propagation tensor derived for the space-coiling structure, K's coefficient can be defined in terms of A's coefficients.

$$\begin{bmatrix} K_1 \\ K_2 \end{bmatrix} = \begin{bmatrix} M_{11} & M_{12} \\ M_{21} & M_{22} \end{bmatrix} \begin{bmatrix} A_1 \\ A_2 \end{bmatrix} \tag{A.31}$$

Using Equations (A.27) to (A.31), the complex transmission ($T = \frac{P_{\mathrm{T}}}{P_{\mathrm{I}}}$) and reflection ($R = \frac{P_{\mathrm{R}}}{P_{\mathrm{I}}}$) coefficient are determined.

$$T = \frac{1}{2}\left[\left(\frac{a}{d_{\mathrm{in}}} + 1\right) + \left(1 - \frac{a}{d_{\mathrm{in}}}\right)R\right]\left(M_{11}\mathrm{e}^{ikw} + M_{21}\right) + \frac{1}{2}\left[\left(\frac{a}{d_{\mathrm{in}}} + 1\right)R + \left(1 - \frac{a}{d_{\mathrm{in}}}\right)\right]\left(M_{12} + M_{22}\mathrm{e}^{-ikw}\right) \tag{A.32}$$

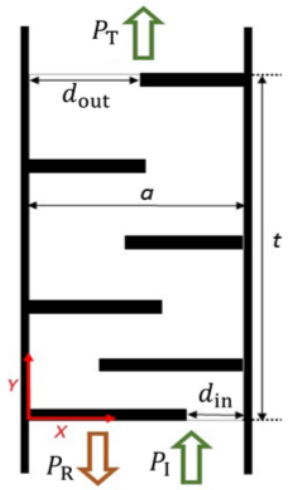

Figure A.2. Transmission and Reflection from Space-coiling metamaterial

$$R = \frac{\eta\left(\frac{a}{d_{in}} - 1\right) - \left(1 + \frac{a}{d_{in}}\right)}{\eta\left(\frac{a}{d_{in}} + 1\right) + \left(1 - \frac{a}{d_{in}}\right)} \tag{A.33}$$

In which η is defined as:

$$\eta = \frac{M_{12}\left(\frac{d_{out}}{a} - 1\right) - M_{22}e^{-ikw}\left(\frac{d_{out}}{a} + 1\right)}{M_{11}e^{ikw}\left(\frac{d_{out}}{a} - 1\right) - M_{21}\left(\frac{d_{out}}{a} + 1\right)} \tag{A.34}$$

In order to validate the analytical solution, the solution result has been compared with a numerical model of a single unit cell constructed using COMSOL Multiphysics software. The unit cell modeled herein, with background medium of air, features a channel width of d = 2cm and is composed of 20 coils (N = 20) with overall dimensions of 55 x 8.5 cm.

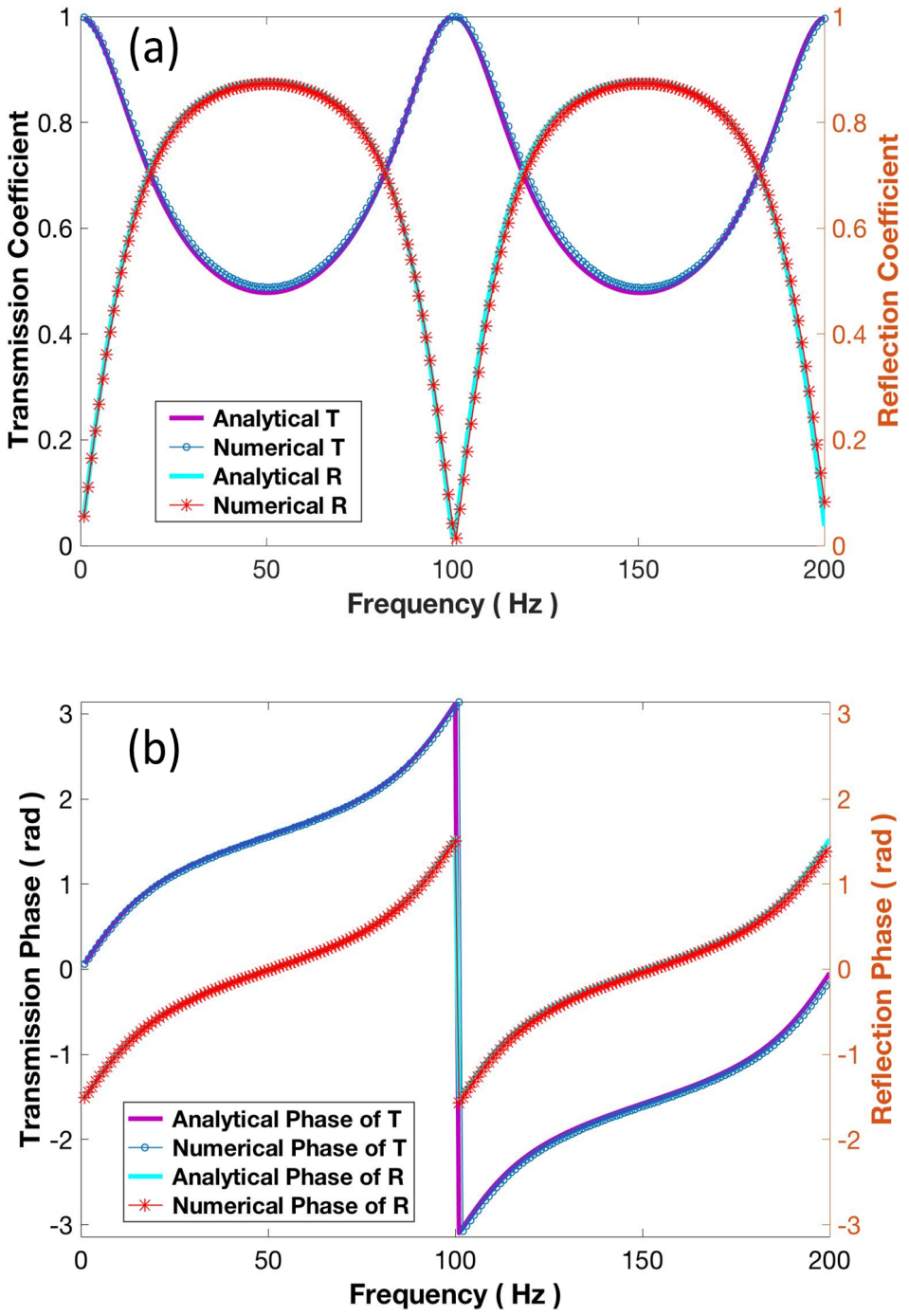

Figure A.3. Comparison between analytical and numerical transmission and reflection. (a) Transmission and reflection amplitude. (b) Transmission and reflection phase. The analytical-labeled legend refers to the results of the TMM methods and Numerical-labeled legends corresponds to the results obtained with simulation (COMSOL)

By sweeping the frequency, the resultant transmission and reflection amplitude and phase have been obtained using both numerical (COMSOL), and analytical models (TMM) discussed herein, with the results shown in **Figure A.3**. The results achieved using both the numerical and analytical approaches are in a high degree of agreement, thereby validating the applicability of the presented model for studying the space-coiling metamaterial behavior.

B. Effect of Unit cells' width on modulation efficiency

While phase-based wavefront modulation relies on an optimization procedure to tune the transmitted phase in each unit cell, full wave modulation (phase-amplitude) benefits from the use of the phase-conjugation method to tune the phase and amplitude of transmission at each unit cell. In full wave modulation, the complex transmission is obtained by discretizing the conjugated wave profile along the metasurface based on the width and the number of present unit cells. Consequently, for a given length of the metasurface, the unit cell's width is a critical design parameter, which can directly affect the conversion output. Smaller unit cell's widths provide a finer discretization and, consequently, near-ideal wavefront shaping capability. As an example, the sound focusing case discussed in this work has been considered, and the focusing performance for different values of unit cell width have been analyzed to yield insight into the effect of this key parameter. The sound focusing profile is shown in **Figure B.1** for four different values of unit cell width ranging from λ to λ/6 which clearly demonstrates that the unit cell's width plays a critical role in successful full wave modulation.

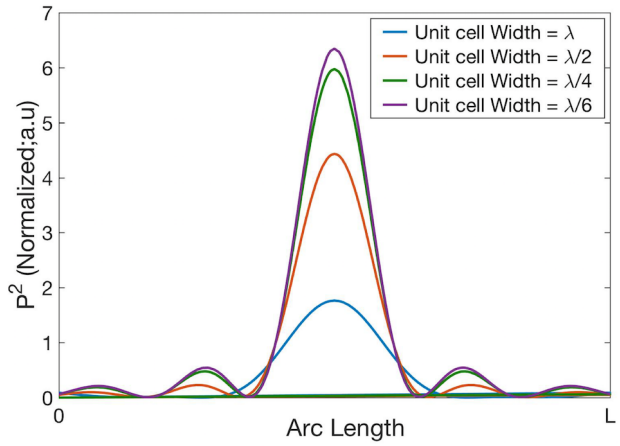

Figure B.1. Sound focusing lateral profile for unit cells of different widths.

C. Phase Modulation versus Phase/Amplitude modulation

While phase modulation represents a highly effective method for wavefront shaping, the additional degree of freedom afforded by full wave modulation (phase-amplitude) may yield improved performance and capability. As an illustrative example, in the case of acoustic beam splitting into $\pi/12$ and $-\pi/12$ directions, both phase modulation and phase-amplitude modulation have been considered. In both cases, a metasurface with a length of 5λ and composed of 30 unit cells has been assumed (vertical black line on the left side of **Figures C.1 (a)** and **C.1 (b).** In the case of phase modulation, given the desired directions of the split beams, the ideal phase at each unit cell has been obtained using the generalized Snell's law. Considering unity transmission amplitude along with the transmission phase found from the generalized Snell's law at each unit cell, the resulting waveform, representing the ideal case for phase modulation only, is shown in **Figure C.1 (a)**. For comparison, a similar metasurface has been considered for phase-amplitude modulation, in which using the phase-conjugation method, the ideal transmission phase and amplitude at each unit cell have been assigned with the resulting wavefront shown in **Figure C.1 (b)**. Comparing the results shown here, it may be readily observed that a markedly improved pressure uniformity is achieved using phase-amplitude modulation when compared to phase modulation. Using phase-amplitude modulation, a clear pressure resolution between the acoustic beams may be achieved, while such a clear pressure resolution has not been obtained with phase modulation.

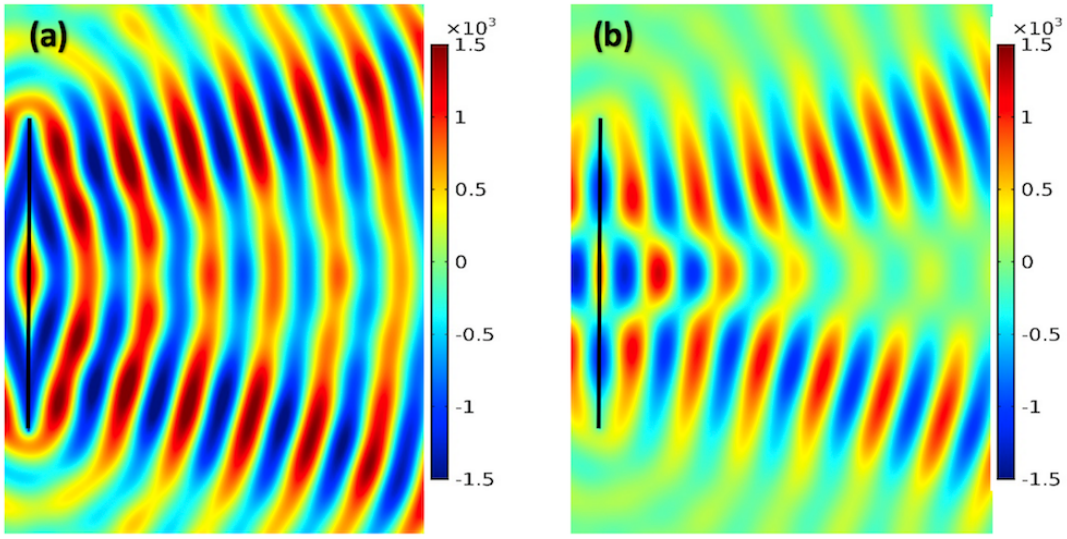

Figure C.1. Acoustic beam splitting. (a) Phase modulation. (b) Phase-amplitude modulation.

D. Unit cell's geometry and predicted complex transmission

Table D.1. Geometrical features and associated transmission in metasurface unit cells

Unit cell	Metasurface function	Geometrical parameters				Resultant transmission coefficient					
						T-Reversal		Numerical		Analytical	
		N	W (λ)	d_1 (λ)	CR	Amp	Phase (degree)	Amp	Phase (degree)	Amp	Phase (degree)
1	Focusing	2	0.124	0.064	1	0.72	107	0.68	108	0.75	114
	Beam-splitter	10	0.026	0.009	1.25	0.37	-116	0.36	-115	0.39	-115
2	Focusing	5	0.028	0.041	1.25	0.72	60	0.77	61	0.76	60
	Beam-splitter	16	0.013	0.004	1.18	0.32	-124	0.31	-124	0.34	-124
3	Focusing	6	0.022	0.034	1.23	0.73	12	0.75	12	0.77	12
	Beam-splitter	9	0.038	0.003	1.48	0.31	-145	0.31	-146	0.34	-148
4	Focusing	13	0.004	0.025	1.05	0.79	-31	0.8	-30	0.82	-34
	Beam-splitter	9	0.035	0.004	1.43	0.39	-168	0.38	-166	0.41	-171
5	Focusing	8	0.004	0.058	1	0.79	-68	0.72	-65	0.72	-74
	Beam-splitter	16	0.010	0.007	1.15	0.54	-178	0.58	-178	0.59	179
6	Focusing	9	0.003	0.050	1.01	0.71	-108	0.72	-108	0.71	-116
	Beam-splitter	10	0.016	0.017	1.18	0.70	180	0.71	-178	0.74	177
7	Focusing	9	0.013	0.020	1.16	0.73	-153	0.72	-157	0.71	-156
	Beam-splitter	10	0.015	0.023	1.13	0.81	-179	0.82	-175	0.84	177
8	Focusing	9	0.015	0.026	1.1	0.87	173	0.86	169	0.89	180
	Beam-splitter	10	0.015	0.023	1.13	0.83	-177	0.82	-175	0.84	177
9	Focusing	2	0.103	0.086	1.2	0.91	149	0.93	150	0.96	153
	Beam-splitter	10	0.016	0.017	1.18	0.73	-176	0.71	-176	0.74	179
10	Focusing	3	0.064	0.064	1.25	0.83	124	0.86	124	0.89	126
	Beam-splitter	16	0.010	0.006	1.18	0.52	180	0.50	180	0.51	180
11	Focusing	4	0.042	0.051	1.24	0.78	94	0.8	92	0.81	92
	Beam-splitter	16	0.010	0.004	1.23	0.27	156	0.34	156	0.35	161
12	Focusing	5	0.023	0.058	1.1	0.85	68	0.87	69	0.84	67
	Beam-splitter	14	0.013	0.007	1.18	0.28	77	0.28	78	0.28	81
13	Focusing	6	0.007	0.073	1.01	0.92	56	0.95	56	0.91	49
	Beam-splitter	14	0.006	0.020	1.08	0.57	52	0.60	50	0.62	52
14	Focusing	6	0.009	0.067	1.04	0.92	52	0.94	53	0.91	48
	Beam-splitter	8	0.012	0.058	1.00	0.83	47	0.79	46	0.84	47
15	Focusing	5	0.028	0.067	1	0.9	51	0.93	50	0.86	54
	Beam-splitter	2	0.001	0.117	1.40	0.97	45	1.00	48	1.00	49

E. Impedance Tube for Measuring Transmittance

Impedance Tube method represents one of the most classical methods to retrieve the acoustic properties of the different materials. In this method, the sample of the material is confined within an impedance tube containing the acoustic source on one end and arbitrary termination on another end. Subsequently, by probing the acoustic pressure in different locations of the impedance tube (both before and after the sample under test), acoustic properties may be retrieved by calculating the transmission and reflection of the sample.

Throughout the history, several approaches and methodology have been proposed to precisely calculate the transmission and reflection coefficient of the sample from which the equivalent acoustic properties of the sample such as Impedance and refractive index may be derived. Generally, the proposed method of measuring reflection and transmission using impedance tube can be divided into two main approaches, transfer matrix method (TM) and wave decomposition method (WD).

In the TM method, the sample material under test is considered as a transfer layer for which the transfer matrix relating the input pressure and velocity to the output pressure velocity may be obtained. Employing the resulted transfer matrix, which is independent of the tube termination condition, the transmission and reflection coefficient may be derived. The most notable TM method is the work by Bolton (Song et al., 2000; Olivieri et al., 2006) in which firstly, at 2000, the one-load method (One type of termination) for a symmetrical sample and later at 2006, the two-load method for asymmetric material were introduced. The TM methods proposed by Bolton, which were later adopted as ASTM standards, have shown to yield to the accurate and precise reflection and transmission coefficient results.

In the WD Methods, the efforts have been made to decompose the wave field (incoming and outgoing wave) both on upstream (Loudspeaker-sample) and downstream (sample-termination) of the impedance tube. Subsequently, the transmission and reflection coefficient of the sample may be obtained by the ratio of the transmitted and reflected wave to the incident wave, respectively. In 1977, Seybert (Seybert et al., 1977), proposed a method in which two microphones on the upstream and one microphone on the downstream were flush-mounted and the tube was terminated by the anechoic termination. Based on this configuration, he proposed a formulation to decompose the incident and reflected wave on the upstream using two microphones and derived the transmitted wave using the third microphone on the downstream. Despite the simplicity of the proposed WD method by Seybert, the challenge associated with the realization of the ideal anechoic termination, specifically in the low-frequency regime, has made this method not practical. To overcome this limitation, Chung and Blaser (Chung et al., 1980), proposed the implementation of two microphone one the downstream tube to incorporate the reflection of the wave from the non-ideal anechoic termination. However, in their proposed method, the effect of the multiple reflections in the impedance tube was neglected and subsequently failed to obtain the accurate values of the transmission and reflection coefficients. In 2011, Ho (Ho et al., 2005), proposed an improved WD method based on the four-microphone configuration that incorporates the effect of multi-reflection in both upstream and downstream tube. In the method proposed by Ho, two main assumptions have been taken in deriving the formulation; first, although the effect of multi-reflection has been considered in the downstream tube, anechoic/semi-anechoic termination was considered in the impedance

tube setup. This assumption has yielded to the small value of reflection from the termination in downstream and consequently has made the coupling between downstream and upstream tube negligible. Hence, the multi-reflection in the method proposed by Ho has been considered in upstream and downstream independent and isolated. Second, Ho only assumed the symmetrical sample in which the reflection coefficients of two sides of the sample were identical. Recently, Followed and based on the Ho's work, Salissou and Panneton (Salissou et al., 2009), present the general WD method arguing that even in the case of symmetrical sample, the reflection from two sides of the sample are not identical given the effect of the backed tube on the overall reflection. Subsequently, they present the two-load modification of Ho's method without limiting the method to the symmetrical sample.

The method presented by the Salissou may be criticized in its logic from two aspects. First, as correctly explained by Salissou, the reflection of each side of the sample is not only related to the sample. For instance, for the reflection coefficient considered from the sample's surface in the upstream side, the configuration of the downstream tube will also influence this reflection coefficient. Consequently, this method essentially fails to derive the reflection coefficient of the sample that only reflects the sample's acoustic property. Noteworthy, this issue is linked with consideration of the multi-reflection in upstream and downstream decoupled from each other. Moreover, due to implementation of two type of load, and consequently deviation from semi-anechoic termination condition in Ho's configuration, the logic of the Ho's method to neglect the higher order cross-coupling between upstream and downstream tube is no longer valid and needs to be

incorporated. In fact, in Salissou's method, the accuracy of the resulted transmission and reflection coefficient highly depends on the pair of the terminations used for the experiment. From this brief overview of the proposed impedance tube-based setup, it may be inferred that for not fully anechoic termination and not perfectly symmetrical sample, the only method that yields to the accurate transmission and reflection are TM-based method proposed by Bolton. For the general and practical cases, there is no accurate WD-based method that yields comparable precision of the TM method.

Herein, we have presented an Ultimate Wave Decomposition (UWD) method that regardless of the termination type, provides the same level of precision in the resulted transmission and reflection coefficient as Bolton's method for both symmetric and asymmetric sample. In UWD method, multi-reflection and infinite order of the cross-coupling between upstream and downstream tube are considered from which, first, the reflection coefficient solely associated with the sample under test and secondly, an accurate result regardless of the termination type may be obtained. The detail of the derivation and formulation of the UWD method will be discussed here.

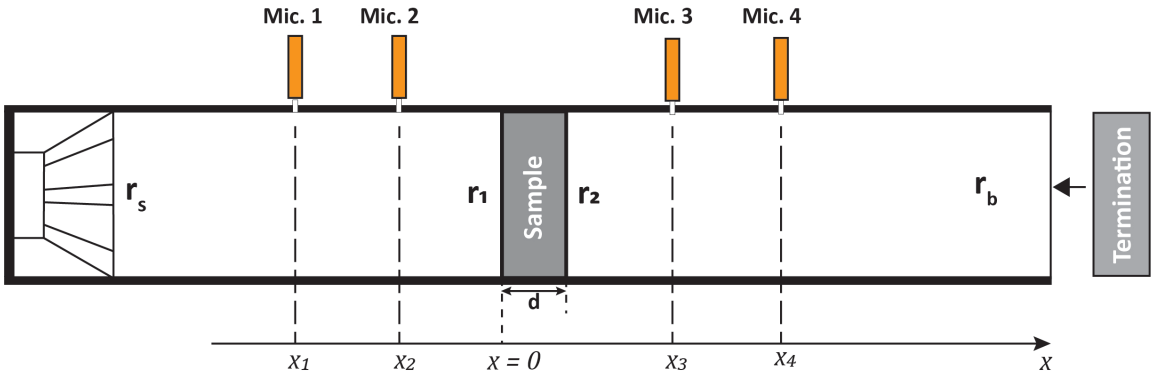

Figure E.1. Impedance tube setup with 4-microphones configuration

Let us initially derive the acoustic waves propagating in the positive x-direction in the upstream tube (**Figure E.1**). Assuming the load speaker is generating the signal with the amplitude of A, the wave field in the upstream propagating in the positive x-direction may be written as:

Zero-order wave:

$$P_0 = A \tag{E.1}$$

1st-order wave:

$$P_1 = Ar_1r_s + At^2r_s\sum_{n=0}^{n=\infty} r_b(r_br_2)^n \tag{E.2}$$

In which r_1, r_2, r_s, r_b, and t are reflection coefficient of the sample in the upstream, reflection coefficient of the sample in the downstream, reflection from the speaker, reflection from the end termination and transmission coefficient of the sample, respectively. Knowing that r_s, r_b are both smaller than the unity, equation (E.2) may be simplified to:

$$P_1 = Ar_1r_s + \frac{At^2r_br_s}{1-r_2r_b} = A(r_1r_s + \frac{t^2r_br_s}{1-r_2r_b}) \tag{E.3}$$

Similarly, 2nd-order wave may be obtained as:

$$P_2 = A(r_1r_s)^2 + A(\frac{t^2r_br_s}{1-r_2r_b})^2 + 2A(r_1r_s)(\frac{t^2r_br_s}{1-r_2r_b}) = A(r_1r_s + \frac{t^2r_br_s}{1-r_2r_b})^2 \tag{E.4}$$

Subsequently, the nth-order wave field may be written as:

$$P_n = A(r_1r_s + \frac{t^2r_br_s}{1-r_2r_b})^n \tag{E.5}$$

The total wave in upstream tube propagating in the positive x-direction may be obtained as:

$$P_{upstream+} = \frac{A}{1 - \frac{t^2 r_b r_s}{1 - r_2 r_b} - r_1 r_S} \tag{E.6}$$

Following the same approach, the wave field in the upstream propagating in the negative x-direction may be derived as:

Zero-order wave:

$$P_0 = A r_1 + \frac{A t^2 r_b}{1 - r_2 r_b} \tag{E.7}$$

1st-order wave:

$$P_1 = (A r_1 + \frac{A t^2 r_b}{1 - r_2 r_b})(r_1 r_s + \frac{t^2 r_b r_s}{1 - r_2 r_b}) \tag{E.8}$$

And the nth-order wavefield may be written as:

$$P_n = A(r_1 + \frac{t^2 r_b}{1 - r_2 r_b})(r_1 r_s + \frac{t^2 r_b r_s}{1 - r_2 r_b})^n \tag{E.9}$$

Eventually, the total wave in upstream tube propagating in the negative x-direction may be obtained as:

$$P_{upstream-} = \frac{A(r_1 + \frac{t^2 r_b}{1 - r_2 r_b})}{1 - \frac{t^2 r_b r_s}{1 - r_2 r_b} - r_1 r_S} \tag{E.10}$$

Consequently, the total acoustic field in the upstream tube following $j\omega t$ convention resulted as:

$$P_{Upstream} = \frac{A \cdot e^{-jkx} + A \cdot e^{jkx}(r_1 + \frac{t^2 r_b}{1 - r_2 r_b})}{1 - \frac{t^2 r_b r_s}{1 - r_2 r_b} - r_1 r_S} \tag{E.11}$$

Following the same approaches, the total wave field in the downstream may be derived as:

$$P_{Downstream} = \frac{\frac{Ate^{-jk(x-d)}}{1 - r_2 r_b} + \frac{Atr_b e^{jk(x-d)}}{1 - r_2 r_b}}{1 - \frac{t^2 r_b r_s}{1 - r_2 r_b} - r_1 r_S} \tag{E.12}$$

Reflection and Transmission in symmetrical Material

In this section, the material under the test is considered symmetric. In other word, r_1 and r_2 are identical. From the formulation discussed here and utilizing Transfer function approaches between the microphones, one may precisely calculate the reflection and transmission regardless of the termination type. The transfer function between two microphones is defined as the ratio between their readout in the frequency domain and has been commonly employed before in the impedance tube setup. Herein, we have utilized the combination of H_{12}, H_{32}, and H_{43} transfer functions which are defined as:

$$H_{12} = \frac{P_{Mic.1}}{P_{Mic.2}}; H_{32} = \frac{P_{Mic.3}}{P_{Mic.2}}; H_{43} = \frac{P_{Mic.4}}{P_{Mic.3}} \tag{E.13}$$

From H43, it may be inferred that:

$$H_{43} = \frac{P_{Mic.4}}{P_{Mic.3}} = \frac{e^{-jk(x_4-d)} + r_b e^{jk(x_4-d)}}{e^{-jk(x_3-d)} + r_b e^{jk(x_3-d)}} \tag{E.14}$$

$$r_b = \frac{e^{-jk(x_4-x_3)} - H_{43}}{H_{43} e^{2jk(x_3-d)} - e^{jk(x_3+x_4-2d)}} \tag{E.15}$$

Moreover, from H_{12} and H_{32}, it can be concluding that:

$$H_{12} = \frac{e^{jk(x_2-x_1)} + e^{jk(x_1+x_2)}[r + t^2 r_b(\frac{1}{1-rr_b})]}{1 + e^{2jkx_2}[r + t^2 r_b(\frac{1}{1-rr_b})]} \tag{E.16}$$

$$H_{32} = \frac{\frac{t}{1-rr_b}(e^{jk(x_2-x_3+d)} + r_b e^{jk(x_3+x_2-d)})}{1 + e^{2jkx_2}[r + t^2 r_b(\frac{1}{1-rr_b})]} \tag{E.17}$$

From equations (E.16) and (E.17), the only two unknowns, i.e., *r* and *t* may be derived as:

$$r = \frac{m - Qr_b}{1 - Qr_b^2} \tag{E.18}$$

$$t = \frac{(mH_{32}e^{2jkx_2} + H_{32})(1 - rr_b)}{(e^{jk(x_2-x_3+d)} + r_b e^{jk(x_2+x_3-d)})} \tag{E.19}$$

Where:

$$m = \frac{e^{jk(x_2-x_1)} - H_{12}}{e^{2jkx_2} H_{12} - e^{jk(x_1+x_2)}} \tag{E.20}$$

$$Q = \frac{(mH_{32}e^{2jkx_2} + H_{32})^2}{(e^{jk(x_2-x_3+d)} + r_b e^{jk(x_2+x_3-d)})^2} \tag{E.21}$$

Notably, due to the symmetrical assumption for the material under test, r_1 and r_2 are simply represented as r in the above equations.

Reflection and Transmission in asymmetrical Material

In the asymmetrical materials, with an added unknown due to the difference in reflection coefficient of the sample from each side, two different type of terminations may be utilized to provide a sufficient number of the equations to calculate the unknowns. This approach has been commonly utilized before and referred to as the two-load method. Using the two-load method and based on the UWD method discussed herein, transmission and reflection coefficients may be derived as below. Noteworthy, the star superscript denotes the parameters associated with the second type of termination. Similar to symmetrical material from H_{43} and $H_{43}*$, one may infer that:

$$r_b = \frac{e^{-jk(x_4-x_3)} - H_{43}}{H_{43}e^{2jk(x_3-d)} - e^{jk(x_3+x_4-2d)}} \tag{E.22}$$

$$r_b* = \frac{e^{-jk(x_4-x_3)} - H_{43}*}{H_{43}*e^{2jk(x_3-d)} - e^{jk(x_3+x_4-2d)}} \tag{E.23}$$

The transmission coefficient is resulted as:

$$t = \frac{r_b - r_b*}{r_b\Upsilon* - r_b*\Upsilon} \tag{E.24}$$

Where:

$$\Upsilon = \frac{(e^{jk(x_2-x_3+d)} + r_b e^{jk(x_2+x_3-d)})}{(mH_{32}e^{2jkx_2} + H_{32})} \tag{E.25}$$

$$\Upsilon^* = \frac{(e^{jk(x_2-x_3+d)} + r_b * e^{jk(x_2+x_3-d)})}{(m * H_{32} * e^{2jkx_2} + H_{32}^*)} \tag{E.26}$$

In which m and m* may be derived using equation (E.20) with H12 and H12* are being used respectively for m and m*. Eventually, reflection coefficients may be derived as:

$$r_2 = \frac{1}{r_b} - \frac{t(e^{jk(x_2-x_3+d)} + r_b e^{jk(x_2+x_3-d)})}{r_b(mH_{32}e^{2jkx_2} + H_{32})} \tag{E.27}$$

$$r_1 = m - t^2 r_b(\frac{1}{1-r_2 r_b}) \tag{E.28}$$

From the methodology discussed herein, i. e., UWD method one may easily calculate the precise reflection and transmission coefficient regardless of the termination type used in the impedance tube setup. The symmetrical sample with just single termination and asymmetrical sample with two types of termination may be fully characterized in the presented methodology. Next, the performance of UWD method for both symmetrical and asymmetrical sample has been experimentally validated and compared with the available approaches.

Experimental Validation for Symmetrical Sample using one-load Method

In order to experimentally validate the performance of the UWD to characterize the symmetrical material, impedance tube setup has been implemented to measure the transfer functions. The symmetrical sample assumed herein is an orifice fabricated out of 3.2mm thickness aluminum sheet with the outer diameter of the 15cm and inner diameter of 2cm.

The fabricated orifice has been placed inside the impedance tube, and transfer functions H12, H32, and H43 have been measured in the range of 950Hz–1250 Hz. In this experiment, three different types of termination have been employed to investigate the effect of termination on the resulted transmission and reflection. The open-end termination refers to the case when the end of the impedance tube has been left open. For rigid termination, the impedance tube is terminated with a 3.2mm thickness aluminum sheet that has been used to mimics the rigid end. The semi-anechoic termination considered herein is the 5cm thickness absorbing foam backed by the aluminum sheet, and the results for each termination are shown in **Figure E.2, E.3, and E.4**. In these figures, results based on our method, i.e., UWD are shown with a solid red line. Results using the modified wave decomposition method (MWD) based on Ho's work (Ho et al., 2005) are shown with a black dotted line. Moreover, the results based on the Transfer Matrix approach based on Bolton's methods (Olivieri et al., 2006) are shown with a black dashed line.

From the results shown in **Figure E.2 to E.4**, it may be observed that transmission amplitude may be precisely obtained using UWD and TM method regardless of the termination type. However, transmission amplitude derived using Ho's method demonstrates instability and multiple deviations from the exact results. This variation is found more significant in the case of rigid termination and slightly improved in the case of semi-anechoic termination. Similarly, the transmission phase may be precisely calculated using the UWD and TM method but not with the MWD approach. In fact, we believe that the MWD method based on Ho's work may possess a typo in the published work, which has led to this large discrepancy.

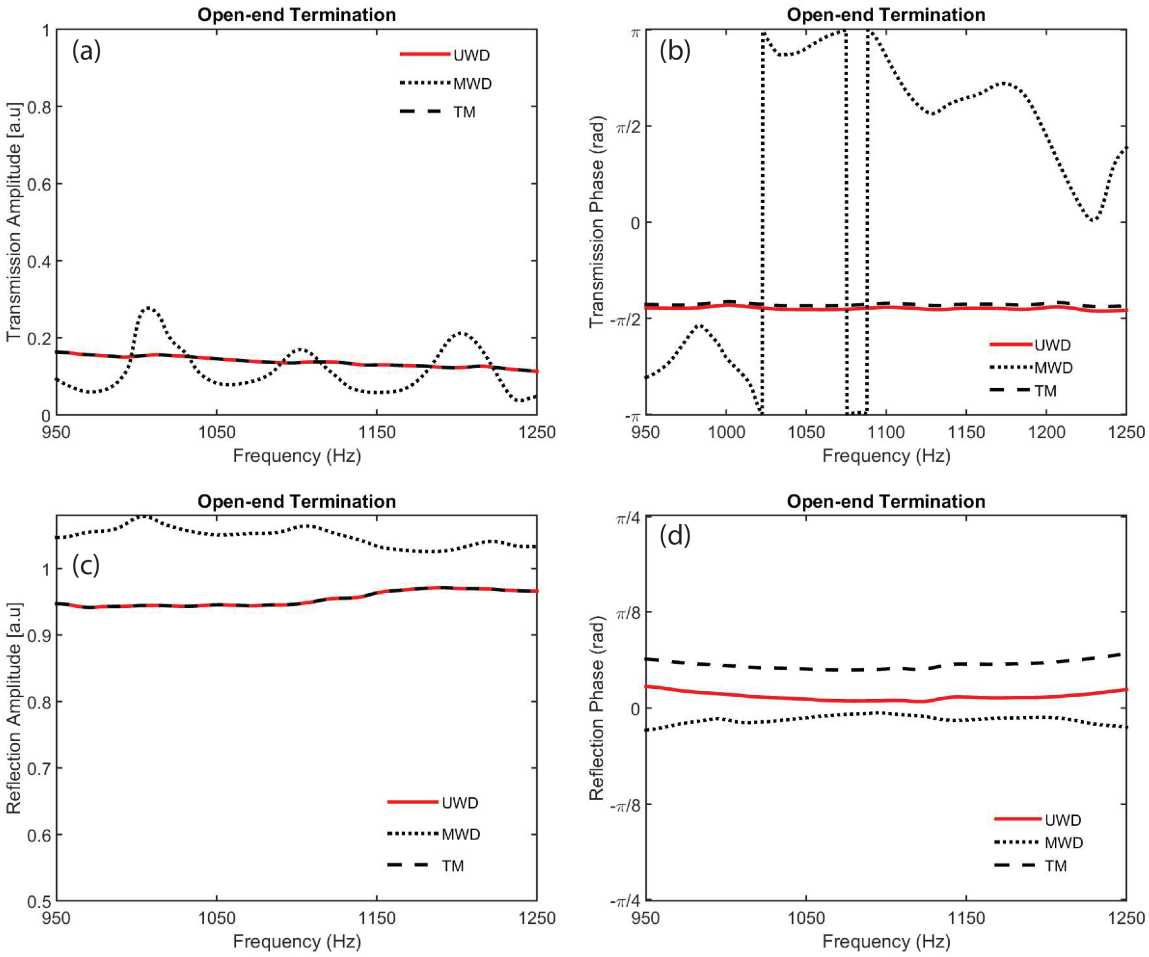

Figure E.2. Transmission and reflection amplitude and phase for the case of open termination. Results based on our method, i.e., UWD are shown with a solid red line. Results using the modified wave decomposition method (MWD) based on Ho's work (Ho et al., 2005) are shown with a black dotted line. Moreover, the results based on the Transfer Matrix approach based on Bolton's methods (Olivieri et al., 2006) are shown with a black dashed line. (a) Transmission amplitude. (b) Transmission phase. (c) Reflection amplitude. (d) Reflection phase.

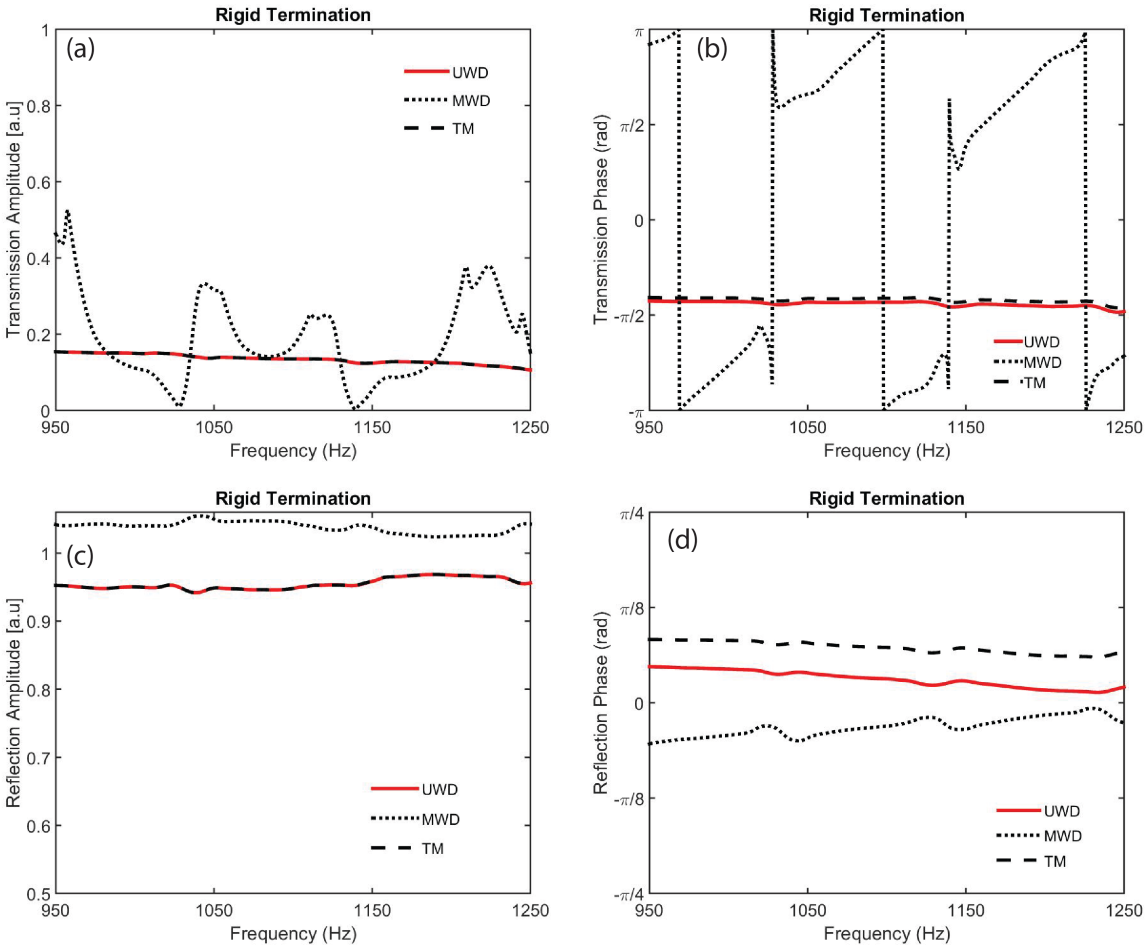

Figure E.3. Transmission and reflection amplitude and phase for the case of rigid termination. Results based on our method, i.e., UWD are shown with a solid red line. Results using the modified wave decomposition method (MWD) based on Ho's work (Ho et al., 2005) are shown with a black dotted line. Moreover, the results based on the Transfer Matrix approach based on Bolton's methods (Olivieri et al., 2006) are shown with a black dashed line. (a) Transmission amplitude. (b) Transmission phase. (c) Reflection amplitude. (d) Reflection phase.

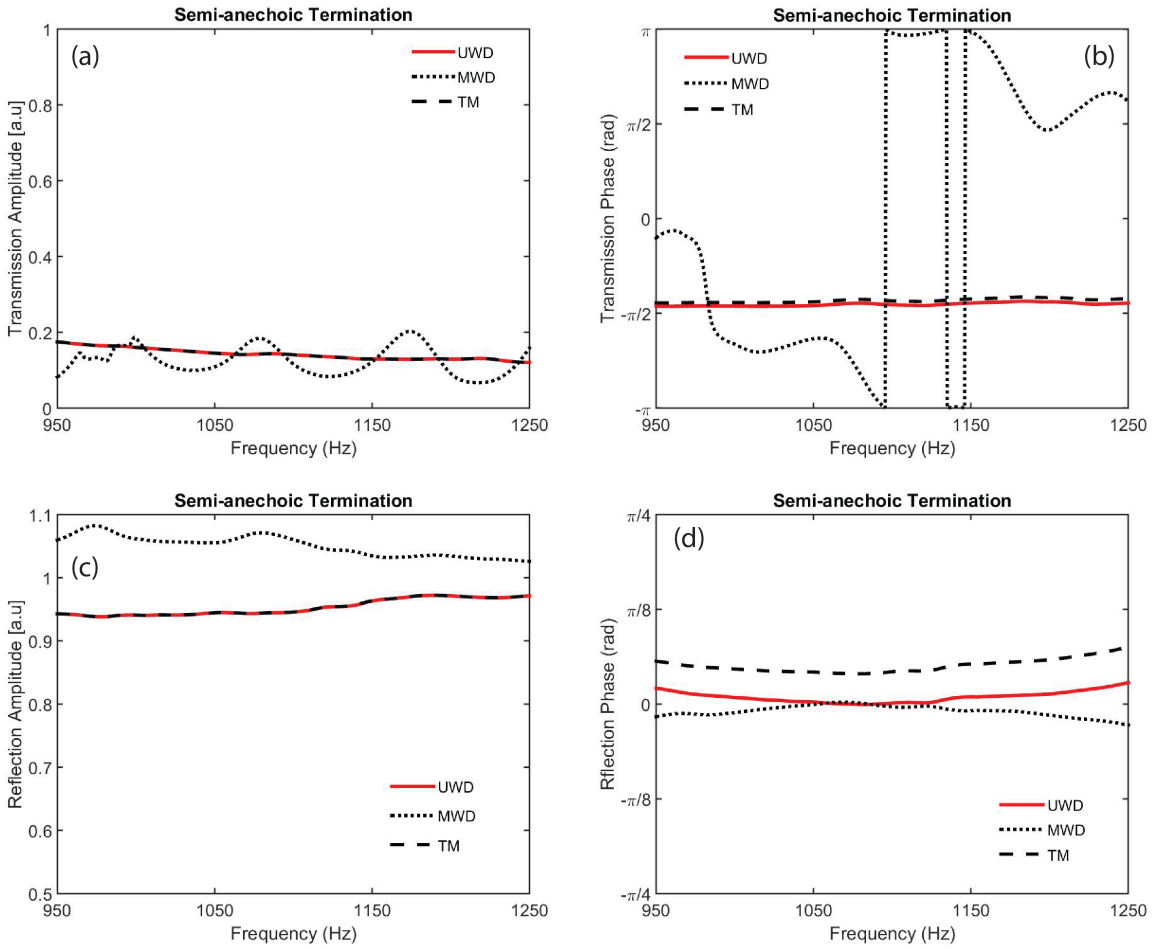

Figure E.4. Transmission and reflection amplitude and phase for the case of semi-anechoic termination. Results based on our method, i.e., UWD are shown with a solid red line. Results using the modified wave decomposition method (MWD) based on Ho's work (Ho et al., 2005) are shown with a black dotted line. Moreover, the results based on the Transfer Matrix approach based on Bolton's methods (Olivieri et al., 2006) are shown with a black dashed line. (a) Transmission amplitude. (b) Transmission phase. (c) Reflection amplitude. (d) Reflection phase.

In the case of reflection coefficients, as discussed before, in the MWD method, the reflection coefficient may be affected by the backed tubing, and consequently, the resulted reflection is not physically meaningful. However, employing both UWD and TM method, reflection amplitude, and phase may be precisely obtained regardless of the termination type. Noteworthy, there exist a minor difference between the reflection phase derived using

UWD and TM method. This difference has resulted from the assigned value for the air density in the TM method. The value of the air density in the TM method is considered 1.18 (kg/m3) that corresponds to the air density at room temperature (25-degrees C). With the change in the temperature, the air density may slightly change, and the UWD method that does not need the value of air density may provide a more accurate result. From the results shown here, it may be observed that both UWD and TM method provides reliable methodologies to accurately retrieve the complex transmission and reflection for symmetrical material using one-load impedance tube setup. Moreover, it is pointed out herein that given the fact that the UWD method, known air density value is not required, it may lead to the more accurate results by the elimination of this potential source of error. Notably, the method presented by Salissou and Panneton (Salissou et al., 2009), based on the Ho's work, requires two-load even for a case of symmetrical sample and consequently has not been discussed here.

Experimental Validation for Asymmetrical Sample using two-load Method

In order to experimentally validate the performance of UWD for the case of asymmetrical material, the combination of the orifice and macro-perforated plates (MPP) has been tested in the impedance tube setup. The asymmetrical sample herein is composed of the orifice placed in the vicinity of MPP with the 2cm spacing between them. The orifice is composed of the aluminum sheet with the thickness of the 3.2 mm with the outer diameter of the 15 cm and inner diameter of 2 cm. The MPP is fabricated out of the aluminum sheet with a thickness of 3.2 mm containing holes with the diameter of 2mm, and the overall area

porosity of the MPP is 0.02. Due to the significant difference in the acoustic behavior of orifice and the proposed MPP, the proposed configuration herein, i.e. (orifice/gap/MPP) represents a highly asymmetric acoustical material.

The fabricated asymmetrical sample has been tested using impedance tube setup, and the associated transfer functions (H_{12}, H_{32}, H_{43}) have been measured between 950-1250 Hz. In this experiment, given the non-symmetrical nature of the sample under test, two different types of termination (i.e., two-load method) are required. Therefore, in order to characterize the material and investigate the effect of the termination, experiments have been performed using all three different types of the termination discussed before (open, rigid, and semi-anechoic). Subsequently, employing the results obtained associated with any pair of the three termination type, the transmission and reflections may be calculated.

Shown in **Figure E.5**, transmission, and reflections phase and amplitude have been derived using open termination and rigid termination cases using three different methods. UWD, the method presented herein is shown with a solid red line. Generalized wave decomposition (GWD), based on the work by Salissou and Panneton (Salissou et al., 2009), is shown with a black dotted line and the TM method based on Bolton's work (Olivieri et al., 2006) is shown with a black dashed line. Noteworthy Ho's method is only limited to the symmetrical material, and it is not discussed here.

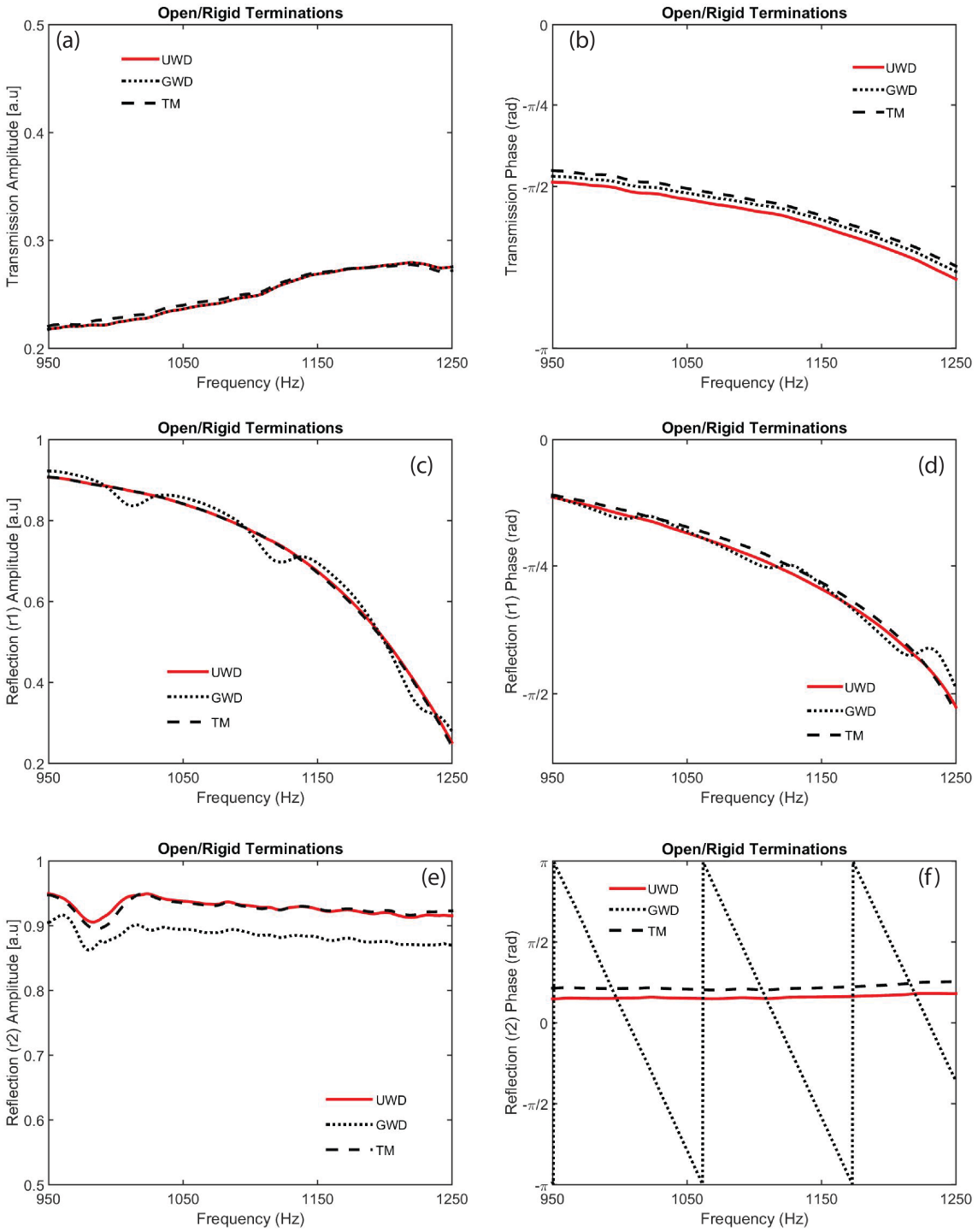

Figure E.5. Transmission and reflection for asymmetrical material. (a) Transmission amplitude. (b) Transmission phase. (c) Reflection (r_1) amplitude. (d) Reflection (r_1) phase. (e) Reflection (r_2) amplitude. (f) Reflection (r_2) phase.

From the result obtained herein and shown in **Figure E.5**, it may be inferred that all three methods investigated herein, i.e., UWD, GWD, and TM methods are capable of precisely retrieving the transmission phase and amplitude. With regards to the reflection coefficients, UWD and TM methods both yield precise results with only minimal difference in their resulted phase, which was pointed out to be associated with the uncertainty in the value of the air density required for TM method and has been discussed before. Furthermore, it may be concluded that the reflection coefficients obtained by the GWD method lack the precision of the UWD and TM method. For reflection coefficient (r_1) given the fact that two different types of terminations are utilized, the effect of downstream tubing on the calculated reflection by the GWD method is mitigated but yet possesses a random deviation from the accurate value. In the case of r_2, the resulted reflection amplitude is shown to be slightly drifted from the accurate value, but the reflection phase possesses a significant difference with the expected result. The deviation in amplitude and phase of r_1 and r_2 calculated using GWD method is believed to be present due to neglecting the cross-coupling between upstream and downstream tube in the methodology proposed by Salissou and Panneton (Salissou et al., 2009). From the results shown in **Figure E.5**, it may be concluded that the in the case of the asymmetrical sample, and employing two types of termination, both UWD and TM methods may be leveraged to retrieve the precise value of reflection and transmission. However, the GWD method is found applicable only to retrieve the transmission but not reflection.

The results discussed herein and shown in **Figure E.5**, are derived using open-end and rigid-end terminations. In order to investigate the dependency of these methodologies

on the termination type, the maximum variation in transmission and reflection's phase and amplitude have been calculated when different pair of termination is utilized. The results are shown in Figure E.6 for three different methods.

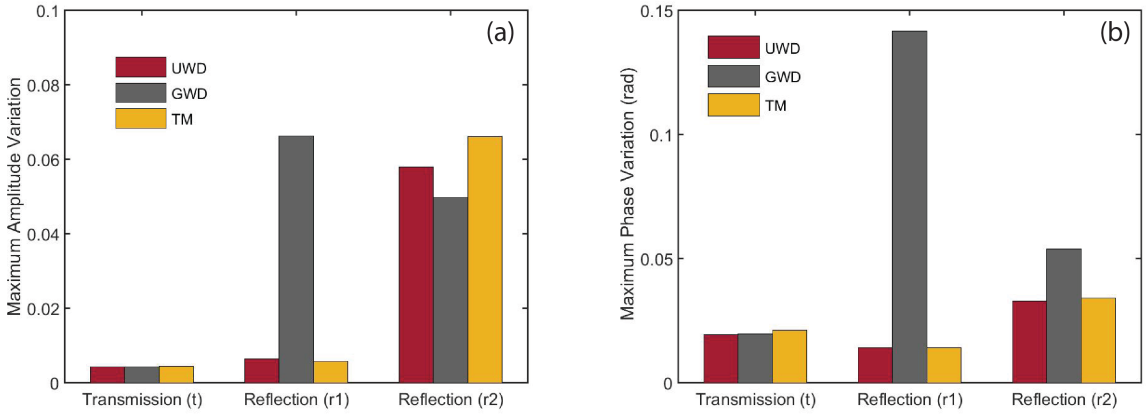

Figure E.6. Maximum variation in the calculated amplitude and phase when a different pair of termination is employed. (a) Amplitude variation. (b) Phase variation.

From **Figure E.6**, it may be observed that regardless of the set of terminations used for the two-load method, UWD and TM methods both offer the same level of precision in the resulted transmission and reflection phase and amplitude. GWD method is a reliable method for measuring the transmission, but the resulted reflection is more termination dependent and inaccurate.

BIBLIOGRAPHY

Alfredson, R. J., Davies, A. L. "The radiation of sound from an engine exhaust". Journal of Sound and Vibration. 13(4), 389-408 (1970).

Ardekany, A. N., Daneshmand, F. and Mehrvarz, A. "Vibration Analysis of a Micropolar Membrane in Contact with Fluid". Iranian Journal of Science and Technology – Transactions of Mechanical Engineering, 1-10 (2018).

Aristegui C., Angle YC. "Effective mass density and stiffness derived from P-wave multiple scattering". Wave Motion. 44,153-164 (2007).

ASTM Standard No. E2611-09, "Standard test method for measurement of normal incidence sound transmission of acoustical materials based on the transfer matrix method" (ASTM International, West Conshohocken, PA, 2009).

Bok, E., Park, J. J., Choi, H., Han, C. K., Wright, O. B. and Lee, S. H. "Metasurface for Water-to-Air Sound Transmission". Physical Review Letters. 120, 044302 (2018).

Brunet, T., Merlin, A., Mascaro, B., Zimny, K., Leng, J., Poncelet, O., Aristegui, C., Mondain-Monval, O. "Soft 3D acoustic metamaterial with a negative index". Nature Materials. 14:384-388 (2015).

Carcione, J. M., Cavallini, F. "On the acoustic-electromagnetic analogy". Wave Motion. 21,149-162 (1995).

Cervera, F., Sanchis, L., Sánchez-Pérez, J., Martínez-Sala, R., Rubio, C., Meseguer, F., López, C., Caballero, D., Sánchez-Dehesa, J. "Refractive acoustic devices for airborne sound". Physical Review Letters. 88 (2), 023902 (2002).

Chen, H. & Chan, C. T. "Acoustic cloaking in three dimensions using acoustic metamaterials". Applied Physics Letters. 91(18), 183518 (2007).

Chen, Y., Huang, G., Zhao, X., Hu, G., Sun, C. T. "Analytical coupled vibroacoustic modeling of Membrane-type acoustic metamaterials: plate model". Journal of the Acoustical Society of America. 136(6), 2926-2934 (2014).

Chen, Z., Fan, L., Zhang, S. Y., Zhang, H., Li, X. J., Ding, J. "An open-structure sound insulator against low-frequency and wide-band acoustic waves". Applied Physics Express. 8(10), 107301 (2015).

Cheng, Z. Y. and Martin, B. G. "Symmetric multilayer structures and their use in the design and fabrication of Chebyshev acoustic antireflection coatings". Journal of the Acoustical Society of America. 90,385 (1991).

Chung, J. Y. and Blaser, D. A. "Transfer function method of measuring induct acoustic properties. II. Experiment," Journal of the Acoustical Society of America. 68, 914–921 (1980).

Crandall, I. B. "Theory of vibrating systems and sound". D. Van Nostrand Company. 1954.

Cummer, S. A., Popa, B. I., Schurig, D., Smith, D. R., Pendry, J., Rahm, M., Starr, A. "Scattering theory derivation of a 3D acoustic cloaking shell". Physical Review Letters. 100(2), 024301 (2008).

Esfahlani, H., Lissek, H. "Generation of acoustic helical wavefronts using metasurfaces". Physical Review B. 95(2), 024312(2017).

Estakhri, N. M., Alù, A. "Wave-front transformation with gradient metasurfaces". Physical Review X. 6, 041008 (2016).

Fano, U. "Effects of configuration interaction on intensities and phase shifts". Physical Review. 124(6), 1866-1878 (1961).

Fellay, A., Gagel, F., Maschke, K. "Scattering of vibrational wave in perturbed quasi-one-dimensional multichannel waveguides". Physical Review B. 55(3), 1707-1717 (1997).

Feng, Q., Huang, Z., Yu, G., Meng, X. "Acoustic attenuation performance through a constricted duct improved by an annular resonator". Journal of the Acoustical Society of America. 134(4), 345-351 (2013).

Fink, M. "Acoustic metamaterial: nearly perfect sound absorbers". Nature Materials. 13(9):848-849 (2014).

Fol, L., Zhang, X. "Negative acoustic index metamaterial". Physical Review B. 83(21), 214304(8) (2011).

Frenzel, T., Brehm, J. D., Bückmann, T., Schittny, R., Kadic, M., Wegener, M. "Three-dimensional labyrinthine acoustic metamaterials". Applied Physics Letters. 103(6), 061907 (2013).

Fry, F. J., Barger, J. E. "Acoustical properties of the human skull". Journal of the Acoustical Society of America. 63(5):1576-1590 (1978).

García-Chocano, V. M., Cabrera, S., Sanchez-Dehesa, J. "Broadband sound absorption by lattices of microperforated cylindrical shells". Applied Physics Letters. 101(18), 184101 (2012).

Gerstenmayer, M., Fellah, B., Magnin, R., Selingue, E., Larrat, B. "Acoustic Transmission Factor through the Rat Skull as a Function of Body Mass, Frequency and Position". Ultrasound in Medicine & Biology. 44(11), 2336-2344 (2018).

Ghaffarivardavagh, R., Nikolajczyk, J., Anderson, S., & Zhang, X. "Ultra-open acoustic metamaterial silencer based on Fano-like interference". Physical Review B. 99(2), 024302 (2019).

Ghaffarivardavagh, R., Anderson, S., & Zhang, X. "Double-decorated membrane structure: Initial efforts towards real-time phase modulation". Journal of the Acoustical Society of America. 142(4), 2578-2578 (2017).

Ghaffarivardavagh, R., Xu, R., Anderson, S., & Zhang, X. "Ultimate wave decomposition method for characterization of symmetric and asymmetric materials". Journal of the Acoustical Society of America. 145(3), 1896-1896 (2019).

Ghaffarivardavagh, R., Nikolajczyk, J., Holt, R. G., Anderson, S., Zhang, X. "Horn-like space-coiling metamaterials toward simultaneous phase and amplitude modulation". Nature Communications. 9, 1349(2018).

Goffaux, C., Sanchez-Dehesa, J., Yevati, A. L. "Evidence of Fano-like interference phenomena in locally resonant materials". Physical Review Letters. 88(22), 225502 (2002).

He, Z., Cai, F., Ding, Y., Liu, Z. "Subwavelength imaging of acoustic waves by a canalization mechanism in a two-dimensional phononic crystal". Applied Physics Letters. 93:233503 (2008).

Ho K. M., Yang Z., Zhang X. X., and Sheng, P. "Measurement of sound transmission through panels of locally resonant materials between impedance tubes," Applied Acoustics. 66, 751–765 (2005).

Huang, L. "Broadband sound reflection by plates covering side-branch cavities in a duct". Journal of the Acoustical Society of America. 119, 2628–2638 (2006).

Jung, J. W., Kim, J. E., Lee, J. W. "Acoustic metamaterial panel for both fluid passage and broadband soundproofing in the audible frequency range". Applied Physics Letters. 112(4), 041903 (2018).

Khodaei, M. J., Mehrvarz, A., Candelino, N. and Jalili, N. "Theoretical and Experimental Analysis of Coupled Flexural-Torsional Vibrations of Rotating Beams". ASME, Dynamic Systems and Control Conference. V003T42A004-V003T42A004 (2018)

Kim, S. H. and Lee, S. H. "Air transparent soundproof window". AIP Advances. 4(11), 117123 (2014).

Kushibiki, J. and Chubachi, N. “Double-layer acoustic antireflection coating for sapphire/water interface”. Electronics Letters. 17(2), 59-61 (1981).

Langfeldt, F., Riecken, J., Gleine, W., Von Estorff, O. “A membrane-type acoustic metamaterial with adjustable acoustic properties”. Journal of Sound and Vibration. 373, 1-18(2016).

Lauche, G. C., MacGilliarvy, J. R., Swanson. D. C. “Active control of axial-flow fan noise”. Journal of the Acoustical Society of America. 101, 341–349 (1997).

Lee, J. W., Jang, G. W. “Topology design of reactive mufflers for enhancing their acoustic attenuation performance and flow characteristics simultaneously”. International Journal for Numerical Methods in Engineering. 91, 552–570 (2012).

Li, L. J. Zheng, B., Zhong, L. M., Yang, J., Liang, B., Chen, J. C. “Broadband compact acoustic absorber with high-efficiency ventilation performance". Applied Physics Letters. 113, 103501 (2018).

Li, P., Chen, X., Zhau, X., Hu, G., Xiang, P. “Acoustic cloak constructed with thin-plate metamaterials”. International Journal of Smart and Nano Materials. 6(1):73-83 (2015).

Li, Y., Jiang, X., Li, R. Q., Liang, B., Zou, X. Y., Yin, L. L., Cheng, J. C. “Experimental realization of full control of reflected waves with subwavelength acoustic metasurfaces”. Physical Review Applied. 2, 064002 (2014).

Li, Y., Jiang, X., Liang, B., Cheng, J. J., Zhang, L. “Metascreen-based acoustic passive phased array”. Physical Review Applied. 4, 024003 (2015).

Li, Y., Liang, B., Gu, Z. M., Zho, X. Y., Cheng, J. C. “Unidirectional acoustic transmission through a prism with near-zero refractive index”. Applied Physics Letters. 103(5), 053505 (2013).

Li, Y., Liang, B., Gu, Z. M., Zou, X. Y., Cheng, J. C. “Reflected wavefront manipulation based on ultrathin planar acoustic metasurfaces”. Scientific Reports. 3, 2546 (2013).

Li, Y., Liang, B., Tao, X., Zhu, X. F., Zou, X. Y., Cheng, J. C.” Acoustic focusing by coiling up space”. Applied Physics Letters. 101(23), 233508 (2012).

Li, Y., Liang, B., Zho, X. Y., Cheng, J. C. “Extraordinary acoustic transmission through ultrathin acoustic metamaterials by coiling up space”. Applied Physics Letters. 103(6), 063509 (2013).

Li, Y., Yu, G., Liang, B., Zou, X., Li, G., Cheng, S., Cheng, J. “Three-dimensional ultrathin planar lenses by acoustic metamaterials”. Scientific Reports. 4, 6830 (2014).

Liang, B., Yoan, B., Cheng, J. C. "Acoustic diode: rectification of acoustic energy flux in one-dimensional systems". Physical Review Letters. 103(10), 104301 (2009).

Liang, Z., Feng, T., Lok, S., Liu, F., Ng, K. B., Chan, C. H., Wang, J., Han, S., Lee, S., Li, J. "Space-coiling metamaterials with double negativity and conical dispersion". Scientific Reports. 3, 1614 (2013).

Liang, Z., Li, J. "Extreme acoustic metamaterial by coiling up space". Physical Review Letters. 108(11), 114301 (2012).

Liu, L., Zhang, X., Kenney, M., Su, X., Xu, N., Ouyang, C., Shi, Y., Han, J., Zhang, W., Zhang, S. "Broadband metasurfaces with simultaneous control of phase and amplitude". Advanced Materials. 26(29), 5031-5036 (2014).

Lu, D. and Liu, Z. "Hyperlenses and metalenses for far-field super-resolution imaging". Nature Communications. 3, 1205 (2012).

Ma, G., Yang, M., Yang, Z., Sheng, P. "Low frequency narrow-band acoustic filter with large orifice". Applied Physics Letters. 103(1), 011903 (2013).

Martin, B. G. "A Note on Multilayer Acoustic Antireflection Coatings". Research in Nondestructive Evaluation. 4(1), (1992).

Mehrvarz, A., Khodaei, M. J., Clark, W. and Jalili, N."Modeling and Dynamics Analysis of a Beam-Hoverboard Self-Transportation System". ASME. Dynamic Systems and Control Conference, V003T32A008-V003T32A008 (2018).

Mehrvarz, A., Ardekany, A. N., Khodaei, M.J. and Jalili, N. "Vibration analysis and control of fluid containers using piezoelectrically-excited side wall". Journal of Vibration and Control, 25(7), 1393-1408 (2019).

Mei, J., Ma, G., Yang, M., Yang, J., Sheng, P. "Acoustic Metamaterials and Phononic Crystals". Springer, Berlin Heidelberg. (2013).

Mei, J., Ma, G., Yang, M., Yang, Z., Wen, W., Sheng, P. "Dark acoustic metamaterials as super absorbers for low-frequency sound". Nature Communications. 3,756 (2012).

Mei, J., Wu, Y. "Controllable transmission and total reflection through an impedance-matched acoustic metasurface". New Journal of Physics. 16, 123007 (2014).

Molerón, M., Daraio, C. "Acoustic metamaterial for subwavelength edge detection". Nature Communications. 6, 8037 (2015).

Monticone, F., Estakhri, N. M., Alù, A. "Full control of nanoscale optical transmission with a composite Metascreen". Physical Review Letters. 110(20), 203903 (2013).

Naify, C. J. Chang, C. M. McKnight, G. Nutt, S. "Transmission loss and dynamic response of membrane-type locally resonant acoustic metamaterials", Journal of Applied Physics. 108, 114905, (2010).

Ni, X., Kildishev, A. V., Shalaev, V. M. "Metasurface holograms for visible light". Nature Communications. 4, 2807 (2013).

Niu, Y., Kim, Y. J. "Three-dimensional visualizations of open fan noise field". Noise Control Engineering Journal. 60(4), 392-404 (2012).

Olivieri, O., Bolton, J. S. and Yoo, T. "Measurement of transmission loss of materials using a standing wave tube," Proceedings of Inter-Noise 2006, Honolulu, HI, 2006.

Pendry, J. B., Holden, A. J., Robbins, D. J., Stewart W. J. "Magnetism from conductors and enhanced nonlinear phenomena." IEEE Transactions on Microwave Theory and Techniques. 47, 2075–2084 (1999).

Pierce, A. D. "Acoustics: An introduction to its physical principles and applications", Acoustical Society of America, 1989.

Pinton, G., Aubry, J. F., Bossy, E., Muller, M., Pernot, M., Tanter, M. "Attenuation, scattering, and absorption of ultrasound in the skull bone". Medical Physics. 39(1), 299-307 (2012).

Rahman, A., Ashraf, A., Xin, H., Tong, X., Sutter, P., Eisaman, M., Black, C." Sub-50-nm self-assembled nano-textures for enhanced broadband antireflection in silicon solar cells". Nature Communications. 6:5963 (2015).

Rayleigh, L. "On reflection of vibrations at the confines of two media between which the transition is gradual". Proceedings of the London Mathematical Society. 1:51–56 (1879).

Sainidou, R. and Stefanou, N. "Guided and quasiguided elastic waves in phononic crystal slabs". Physical Review B. 73, 184301 (2006).

Salissou, Y. and Panneton, R. "A general wave decomposition formula for the measurement of normal incidence sound transmission loss in impedance tube," Journal of the Acoustical Society of America. 125, 2083–2090 (2009).

Scheuer, J. "Metasurfaces-Based holography and beam shaping: engineering the phase profile of light". Nanophotonics. 6(1), 137-152 (2016).

Schurig, D., Mock, J. J., Justice, B. J., Cummer, S. A., Pendry, J. B., Starr, A. F., Smith, D. R. "Metamaterial electromagnetic cloak at microwave frequencies". Science. 314(5801), 977-980 (2006).

Selamet, A., Ji, Z. L. "Acoustic attenuation performance of circular expansion chambers with extended inlet/outlet". Journal of Sound and Vibration. 223(2), 197–212 (1999).

Sellen, N., Cuesta, M., Galland, M. A. "Noise reduction in a flow duct: Implementation of a hybrid passive/active solution". Journal of Sound and Vibration. 297(3), 492-511 (2006).

Seybert, F. and Ross, D. F., "Experimental determination of acoustic properties using a two-microphone random-excitation technique," Journal of the Acoustical Society of America. 61, 1362–1370 (1977).

Shen, C., Xu, J., Fang, N. X., Jing, Y. "Anisotropic complementary acoustic metamaterial for canceling out aberrant layers". Physical Review X. 4(4), 041033 (2014).

Smith, D. R., Pendry, J. B., Wiltshire, M. C. "Metamaterials and negative refractive index". Science. 305(5685), 788-792 (2004).

Song, B. H. and Bolton, J. S. "A transfer matrix approach for estimating the characteristic impedance and wave numbers of limp and rigid porous materials," Journal of the Acoustical Society of America. 107, 1131–1152 (2000).

Song, Y. S., Huang, B., Dong, H. Y., Cheng, Q., Cui, T. J. "Broadband focusing acoustic lens based on fractal metamaterials". Scientific Reports. 6, 35929 (2016).

Stewart, G. W. "The theory of the Herschel-Quincke tube". Physical Review. 31(4), 696-698 (1928).

Su, H., Zhao, X., Xu, X., Hu, G. "Experimental study on acoustic subwavelength imaging of holey-structured metamaterials by resonant tunneling". Journal of the Acoustical Society of America. 135(4), 1686-1691 (2014).

Sun, H. T., Wang, J. S., Cheng, Y., Wei, Q., Liu, X. J. "Modulation of water surface waves with a coiling-up-space metasurface". AIP Advances. 6(5), 055017 (2016).

Tang, K., Qiu, C., Ke, M., Lu, J., Ye, Y., Liu, Z. "Anomalous refraction of airborne sound through ultrathin metasurfaces". Scientific Reports. 4, 6517 (2014).

Veselago, V. G. "The electrodynamics of substances with simultaneously negative values of μ and ε," Soviet Physics Uspekhi. 10(4), 509(1968).

Wang, C. Q., Cheng, L., Huang, L. "Realization of a broadband low frequency plate silencer using sandwich plates". Journal of Sound and Vibration. 318(4), 792–808 (2008).

Wang, H., Tao, G., Shang, X. "Understanding acoustic methods for cement bond logging". Journal of the Acoustical Society of America. 39, 2407-2416 (2016).

Wang, Q., Zhang, X., Xu, Y., Gu, J., Li, Y., Tian, Z., Singh, R., Zhang, S., Han, J., and Zhang, W. "Broadband metasurface holograms: toward complete phase and amplitude engineering". Scientific Reports. 6, 32867 (2016).

Wu, X., Au-Yeung, K. Y., Li, X., Roberts, R. C., Tian, J., Hu, C., Huang, Y., Wang, S., Yang, Z., Wen, W. "High-efficiency ventilated metamaterial absorber at low frequency". Applied Physics Letters. 112(10), 103505(2018).

Xi, J., Schubert, M., Kim, J., Schubert, E., Chen, M., Lin, S., Liu, W., Smart, J. "Optical thin-film materials with low refractive index for broadband elimination of Fresnel reflection". Nature Photonics. 1, 176–179 (2007).

Xiao, S., Ma, G., Li, Y., Yang, Z. H., Sheng, P. "Active control of membrane–type acoustic metamaterial by electric field". Applied Physics Letters. 106(9), 091904 (2015).

Xie, Y., Popa, B. I., Zigoneanu, L., Cummer, S. A. "Measurement of a broadband negative index with space-coiling acoustic metamaterials". Physical Review Letters. 110(17), 175501 (2013).

Xie, Y., Wang, W., Chen, H., Konneker, A., Popa, B. I., Cummer, S. A. "Wavefront modulation and subwavelength diffractive acoustics with an acoustic metasurface". Nature Communications. 5, 6553 (2014).

Yang, J. J., Huang, M., Cai, G. H., Xie, R. S., Yang, J. "Design of acoustic metamaterial devices based on inverse method". Journal of Vibration and Acoustics. 135(5), 051024 (2013).

Yang, M., Li, Y., Meng, C., Fu, C., Mei, J., Yang, Z., Shen, P. "Sound absorption by subwavelength membrane structures: a geometric perspective". Comptes Rendus Mecanique. 343(12), 635-644 (2015).

Yuan, B., Cheng, Y., Liu, X. "Conversion of sound radiation pattern via gradient acoustic metasurface with space-coiling structure". Applied Physics Express. 8(2), 027301 (2015).

Zhai, S., Chen, H., Ding, C., Zhao, X. "Double-negative acoustic metamaterial based on meta-molecule". Journal of Physics D: Applied Physics. 46, 475105 (2013).

Zhang, Y. Wen, J. Xiao, Y. Wen, X. Wang, J. "Theoretical investigation of sound attenuation of membrane-type acoustic metamaterials". Physics Letters A. 376, 1489-1494 (2012).

Zhao, J., Li, B., Chen, Z., Qiu, C. "Manipulating acoustic wavefront by inhomogeneous impedance and steerable extraordinary reflection". Scientific Reports. 3, 2537 (2013).

Zhao, Y., Alù, A. “Manipulating light polarization with ultrathin plasmonic metasurfaces”. Physical Review B. 84(20), 205428 (2011).

Zhu, J., Christensen, J., Jung, J., Moreno, L. M., Yin, X., Fok, L., Zhang, X., Garcia-Vidal, F. J. “A holey-structured metamaterial for acoustic deep-subwavelength imaging”. Nature Physics. 7, 52–55(2011).

Zhu, X., Li, K., Zhang, P., Zhu, J., Zhang, J., Tian, C., Liu, S. “Implementation of dispersion-free slow acoustic wave propagation and phase engineering with helical-structured metamaterials”. Nature Communications. 7, 11731 (2016).

Zingoneanu, L., Popa, B. L., Cummer, S. A. “Three-dimensional broadband omnidirectional acoustic ground cloak”. Nature Materials. 13, 352-355 (2014).

CURRICULUM VITAE